

AD-A174 944

THE MORPHOLOGY OF BROKEN CLOUD FIELDS OVER OCEAN
SURFACES USING LANDSAT(U) TEL-AVIV UNIV (ISRAEL) DEPT
OF GEOPHYSICS AND PLANETARY SCIEN J H JOSEPH

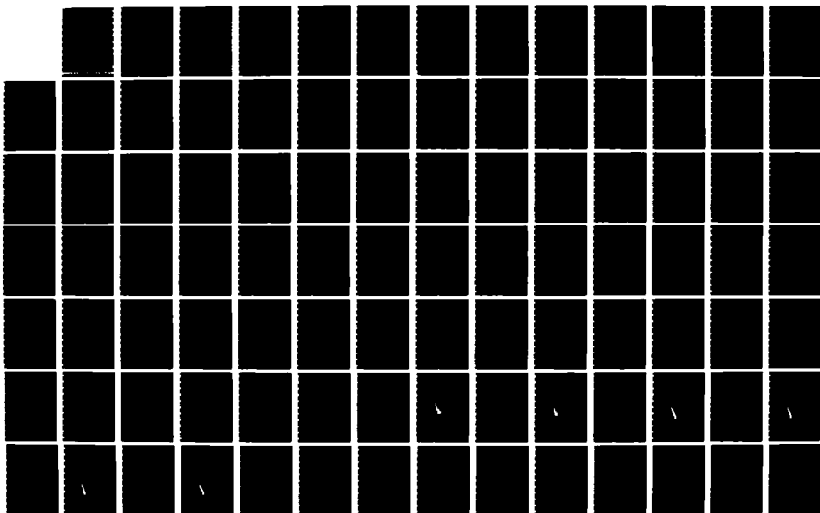
1/2

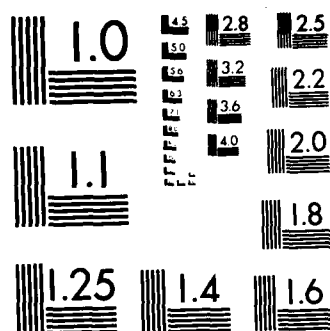
UNCLASSIFIED

05 MAY 86 AFOSR-TR-86-2126 AFOSR-84-0357

F/G 4/1

NL





MICROCOPY RESOLUTION TEST CHART
NATIONAL BUREAU OF STANDARDS 1963-A

AD-A174 944

DTIC FILE COPY


AFOSR-TR. 86-2126

**The Morphology of Broken Cloud Fields
over Ocean Surfaces Using LANDSAT**

Approved for public release;
distribution unlimited.

**Joachim H. Joseph
Dept. of Geophysics and Planetary Sciences
Tel Aviv University
Ramat Aviv, Tel Aviv 69978
Israel**

AIR FORCE OFFICE OF SCIENTIFIC RESEARCH (AFSC)
NOTICE OF TRANSMITTAL TO DTIC
This technical report has been reviewed and is
approved for public release IAW AFR 199-12.
Distribution is unlimited.
MATTHEW J. KEPPER
Chief, Technical Information Division

1

1986

86 12 11

REPORT DOCUMENTATION PAGE

1a. REPORT SECURITY CLASSIFICATION UNCLASSIFIED			1b. RESTRICTIVE MARKINGS		
2a. SECURITY CLASSIFICATION AUTHORITY			3. DISTRIBUTION/AVAILABILITY OF REPORT Approved for public release; Distribution unlimited		
2b. DECLASSIFICATION/DOWNGRADING SCHEDULE					
4. PERFORMING ORGANIZATION REPORT NUMBER(S)			5. MONITORING ORGANIZATION REPORT NUMBER(S) AFOSR-TR- 86-2126		
6a. NAME OF PERFORMING ORGANIZATION Tel Aviv University		6b. OFFICE SYMBOL (If applicable)	7a. NAME OF MONITORING ORGANIZATION AFOSR		
6c. ADDRESS (City, State and ZIP Code) Ramat Aviv, Isreal 69978			7b. ADDRESS (City, State and ZIP Code) Bldg. 410 Bolling AFB, Dc 20332		
8a. NAME OF FUNDING/SPONSORING ORGANIZATION AFOSR		8b. OFFICE SYMBOL (If applicable) NC	9. PROCUREMENT INSTRUMENT IDENTIFICATION NUMBER AFOSR-84-0357		
8c. ADDRESS (City, State and ZIP Code) Bldg. 410 Bolling AFB, DC 20332			10. SOURCE OF FUNDING NOS.		
			PROGRAM ELEMENT NO. 61102F	PROJECT NO. 2310	TASK NO. A1
11. TITLE (Include Security Classification) The Morphology of Broken Clouds Fields over Ocean Surfaces Using Landsat					
12. PERSONAL AUTHOR(S) Joachim Joseph					
13a. TYPE OF REPORT Final		13b. TIME COVERED FROM 840915 TO 850914	14. DATE OF REPORT (Yr., Mo., Day) 86 May 05		15. PAGE COUNT 139
16. SUPPLEMENTARY NOTATION					
17. COSATI CODES			18. SUBJECT TERMS (Continue on reverse if necessary and identify by block number)		
FIELD	GROUP	SUB. GR.			
19. ABSTRACT (Continue on reverse if necessary and identify by block number) SEE FINAL MASIS					
20. DISTRIBUTION/AVAILABILITY OF ABSTRACT UNCLASSIFIED/UNLIMITED <input type="checkbox"/> SAME AS RPT. <input type="checkbox"/> DTIC USERS <input type="checkbox"/>			21. ABSTRACT SECURITY CLASSIFICATION		
22a. NAME OF RESPONSIBLE INDIVIDUAL Lt. Col Koermer			22b. TELEPHONE NUMBER (Include Area Code) 202-767 4963	22c. OFFICE SYMBOL NC	

Contract Number:

AFOSR-83-0239

Title:

The Morphology of Broken Cloud Fields over Ocean
Surfaces Using LANDSAT

Joachim H. Joseph
Dept. of Geophysics and Planetary Sciences
Tel Aviv University
Ramat Aviv, Tel Aviv 69978
ISRAEL

5/5/1986

Final Report:

6/15/83 - 9/15/85

Approved for public release

Distribution unlimited

Prepared for:

AFGL Hanscom Field, Mass., U.S.A.

and

European Office of Aerospace and Development
London, England.



AI

Chapter 1: Introduction and Summary

	<u>Page</u>
1.1 Comparison between proposed and achieved tasks	8
1.2 Presentation at scientific meetings	10
1.3 Publications	11
1.4 Future applications	11
1.5 Work in process	12

Chapter 2: Processing of LANDSAT Data

	<u>Page</u>
1. Introduction	13
2. Discrimination between cloud and background	15
2.1 The incremental method	15
2.2 The composite histogram method	16
2.3 Spatial coherence	22
2.4 Multispectral histogrammes	23
2.5 Summary	24
3. The statistical properties of single clouds	25
3.1 The enumeration of clouds	26
3.2 Holes in clouds	32
3.3 Cloud perimeters	33
3.4 Cloud areas	34
3.5 Cloud centers	34
3.6 Minimal distance between cloud pairs	35
3.7 The ratio of cloud area to cloud area of influence	35

List of Figures for Chapter 2

	<u>Page</u>
Figure 2.1: The incremental method. The X-axis is the grey level threshold value in all figures.	37
Figure 2.2: The composite histogram method. The X-axis is the grey level threshold value. The H1, H2 and H3 curves are explained in the text.	41
Figure 2.3: The effect of noise on H1, H2 and H3 and on the chosen threshold. H1P, H1M, H3P and H3M are elaborated upon in the text.	43
Figure 2.4: The bi-spectral histogram method. (a) ocean background, (b) ocean background overlain by slight haze, (c) cloudy ocean area.	45
Figure 2.5: The Laplacian as a function of the grey level.	46
Figure 2.6: Flowchart of the cloud enumeration process.	48
Figure 2.7: The size distribution of holes in clouds.	49

List of Tables for Chapter 2

Table 2.1: Variation of cloud parameters with grey level threshold.	50
Table 2.2: Numerical values of bi-spectral histograms of Figure 4.	51

Chapter 3: The distribution of Cumulus cloud sizes and intercloud distances as derived from LANDSAT

	<u>Page</u>
3.1: Introduction	54
3.2: Analysis of Landsat imagery	56
3.3: The size distribution of clouds	60
3.4: The distribution of minimal distances between pairs of cloud centers	62
3.5: Discussion and summary	66
3.6: Acknowledgements	69
3.7: References	70

List of Figures for Chapter 3

Figure 3.1:	Analysis of Landsat imagery - the basic problem of data analysis: discrimination between clouds and backgrounds	72
Figure 3.2:	Comparison of exponential and power-law fits to the experimental data on cloud radius	73
Figure 3.3:	Size distribution and accumulated distributions for three cases. Spanning the range of observed cloudiness	74
Figure 3.4:	Histograms of minimal distances between cloud centers for bands MSS4 and 7 in case 7032 (See Appendix).	86
Figure 3.5:	The distribution function of minimal distance between cloud centers for three cases spanning the range of cloudiness observed - (a) Case 7067, cloudiness 1.4%; (b) Case 7025, cloudiness 13.5%; (c) Case 7024, cloudiness 32.9%.	87

List of Tables for Chapter 3

Table 3.1:	Sources of information on clouds	90
Table 3.2:	The size distribution of Cu clouds over oceans	91
Table 3.3:	The distribution function of minimal distance between cloud pairs using a log-normal function	92
Table 3.4:	The distribution function of minimal distance between cloud pairs using a Weibull function	93

Chapter 4: On the fractal dimension of broken Cumulus cloud fields

	<u>Page</u>
4.1 Introduction	94
4.2 Data analysis	95
4.3 The fractal dimension of cloud perimeters	97
4.4 Discussion	101
4.5 Summary	104
4.6 Acknowledgements	105
4.7 References	105

List of Figures for Chapter 4

Figure 4.1:	The fractal dimension of very large cloud perimeters (Lovejoy 1982).	106
Figure 4.2:	A range of examples of the relationship between cloud perimeters and areas for four locations.	107

List of Tables for Chapter 4

Table 4.1:	Summary of data on the fractal dimension of cloud perimeters	111
------------	--	-----

Chapter 5: Application to Cumulus cloud convection

	<u>Page</u>
5.1 The mean mass flux at cloud bottom altitude	112
5.2 The ratio of updraft to downdraft in convective Cu clouds	117
5.3 References	121

List of Figures for Chapter 5

Figure 5.1:	The dependence of the mean mass flux at cloud bottom as a function of cloudiness in percent	122
Figure 5.2:	The parameter γ as a function of r for three cases: (a) Case 7067, cloudiness 1.4%; (b) Case 7025, cloudiness 13.5% (c) Case 7024, cloudiness 33%. All cases in Band MSS4. Results for MSS7 are identical.	123

List of Tables

Table 5.1:	Mean mass flux at cloud bottom altitude in $10^{-2} \text{ kg m}^{-2} \text{ s}^{-1}$	126
Table 5.2:	2-D Histogram of the ratio of cloud area to cloud area of influence as a function of cloud effective radius.	127
	(a) MSS4; (b) MSS7	

APPENDICES

	<u>Page</u>
Introduction	129
Appendix 1: Summary of images analysed	131
Appendix 2: Summary of general conditions of analysed images	132
Appendix 3: Summary of size distribution and perimeter to area fit parameters	133
Appendix 4: Summary of parameters of fit of minimal distance between clouds	135
Appendix 5: Description of cooperation and assessment of the contribution of both partners.	136
Appendix 6: Inventory and status of data	138

Chapter 1: Introduction

Chapter 1.1

Comparison between proposed and achieved tasks

↖ The aims of our study as outlined in our original proposal were the following:

- (a) Carry out an initial study of suitably chosen LANDSAT data over both land and sea;
- (b) Develop the first step in the evolution of semi-automatic computer algorithms to obtain cloud morphology data on a global and long-term basis;
- (c) Provide a basis for future coordinated satellite, air and ground-based experiments on cloud field properties.
- (d) Test and improve the modelling of cloud field optical properties for various purposes;
- (e) Use the data for testing models of atmospheric dynamics on various scales and to develop methods for using cloud morphology data as diagnostics for large scale atmospheric characteristics.

These aims have been carried out for the most part. Suitable LANDSAT 2,3 and 4 imagery was chosen over the Atlantic, Pacific and Indian Oceans. Hundreds of images were examined by eye and computer catalogue at the Goddard Space Flight Center.

Thirty LANDSAT 2 or 3 full scenes and 41 LANDSAT 4 quarter scenes were selected of which only the LANDSAT 2 and 3 scenes have been analysed. The LANDSAT 4 images which include thermal IR data are in the process of being analysed and will be the subject of a separate report. This will also include the calibration and use

of a new method, based on the solar spectral range, of cloud top height determination, developed by us and described in previous reports.

We have developed a semi-automated algorithm for the production of cloud field maps over sea. Because of the unexpected degree of inhomogeneity of the ocean surface, we studied a variety of schemes for cloud-background discrimination, none of which is really optimal. This is also the reason the analysis of imagery over land has been deferred for a later study.

The method has been applied and is suitable for man-computer interactive analysis of cloud fields after suitable preparation of the analyst. The method provides histograms of single cloud parameters and their various moments and correlation. Some ideas have evolved for the analysis of 2D-cloud patterns which have been submitted to the USAF in a "letter of intent" recently.

The methods of analysis and the data-base may be used as a basis for the planning of possible future dedicated satellite-based cloud field morphology missions. These should include surface and air-based field morphology data at all times of the day.

We have developed an analytical model of the reflectivity of bar clouds of given aspect ratios, inter-cloud distances and optical properties. Cloud-cloud scatter and shading have been explicitly taken into account. Future development will include a 3-D box cloud array and the use of our data base for calibration.

Finally, the data base has been applied to a current model of cloud convection and mean convective mass fluxes have been estimated which are in reasonable agreement with theoretical and in-situ estimates.

1.2: Presentations at scientific meetings

The material summarized in this report has been presented in part at several meetings.

1. J.H. Joseph: "The Morphology of Broken Cloud Fields from LANDSAT".
Symp. R1 - Interdependence of clouds, Trace Substances, Radiation and Climate IAMAP - IAGA Conf. Hamburg, F.R.G. August 1983.
2. J.H. Joseph: "The Morphology of Fair Weather Cumulus Clouds as Remotely Sensed from Satellites and some Applications" Paper 4.3.4. Symp. on Space Observations for Space Studies, XXV COSPAR, Graz, Austria, 25-29 June 1984.
3. R.F. Cahalan: "Climatological Statistics of Cloudiness" - Invited Paper, Proc. 5th Conf. on Atmospheric Radiation, Baltimore, MD, Oct. 1983.
4. J.H. Joseph: "The Role of Cloud Field Morphology in Weather and Climate Studies - The Charney Workshop on Weather Modification, Caesarea, Oct. 27-29, 1982.

The material will be discussed in detail at the IBM Workshop on "Fractals and Dynamics" at Oberlach, Austria, June 30 - July 7, 1986.

1.3 Publications

The following publications have resulted from our study:

J.H. Joseph (1985): The morphology of fairweather Cu clouds as remotely sensed for satellites and some applications, Adv. Space. Res. 5, 213-216.

J.H. Joseph (1985): The role of cloud field morphology in weather and climate studies, Isr. J. Earth Sci. 34, 96-101.

J.H. Joseph and R.F. Cahalan: On the morphology of broken Cumulus cloud fields (submitted) 1986.

The various chapters in this report essentially represent the papers that will be submitted for publication in the near future.

1.4 Future Applications

The application of our results to the calculation of transmission of radiation or information through cloudy layers for various purposes - e.g. correction of remotely determined sea surface temperatures, availability of solar radiation or the probability of lines of sight will be discussed this fall at the NASA - GSFC, Greenbelt, MD., which I plan to visit for an extended stay.

1.5 Work in Process

—
This report does not include the totality of tasks outlined in our proposal because the USAF funding was discontinued prematurely.

We are in the process of analysing a large amount of LANDSAT 4 TM data and have an option to acquire SPOT data. The rate of analysis is slower now because of local improvised funding.

The analysis planned is similar and we expect to achieve the following aims:

- (a) Improve our resolution of cloud sizes, etc, down to 30 meters;
- (b) Add an additional source of information, namely the thermal IR emissivities;
- (c) Determine the distribution of the heights of cloud tops from the emission temperatures using spatial coherence techniques. These heights for the first time will be compared to those calculated with our model for height determination in the solar range, using data from the same satellite platform;
- (d) Get a time series on a monthly or yearly basis of possible variations in cloud properties primarily over the ocean East and West of Florida. This will make it possible to correlate the latter with year to year changes in meteorological conditions.

Chapter 2: Processing of LANDSAT DATA

1. Introduction

The type of LANDSAT imagery analysed in this study is broken Cumulus cloud fields over ocean.

The reasons are several and are summarised here in short for completeness. Firstly, about 50% of all clouds are of this type and exist almost continuously over great parts of the globe. Cumulus clouds are therefore an important part of the global cloudiness and are thus worthy of investigation in their own right.

Secondly, as will be described in this chapter, the discrimination of clouds against their background is one of the biggest problems of the data analysis. Bright clouds over a dark sea were therefore chosen as a first topic of investigation, later augmented by a study of the effects of a quite variable ocean background on the results of the analysis.

Four main classes of problems will be addressed in this chapter:

- (1) Discrimination between cloud and background
- (2) Recognition of a connected cluster of pixels as a cloud
- (3) Definition of the properties of a single cloud
 - (a) area;
 - (b) perimeter;
 - (c) effective radius;
 - (d) location;
 - (e) center of gravity;
 - (f) nearest neighbour;
 - (g) nearest neighbour of comparable or larger area;
 - (h) holes in cloud;
 - (i) cloud top altitude.

(4) Properties of the cloud field, assuming clouds to be independent of one another. Both the experimental data and their fit to chosen functions are available.

- (a) Distribution function of equivalent radii, r_e ;
- (b) Distribution function of areas, a ;
- (c) Distribution function of nearest neighbours, D ;
- (d) Distribution function of perimeters, P ;
- (e) The two-dimensional histogram of $(\log P, \log a)$ and the fractal dimension of cloud fields;
- (f) The relationship of actual cloud area to area of influence of a cloud;
- (g) Total cloudiness;
- (h) Total number of clouds;
- (i) Area of analysed image

2. Discrimination between cloud and background

The discrimination between cloud and ocean background is not a simple task. Even though brightness of the ocean surface is often assumed to be relatively homogenous, this is not the case in actuality. The brightness of ocean surface changes because of variations in depth and the presence of waves, haze or fog.

In order to determine the location of the cut between cloud and background, we applied or developed several methods, no single one of which turned out to be optimal by itself.

2.1 The incremental method

This method starts by assigning a lower limit to cloud brightness (gray level) that is much too high. One then calculates:

- (a) the total number of clouds;
- (b) the number of clouds less than 4 pixels in size;
- (c) the total relative cloud cover

Next, lower and lower thresholds are assigned and the above three properties are calculated for each case. The process terminates when one or more of the following phenomena occurs

- (a) the number of small clouds increases steeply. This means that background noise is added to the actual cloud pixels;
- (b) the number of clouds of area larger than 4 pixels decreases significantly or again random noise connects large clouds;
- (c) the percentage of cloudiness increases significantly.

Finally, we assume that we have converged on an appropriate threshold for a given image when two different spectral bands give the same number of clouds and the same cloudiness.

The problem with this method is that it is difficult to determine a given fixed rate of increase of the small clouds or rate of decrease in the number of large clouds that fits all available images.

Experience has shown that these criteria change from image to image and even from spectral band to spectral band in a single image.

Figure 2.1 and Table 2.1 show a typical example of the application of this method in case 7025.

Figure 2.1 shows the increase with decreasing values of the chosen threshold of the grey level of the number of "all clouds" (Figure 2.1(a) - MSS4, Figure 2.1(f) - MSS7), of the "big clouds" (Figure 2.1(b) - MSS4, Figure 2.1(g) - MSS7), of the "small clouds" (Figure 2.1(c) - MSS4, Figure 2.1(h) - MSS7), of the amount of cloudiness due to the "big clouds" (Figure 2.1 (d) - MSS4, Figure 2.1(i) - MSS7) and of the amount of cloudiness due to "all clouds" (Figure 2.1(e) - MSS4, Figure 2.1(j) - MSS7). All parameters increase slowly with decreasing values of the threshold. Because of the slow variations, we show the same data once more in Table 2.1. On analysis of the figures and the Table the reason for the actual choice of optimal thresholds for the analysis of 69 for MSS4 and of 2 for MSS7 becomes clear.

2.2 The composite histogram method

When developing this method we tried to set up an automatic way to exclude the background by using composites of appropriate sample histograms.

Let us assume that the general histogram, $n(x)$, includes both cloud and background pixels at any given brightness or gray level x . Then the probability for a pixel to have the gray level x is

$$P(x) = n(x)/N$$

where N is the total number of pixels in the histogram. Assuming we have a mixture of cloud and background pixels independent of each other, then

$$P(x) = \frac{n(x)}{N} = P_b(x) m_b + P_c(x) m_c$$

where

$$m_b = N_b/N$$

$$m_c = N_c/N$$

$$P_b(x) = n_b(x)/N_b$$

$$P_c(x) = n_c(x)/N_c$$

and "b" and "c" denote "background" and "cloud" respectively. In addition,

$$m_b + m_c \equiv 1$$

Next, let us assume that for brightness lower or equal to the maximal brightness of background, $x_{\max b}$, there are no cloud pixels, or for

$$x \leq x_{\max b} : P_c(x) \equiv 0$$

This assumption will often but not generally be true for clouds over the ocean, but not necessarily so over land. We thus have in the region

$$(x \leq x_{\max b})$$

$$P(x) \approx P_b(x) m_b$$

or

$$m_b \approx \frac{P(x)}{P_b(x)}$$

In particular at $x = x_{\max b}$

$$m_b = P(x_{\max b}) / P_b(x_{\max b}) = \frac{n(x_{\max b})/N}{n_b(x_{\max b})/N_b}$$

Therefore the probability distribution function for cloud brightness as a function of x is given by

$$P_c(x) = \frac{P(x) - P_b(x) m_b}{1 - m_b}$$

The parameter m_b is assumed to be independent of x and determinable from suitably chosen samples from a given image.

In practice, this method is applied in the following manner. Using a film positive in a given band, n samples of cloud-free areas and m samples of partly cloudy areas are chosen by eye.

A probability distribution function for the background is constructed from the digital data

$$P_j(x) \equiv H1_i = \sum_{j=1}^n H_{i,j} / \sum_{j=1}^n A_j$$

where A_j is a sample area in pixels and $H_{i,j}$ is the histogram of a background sample.

Similarly, the probability distribution function for the mixed samples is constructed.

$$P_2(x) \equiv H2_i = \sum_{j=1}^m H'_{i,j} / \sum_{j=1}^m A'_j$$

where A'_j and $H'_{i,j}$ are the area and histogram of a mixed sample.

The probability distribution function for the clouds alone is then given by

$$P_3(x) \equiv H3_i = (H2_i - H1_{i_{\max}} \times R) / (1 - R)$$

where

$$R \equiv m_b = H2_{i_{\max}} / H1_{i_{\max}}$$

The index i_{\max} is taken as that i where $H1_i$ reaches its maximal value and $H3_i$ is put equal to zero wherever it is negative.

Because of the possible uncertainties in the application of this method we determine an intermediate range of gray levels, in which both clear and cloud-filled pixels may exist. We define this range to lie between the lower limit for the existence of cloud pixels and the lower limit for "doubtful" pixels. The pixels in this range are included with the clouds when they are next to clouds and disregarded when they occur alone.

The intersection between the cloud and background distribution functions is defined as the lower limit for cloud pixels and denoted ICLOUD. It is determined from the data in the following manner. The difference function

$$D_i = H3_i - H1_i$$

is scanned from high to low grey level. When the first negative value is obtained, we calculate

$$\min(D_i, D_{i+1})$$

and ICLOUD is set as the gray level with the lowest difference, D_i .

Next, in order to define the doubtful range - IQUES - we again scan from high to low starting from the maximum of $H3_i$, looking for

$$H3_i \leq \frac{1}{e} \max(H3)$$

The gray level that fulfils the above condition is defined - tentatively - as IQUES 1. If

$$IQUES 1 > ICLOUD,$$

we look for

$$H3_i \leq \frac{1}{e^2} \max(H3),$$

which is then defined as IQUES 1.

Finally, we re-scan the difference function from

$$IMIN = \min (ICLOUD, \max(H3))$$

to find the first grey level for which the function becomes zero or negative. This point is denoted IQUES 2 and the lower limit of the doubtful range, IQUES, is taken as

$$IQUESS = \max (IQUES 1, IQUES 2)$$

Figure 2.2 for case 7025 shows H3, H2 and H1 as well as the various grey levels described above.

For the case of MSS7 this method gives a threshold value similar to the one obtained by means of the previous method 2 and moreover one can see a separation between the dotted histogram for the clouds alone and the full-line curve representing the ocean background. This is not the case however for MSS4 where the two histograms are poorly separated and the previous method indicated a working threshold of 69 as opposed to the value of 55 arrived at here.

The last operation carried out is an attempt to assess the effect of the particular choice of samples made in the above process.

We evaluate a standard deviation for each gray level:

$$S_i = \sqrt{\sum_{j=1}^n (H_{i,j} - M_i)^2 / n}$$

where M_i is the average value

$$M_i = \sum_{j=1}^n H_{i,j} / n$$

Two new probability distribution functions are constructed for the background

$$H1P_i = (\sum_{j=1}^n H_{i,j} + S_i) / AP$$

$$H1M_i = (\sum_{j=1}^n H_{i,j} - S_i) / AM$$

Where AP and AM are the histogram areas to which the area due to the standard deviation is added or subtracted respectively.

One then, once more, goes through the calculation of the probability distribution function for clouds, namely $H3P_1$ and $H3M_1$, for the two perturbed background functions, $H1P_1$, $H1M_1$. Then once more, one evaluates the areas of uncertainty through IQESP, ICLOUDP, IQUESM and ICLOUDM.

In Figure 2.3 we show the function $H1P$, $H3P$, $H1M$, $H3M$ showing the possible error due to the sampling to be unimportant.

This method gives good results for low gain data and does not work for high gain data.

2.3 Spatial coherence

The spatial coherence technique is based on an analysis of the dependence of the variance of the intensity on the latter in a given image. This is done by choosing an area and dividing it into rectangles of nm pixels. In each rectangle, one calculates the average gray level and its standard deviation. These latter are plotted versus the average intensity and then one looks for regions of low standard deviation or high spatial coherence of the pixels, ("feet"). Normally, one should get two regions of low standard deviation - one, for low intensity, representative of the ocean background, the other, for high intensities, represents fully cloud-covered pixels in regions of thick clouds. Between these "feet" one finds an arch of points representing pixels with a cloud-ocean mix of intensities or covered by thinner clouds.

In our case, however, the method does not work very well. We do get a narrow cloud "foot" or "double foot". The foot representing the ocean is very wide and is not suitable for discriminating between clouds and ocean. In other words, the ocean surface is not very homogenous.

When analysing the thermal IR data of LANDSAT 4 and 5, the method does work and will be useful.

2.4 Multispectral histograms

Using MSS4 and MSS7, we constructed one and two-dimensional histograms in both digital and graphical form.

Histograms were constructed of the whole image, of cloud filled and of clear background areas. The various histograms and the images were then analysed visually and simultaneously.

Figures 2.4a,b,c and Table 2.2 give typical results. Figure 2.4a shows a typical sample of a bi-spectral ocean background histogram - a very high peak in the low intensity region. Although we designate this histogram as typical, it should be realised that the constant "peak" may have very different slopes from location to location in the same image due to the inherent inhomogeneity of the reflectivity of the ocean surface. This basic problem of our analysis becomes even clearer when one looks at Figure 2.4b where we show the histogram of the ocean surface slightly obscured by a light haze. The features of the surface histogram are still there but one already sees the extension with a definite slope due to the haze. Finally, Figure 2.4c shows the full histogram of a

cloudy region. The background peak is there as well as a long directed (correlated) slope culminating in a very high peak at the right edge of the diagram, both due to the presence of clouds. It is clear therefore that the problem of discrimination between clouds and background is a major one especially for the smallest clouds with varying and variable optical depths. Luckily, the analysis is not too sensitive to the exact value of the threshold chosen. One last method was also tried and that was the use of a Laplacian to find local changes in the brightness gradient between a given pixel and its neighbours. The results are shown in Figures 2.5(a) and 2.5(b) for MSS4 and MSS7 respectively. The Laplacian is shown as a function of the grey level. Going back from high grey levels we find positive extrema at grey level values of 68 for MSS4 and at 2 for MSS7, quite similar to those found by the incremental method.

2.5 Summary

In summary then, none of the methods is good enough by itself and man-computer interactive choices are necessary for each separate image. Usually, method 2.1 has been adopted.

3. The statistical properties of single clouds

The next stage after the definition of the cloud-background demarcation intensity in a given spectral image is the treatment of the clouds as aggregates of "cloud" pixels.

All pixels with intensities above or equal to the limit are termed "cloud pixels", all others are "background".

The next step to be described is the definition of a cloud. Afterwards, we shall deal with the location and counting of clouds, cloud areas, perimeters, holes in clouds, inter-cloud distances as well as various derived quantities - like the fractal dimension of a cloud field, the ratio between cloud area and its surrounding and the various probability distributions of these and other quantities.

The first step in this long line of activities is the definition of a file (A) that contains 1 for each pixel of cloud intensity and 0 for each pixel of background intensity. In other words - the creation of a high-contrast map from the satellite image.

The neighbours of a given pixel, X_{ij} , in row i and column j in a cloud are defined as part of the same cloud if they have the appropriate intensity, viz., are assigned the value 1.

We take into account all eight neighbours of each cloud pixel, X_{ij} and $(X_{i-1,j-1}, X_{i-1,j}, X_{i-1,j+1}, X_{i,j-1}, X_{i,j+1}, X_{i+1,j-1}, X_{i+1,j}, X_{i+1,j+1})$ as potential parts of the same cloud.

3.1 The enumeration of clouds

Our aim here is to count the clouds and to evaluate their area in pixels. At the end of the process to be described, one identifying cloud number will be assigned to all pixels that belong to the same cloud.

These numbers - the "cloud numbers" - replace the 1's on file A. In addition we file the cloud areas as a vector.

The program creates a fictitious line of zeros above the upper edge of file A. At every stage, the program reads one line $\{M_{i,j}\}$ of 1's and 0's from file A. It always uses two lines, $\{M_{i,j}\}$ and $\{M_{i,j-1}\}$ simultaneously in the counting process.

When the process is finished for one line, a line of cloud numbers of $\{M_{i,j}\}$ replaces $\{M_{i,j}\}$ on file A. Then the next line of $M_{i,j+1}$ is read and the process repeated.

Before initiation of the counting process, a vector JJ is zeroed. In JJ_i , we then keep the cloud number connected to cloud i, Cloud i itself may be connected to another cloud number, etc.

For every line, four neighbours are defined for each pixel - its left neighbour on the same line and its three closest neighbours in the line above. Pixels on the left margin have only two neighbours, those on a right margin have three neighbours.

For each pixel, we find the maximum cloud number (MAX) of its neighbours and the minimum cloud number (MIN), without counting the 0 (background) pixels.

Two cases may occur:

- (a) $\text{Max} = 0$; in this case we introduce into the location of the pixel on line $\{M_{ij}\}$, a new cloud number, N, and enlarge by 1 the area of "cloud number" N namely $\text{ICL}(N)$;
- (b) $\text{Max} \neq 0$; we have to check whether "cloud number" MAX is connected to another cloud number. If

$$\text{ICL}(\text{MAX}) = 0,$$

MAX is infact connected to another cloud number. This is because for any cloud number that is found to be connected to cloud MAX, $\text{ICL}(\text{MAX})$ is added to the area of that cloud and is then put to zero. Therefore in the case

$$\text{ICL}(\text{MAX}) = 0,$$

MAX is exchanged for $\text{JJ}(\text{MAX})$ and we check if

$$\text{ICL}(\text{JJ}(\text{MAX})) = 0$$

etc. until one finds a cloud number for which

$$\text{ICL}(\text{JJ}(\text{MAX})) \neq 0$$

This JJ is the initial cloud number, to which pixel with cloud number MAX is connected. MAX is replaced by this JJ. If abinitio $\text{ICL}(\text{MAX}) \neq 0$, it is not necessary to find a new MAX.

Now again two different cases may be distinguished:

(a) The new MAX cloud number equals MIN or in other words all the neighbours have the same "cloud number". Then we introduce the new MAX into the location of the pixel checked out on line $\{M_{ij}\}$ and increase the area of the cloud ICL(MAX) by one.

(b) The new MAX is different from MIN. In this case, one has to check for each neighbour if its cloud number is connected to another cloud number. We carry out the above process until the initial cloud number is found to which the neighbour is connected. We connect the area ICL (initial cloud number connected to neighbour) to the area ICL (new MAX), zero ICL (cloud number of neighbour) and ICL (initial cloud number connected to neighbour), enter the new MAX into JJ (cloud number of neighbour) and into JJ(initial cloud number connected to neighbour). Then one enters the new MAX into the location of the pixel checked out on line $\{M_{ij}\}$ and increases the area of ICL(MAX) by one.

When the process is finished for each line, one writes M_{ij} on file A and checks for value of maximum cloud number. If the largest cloud number reaches within 500 of the dimension of the vectors JJ and ICL, one executes a reduction of the cloud numbers - eliminating "empty" numbers in the following manner.

We first find the initial cloud number to which every cloud number is connected; we scan JJ_i for i from 1 to NMAX, where NMAX is the largest cloud number reached at the given stage, and check whether $JJ_i = 0$. If not, one checks whether $JJ(JJ_i)$ is equal to zero and so on until equality to zero is reached.

The index of JJ for which the equality to zero is reached is the initial cloud number. One writes the initial cloud number for every cloud on an auxiliary file.

Then one scans ICL_i for i from 1 to NMAX and finds the number of cases of $ICL_i = 0$ up to each case of $ICL_i \neq 0$, and stores it in $ICLO_i$. For each i for which $ICL_i \neq 0$, we write on an additional temporary auxiliary file the value of $ICLO_i$. The latter quantity is the number that has to be subtracted in order to eliminate the intervals formed by the cloud numbers for which $ICL_i = 0$. For each i for which $ICL_i = 0$, we write on this auxiliary file, the cloud number i .

Then we read the two auxiliary files and for each cloud number, i , between 1 and NMAX, we subtract from its cloud number the appropriate $ICLO$ or the number i itself.

The result is a vector with new cloud numbers, arranged sequentially without gaps. Part of the new numbers are zeros.

We read the file A once more upto the line reached in the counting process and enter instead of each M_{ij} the new cloud numbers and rewrite file A.

Finally, we sort ICL_i according to the new (reduced) cloud numbers. We scan ICL_i and sort from $i = 1$ all the areas ICL_i that are different from zero. The rest of the vector ICL_i is set equal to zero.

At the end of the reduction process, we define the new maximal cloud number as NMAX, check if the last line of file A is reached, read the last processed line of file A to $M_{i,j-1}$, read another line from file A and continue.

A flow chart of the complicated process described above is given in Figure 2.6.

3.2 Holes in clouds

The identification, counting and filing of holes is analogous to the operation with cloud areas. In order to forestall the possibility of pixels in a given cloud that are empty but cannot be defined as part of a hole, we count here as neighbours only those pixels that have a common boundary (namely for pixel $X_{i,j}$ - $X_{i+1,j}$, $X_{i-1,j}$, $X_{i,j-1}$, $X_{i,j+1}$).

Using the file of cloud numbers, we identify those pixels inside a cloud that are not cloud pixels.

We end up, with the number of holes and their association to clouds. Figure 2.7 shows typical results (Case 7032). The size distribution of the holes has, similarly to that of the clouds, a power-law type of behaviour. The slope is however, much steeper. In the case shown, the slope of the size distribution of the holes is 12, versus a value of 2.7 for that of the cloud sizes. The influence of the holes on the results of our analysis should therefore be minor, except for the very smallest clouds. It is however always taken into account.

3.3 Cloud perimeters

Cloud perimeters are determined for each cloud by adding the number of outside edges of pixels in the x direction times their length Δx , to the number of such edges in the y direction times the pixel length in the y-direction, Δy . So the i th cloud, has a perimeter P_i given by:

$$P_i = \left(\sum_{ix=1}^n P_x \right) \Delta x + \left(\sum_{iy=1}^m P_y \right) \Delta y$$

All edges abutting non-cloud areas, including holes, are counted.

We do not take into account that non-cloud pixels abutting on cloud pixels may be partially cloudy. This determination of possible partial cloudiness of such single pixels, which are below our resolution, is impossible, except by some assumption - e.g. 50% coverage. Such an assumption does not increase our accuracy and may lead to an under-estimate of both perimeter and area on our part. On the other hand, the fact that we do not smooth the serrated cloud edges leads to a possible over-estimate of perimeter and area of about the same magnitude.

As the discrimination between cloud and non-cloud pixels is indeterminate to about one or two gray levels, we do not think it fruitful to make any correction for the above effects.

3.4 Cloud areas

The area, A , of a cloud i , is simply defined as the number of pixels connected to it multiplied by the area of a single pixel, viz:

$$A_i = \left(\sum_{j=1}^N a_j \right) \Delta x \Delta y$$

3.5 Cloud centers

The center of a cloud is defined as its "center of gravity", where equal weights are given to all pixels. Therefore, the x coordinate of the cloud center is:

$$C_x = \sum_{j=1}^N x_j / N$$

and similarly, the y -coordinate is

$$C_y = \sum_{j=1}^N y_j / N$$

3.6 Minimal distance between cloud pairs

The calculation of minimal inter cloud distance is based on the assumption that each cloud is defined by its center coordinates. Therefore the distance between two clouds is

$$D = ((C_{x2} - C_{x1})^2 + (C_{y2} - C_{y1})^2)^{\frac{1}{2}}$$

Each cloud has at least one neighbour that is closer to it than all the others. The distance between the cloud in question and its closest neighbour defines the minimal inter-cloud distance, DISMIN, for that cloud.

Then, we define a second minimal distance D_{min} , namely the minimal distance between a cloud, i , and its neighbours, j , of $A_j \geq 1.1 A_i$.

This is to take into account that a given cloud may have very small close neighbours in the image that may physically be part of the larger cloud.

3.7 The ratio of cloud area to cloud area of influence

For the latter distribution of minimal distances, we calculate for each cloud a relationship between the cloud area πr_e^2 , and an associated cloud-free 'ring' around it

$$\gamma = \frac{r_e^2}{\frac{(D_{min})^2}{2} - r_e^2}$$

We assume that one half of the minimal distance between the cloud and its neighbour defines the cloud area of influence, and that clouds are circular of area A ,

$$A = \pi r_e^2$$

These ratios must of course be positive. Let us investigate the possibilities for negative values.

The ratio γ is equal to zero only for $r_e = 0$ (no cloud)

Negative values $\gamma < 0$ occur when

$$\left(\frac{D_{\min}}{2}\right)^2 - r_e^2 < 0$$

or

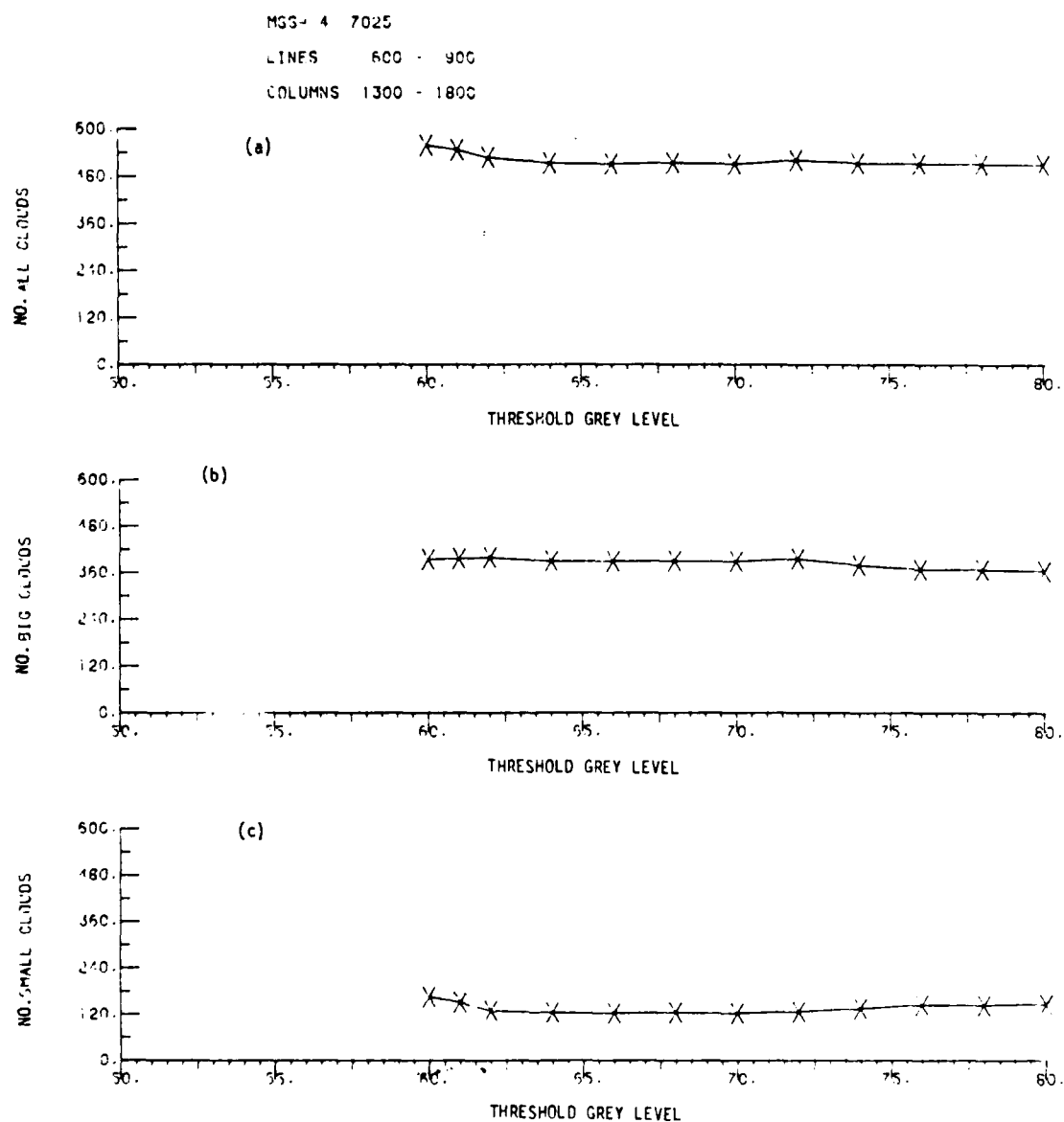
$$\frac{D_{\min}}{2} < r_e$$

This may occur when two elongated clouds occur side by side.

In all cases analysed, almost all data show positive values which are almost independent of cloud size.

I6P BWPH

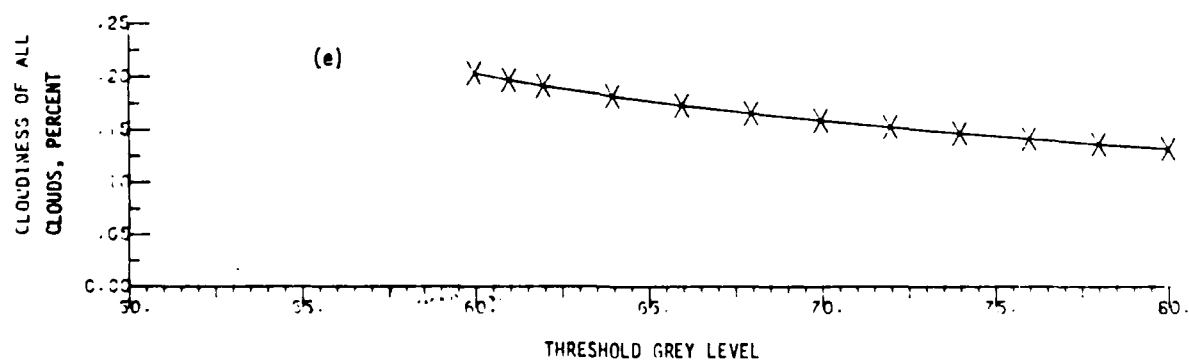
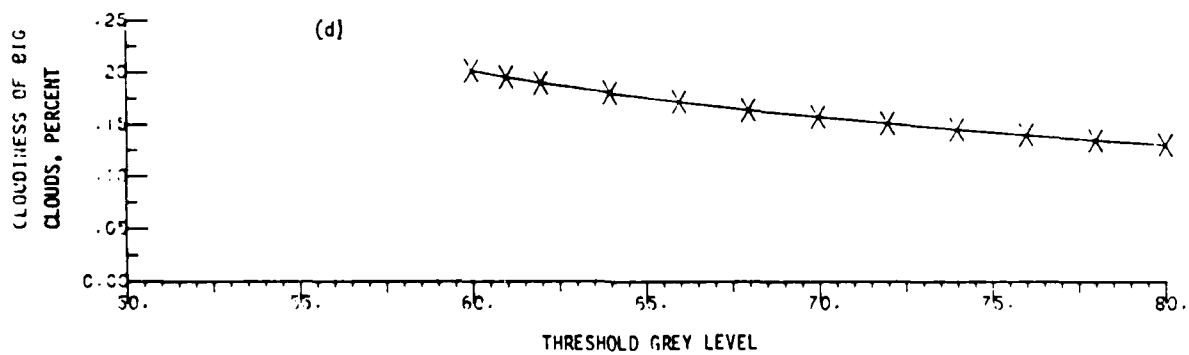
Figure 2.1: The incremental method. The X-axis is the grey level threshold value in all figures.



MSS- 4 7025

LINES 600 - 900

COLUMNS 1300 - 1800



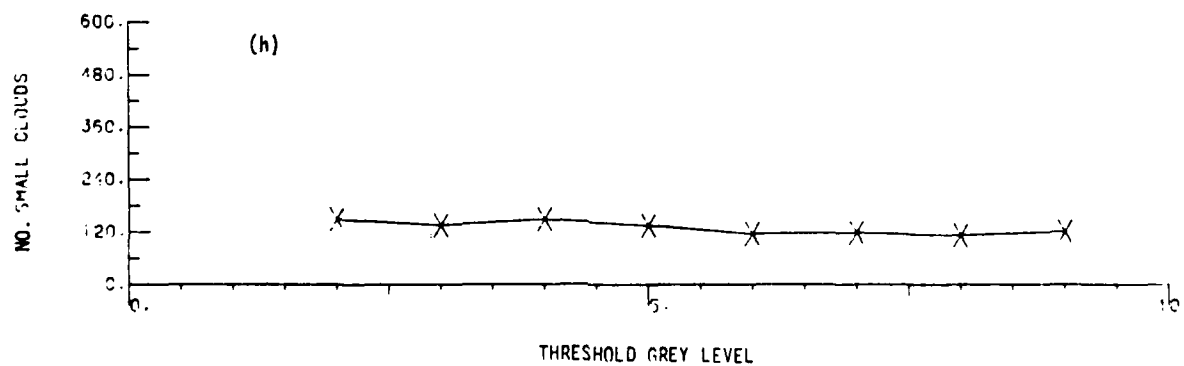
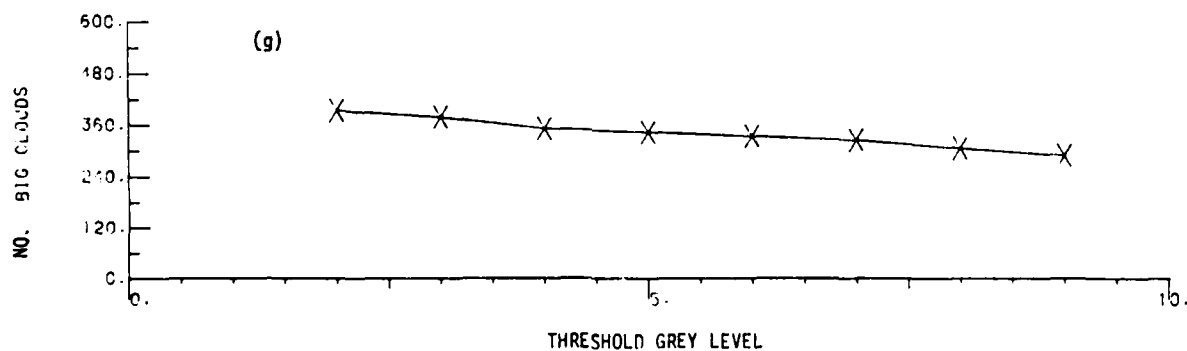
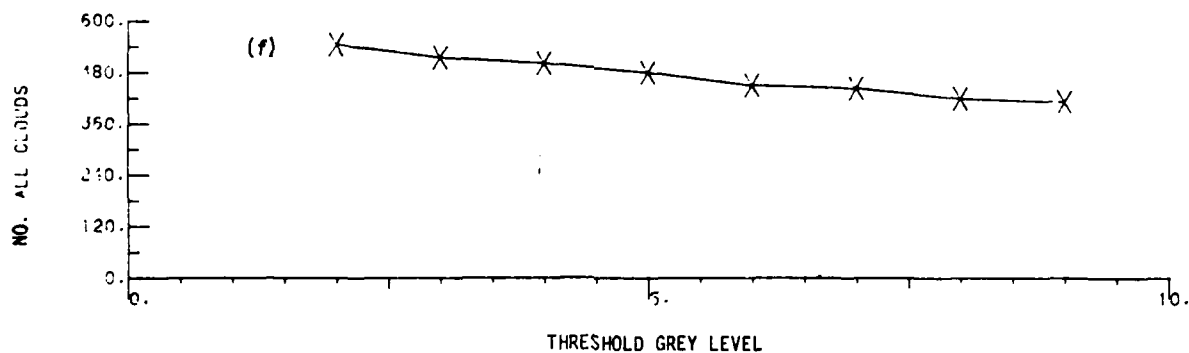
168

BODW

MSS- 7 7025

LINES 600 - 900

COLUMNS 1300 - 1800



MSS- 7 7025

LINES 600 - 900

COLUMNS 1300 - 1800

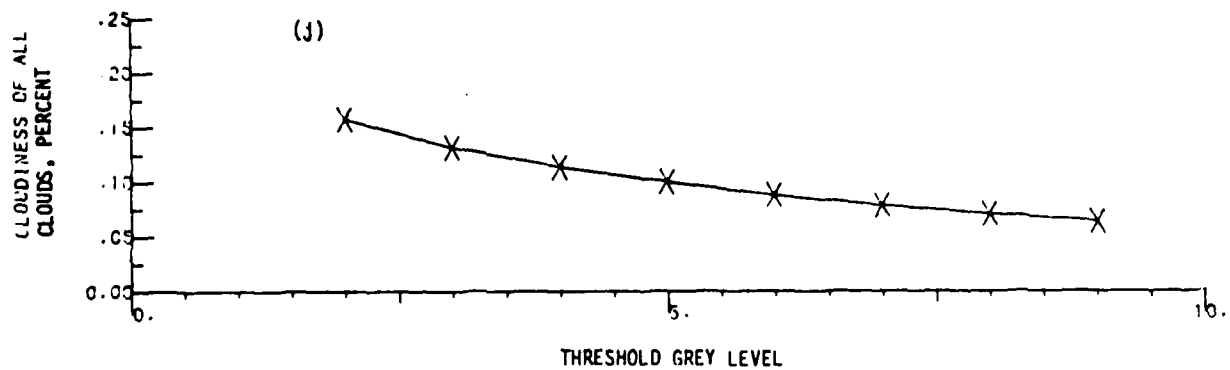
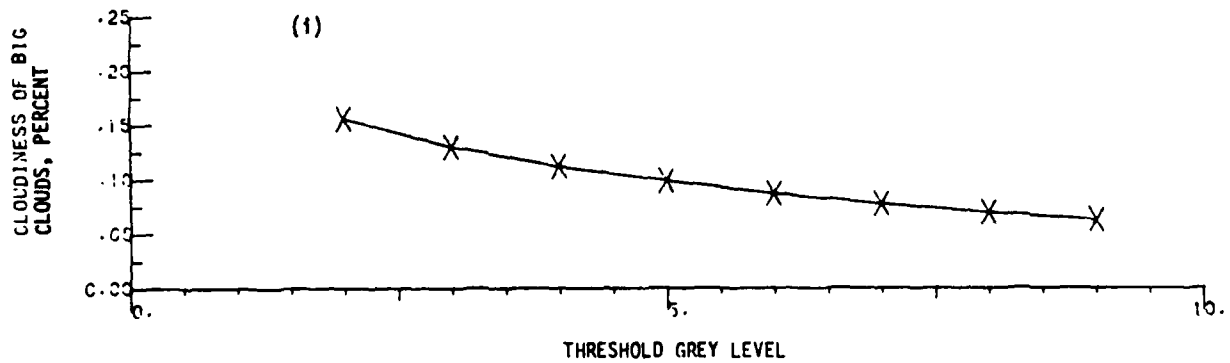
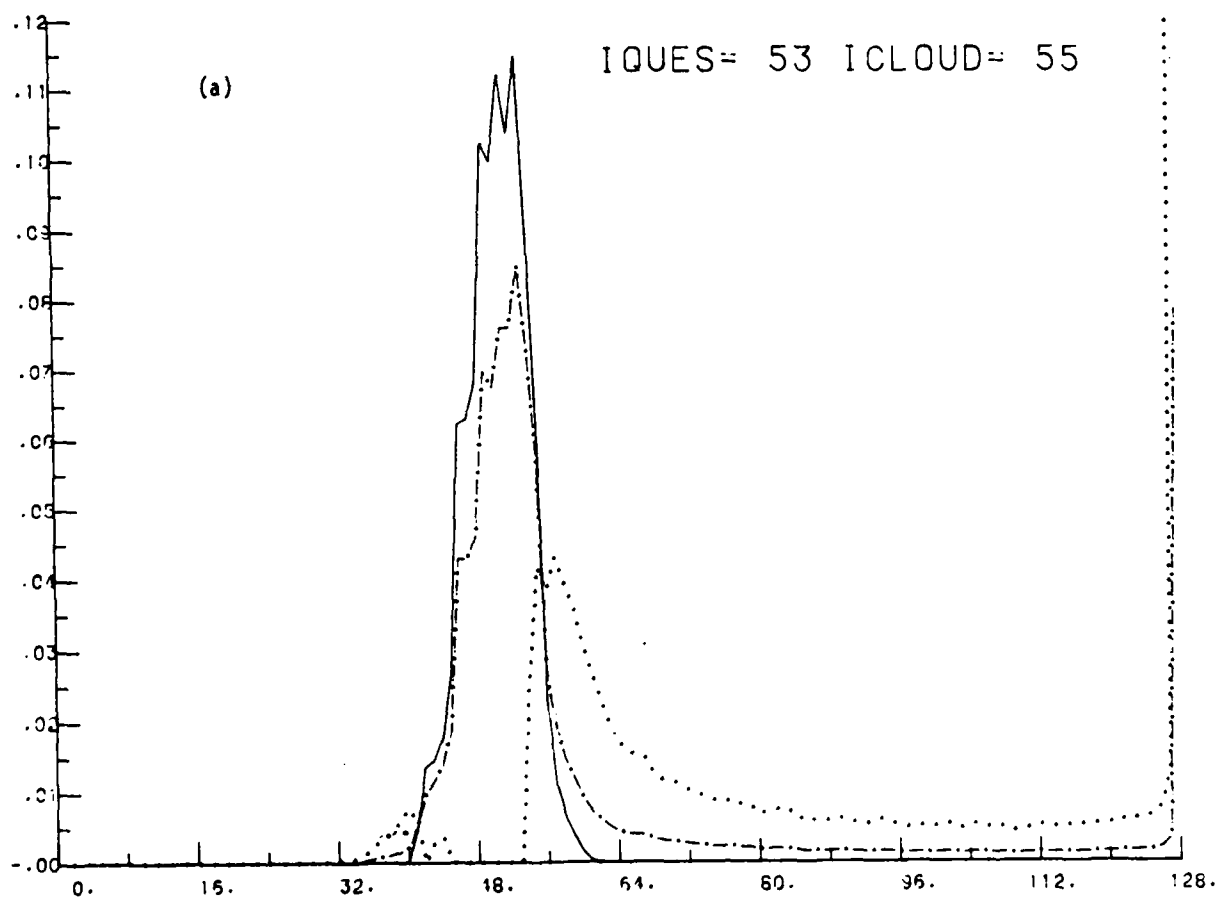


Figure 2.2: The composite histogram method. The X-axis is the grey level threshold value. The H1, H2 and H3 curves are explained in the text.

X-GRAY LEVEL
Y-PROBABILITY
H1 — PROB. OF SEA
H2 --- PROB. OF CLOUDS AND SEA
H3 ... PROB. OF CLOUDS
7025 MSS= 4



X-GRAY LEVEL

Y-PROBABILITY

H1 — PROB. OF SEA

H2 --- PROB. OF CLOUDS AND SEA

H3 ... PROB. OF CLOUDS

7025

MSS= 7

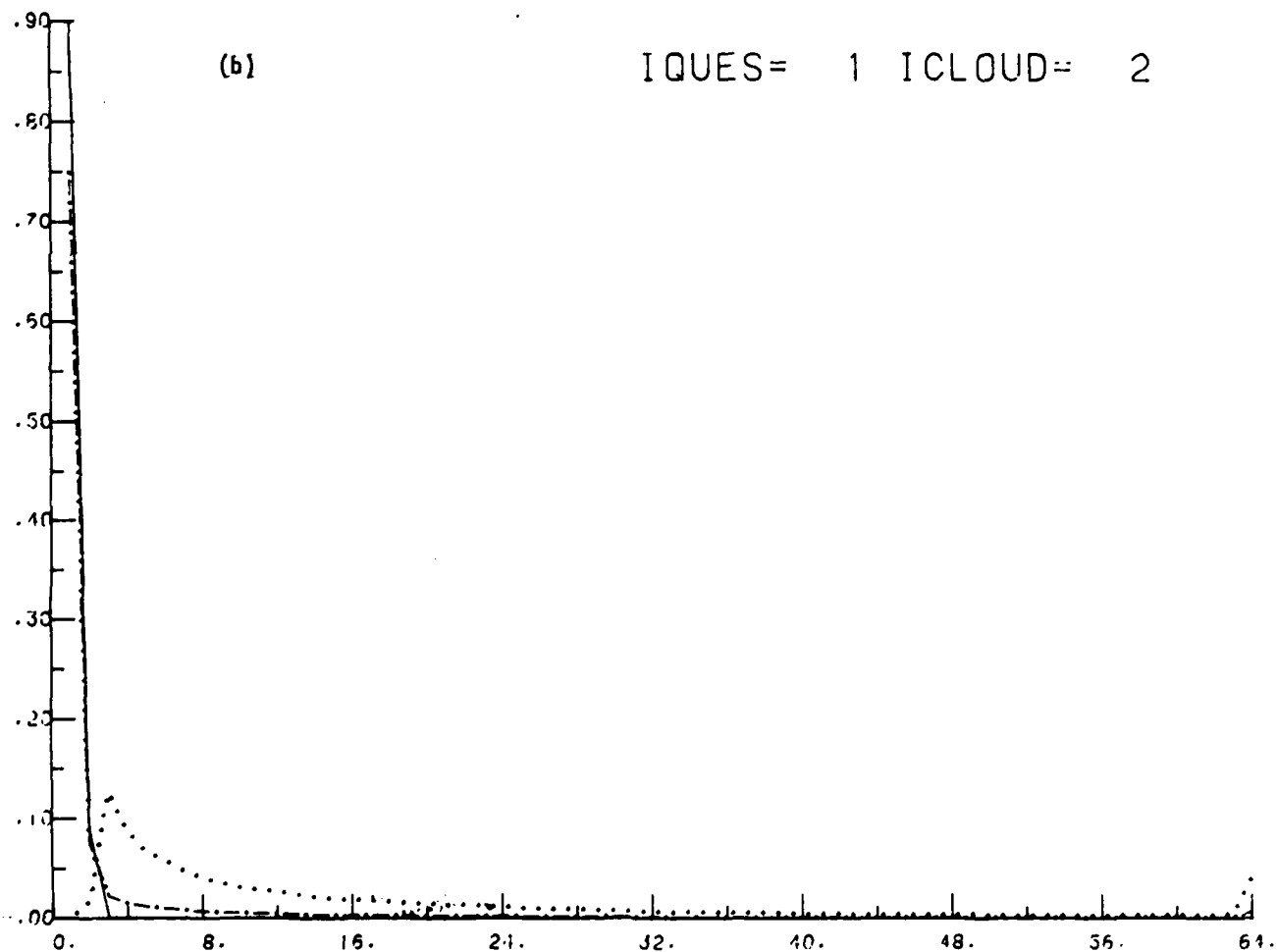
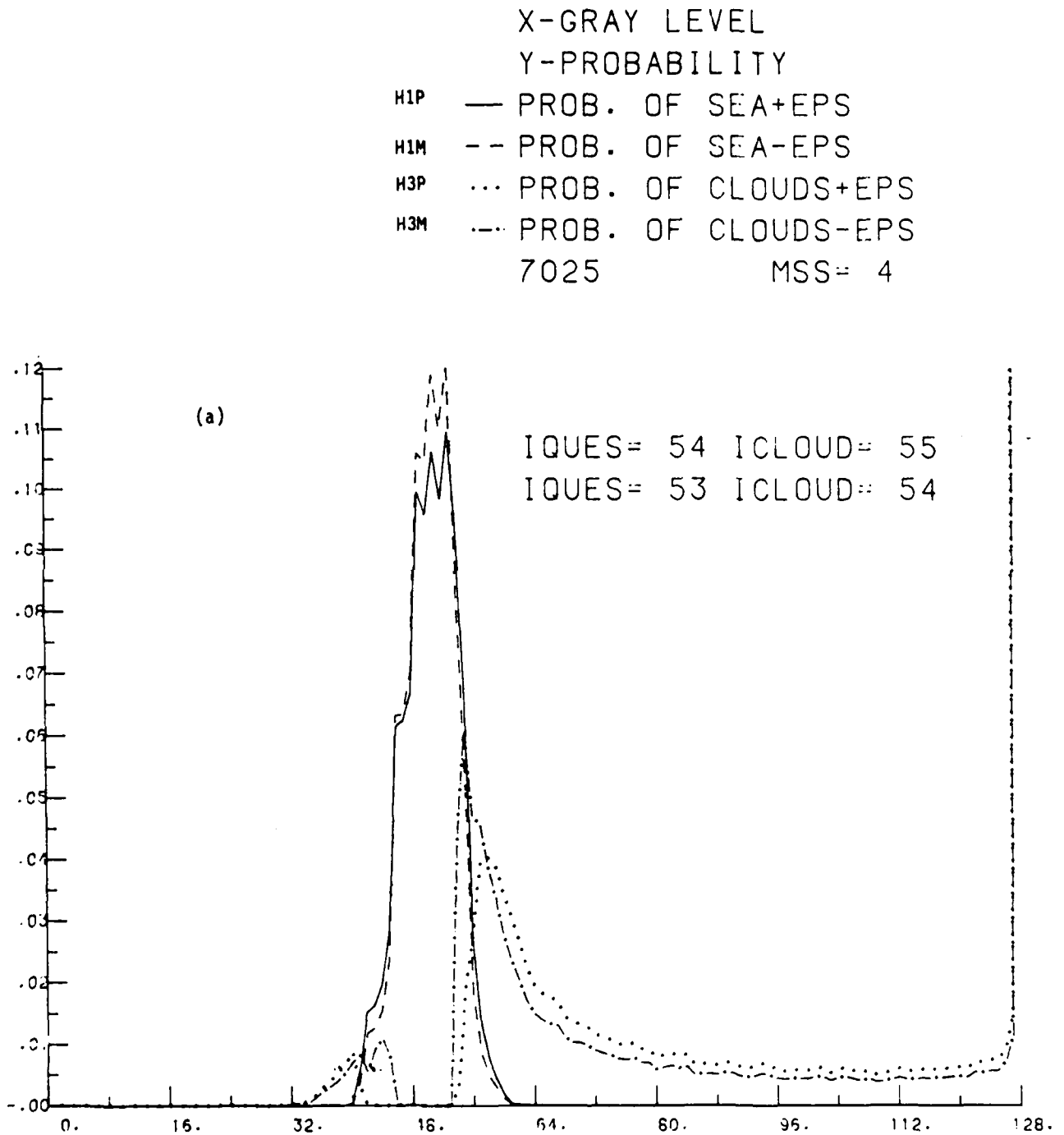


Figure 2.3: The effect of noise on H1, H2 and H3 and on the chosen threshold. HTP, H1M, H3P and H3M are elaborated upon in the text.



X-GRAY LEVEL
Y-PROBABILITY

H1P — PROB. OF SEA+EPS
H1M -- PROB. OF SEA-EPS
H3P ... PROB. OF CLOUDS+EPS
H3M PROB. OF CLOUDS-EPS
7025 MSS= 7

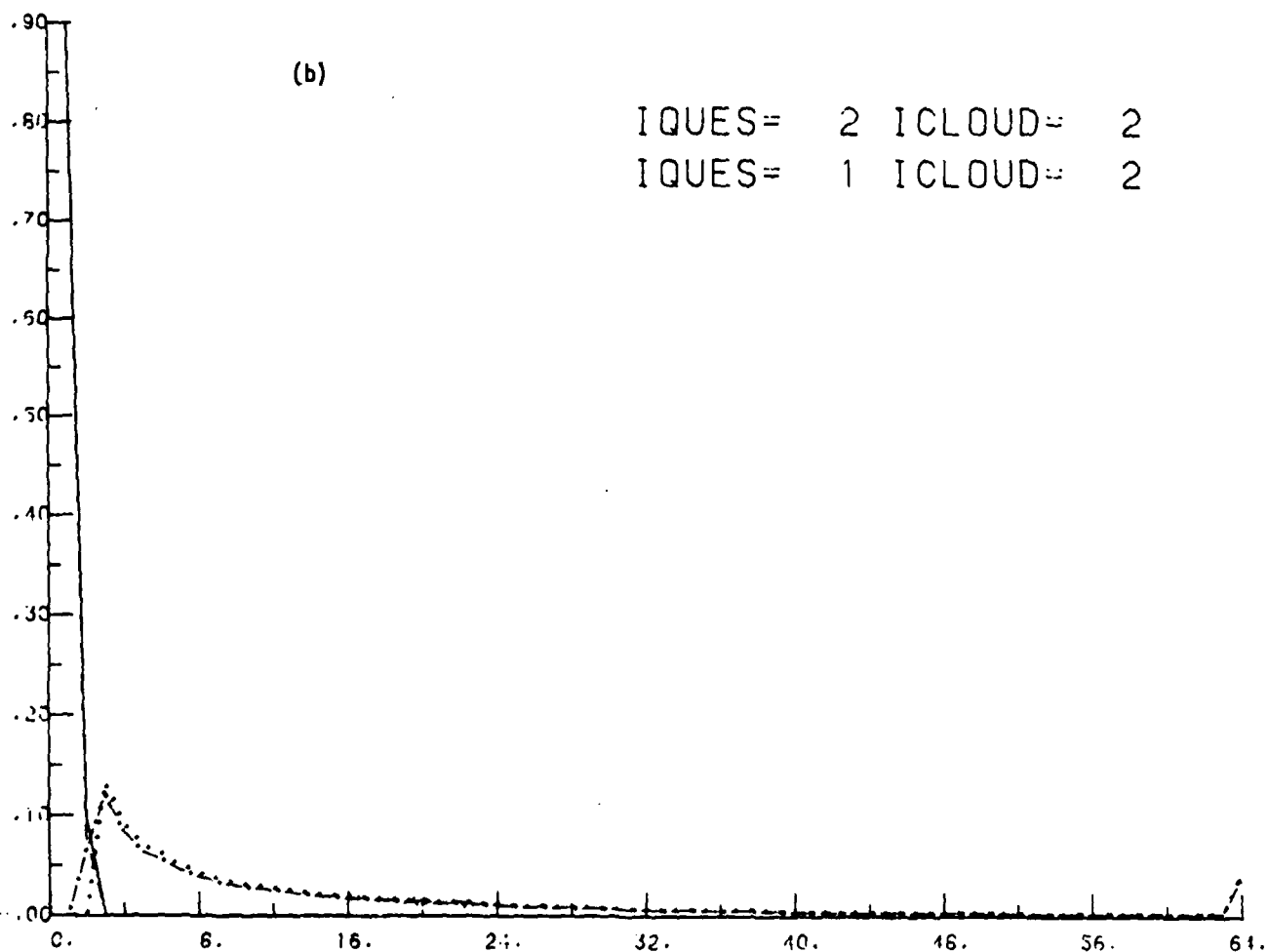


Figure 2.4: The bi-spectral histogram method. (a) ocean background, (b) ocean background overlain by slight haze, (c) cloudy ocean area.

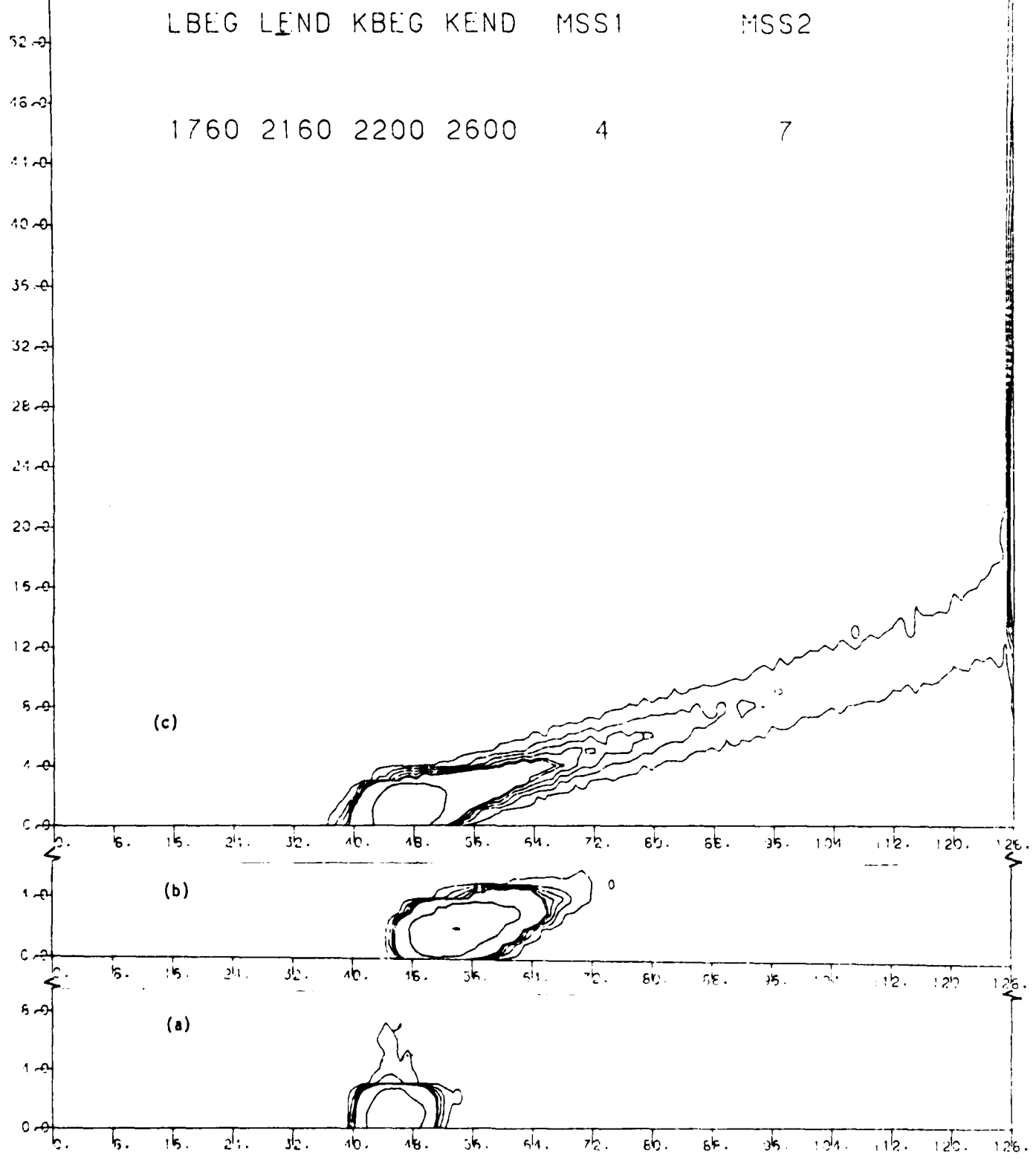
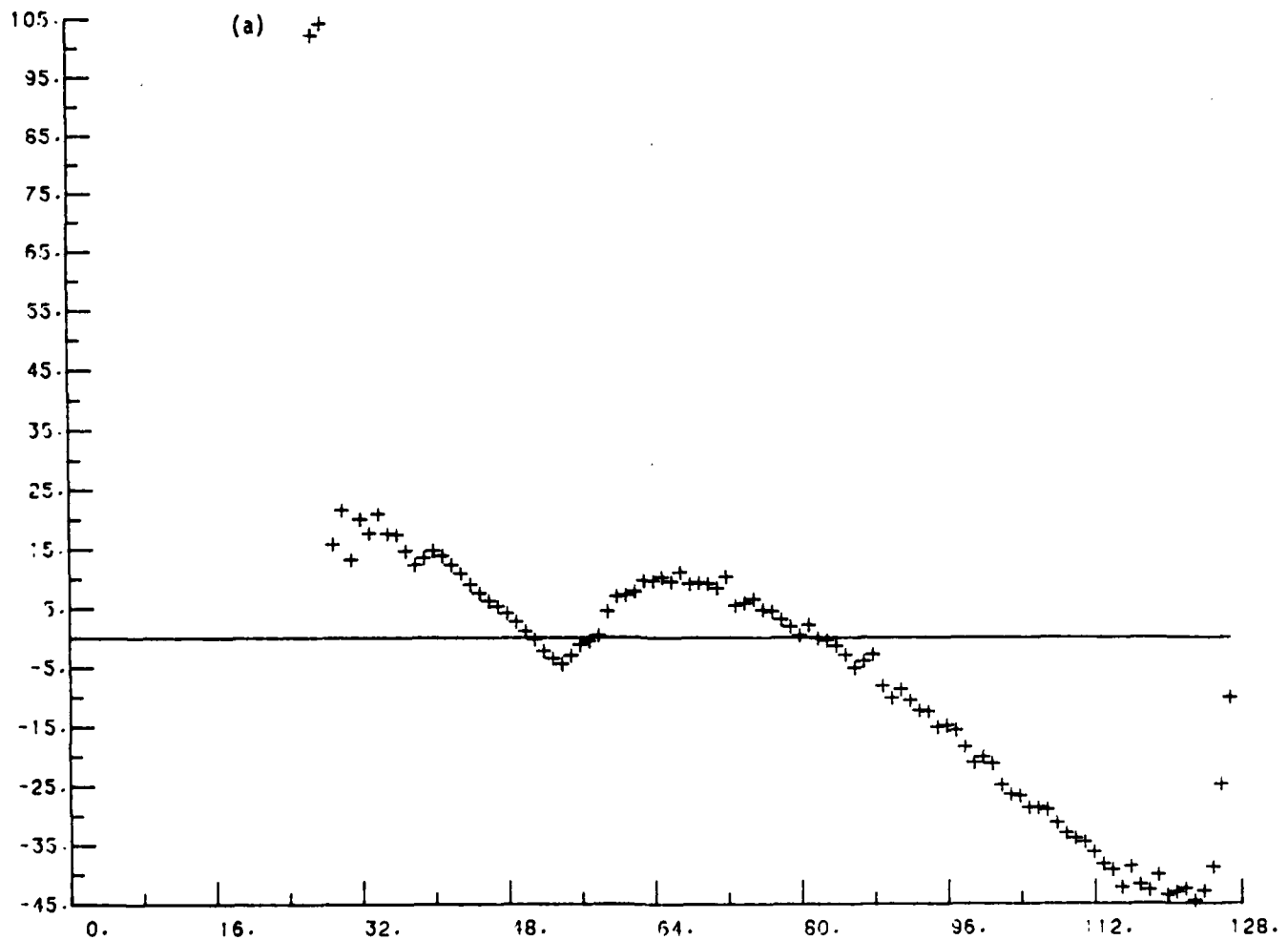


Figure 2.5: The Laplacian as a function of the grey level.

X-GRAY LEVEL
Y-DERIVATIVE

7025

MSS= 4



X-GRAY LEVEL
Y-DERIVATIVE

7025

MSS= 7

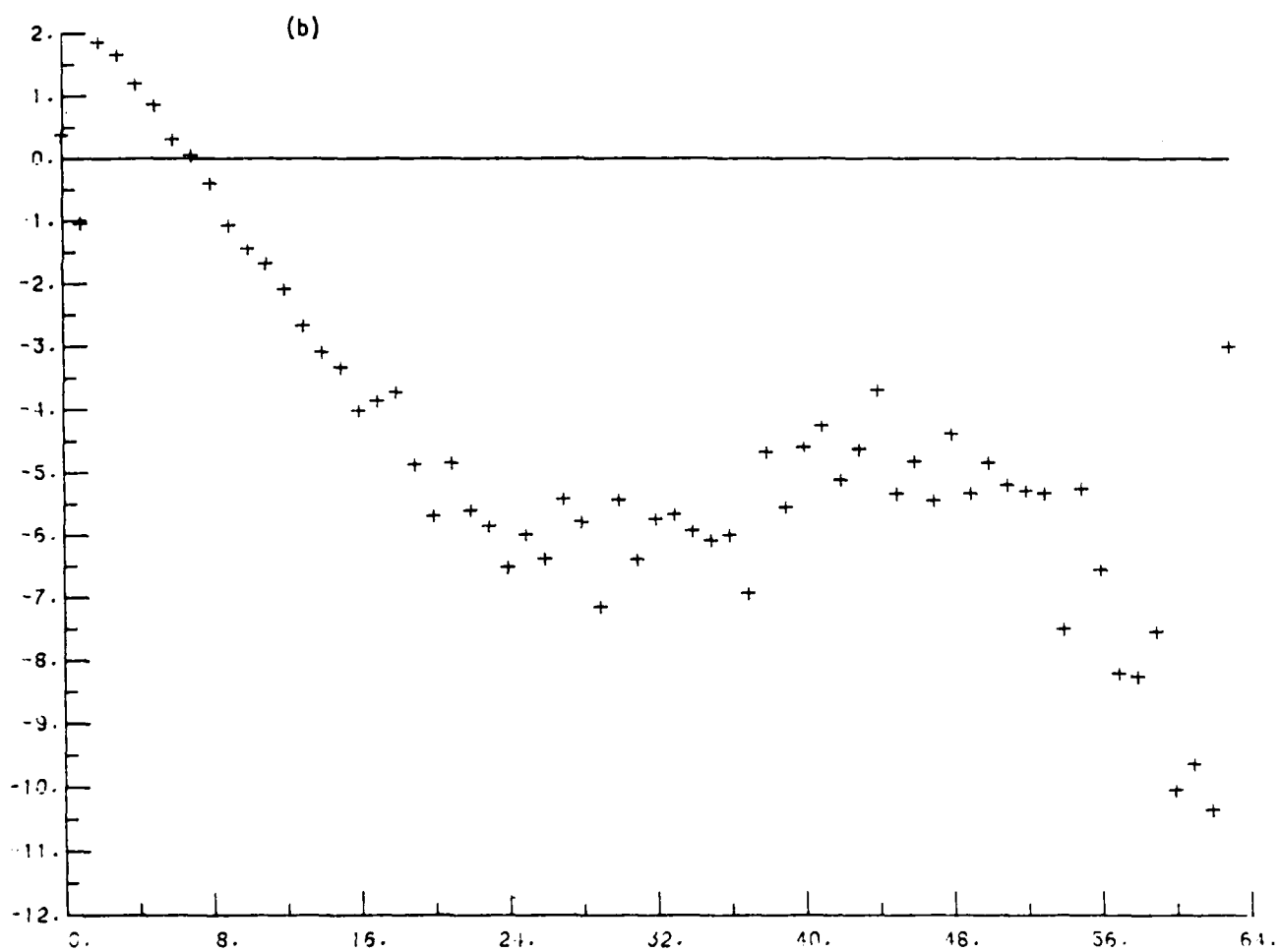


Fig. 2.6: FLOW CHART OF THE ENUMERATION OF CLOUDS

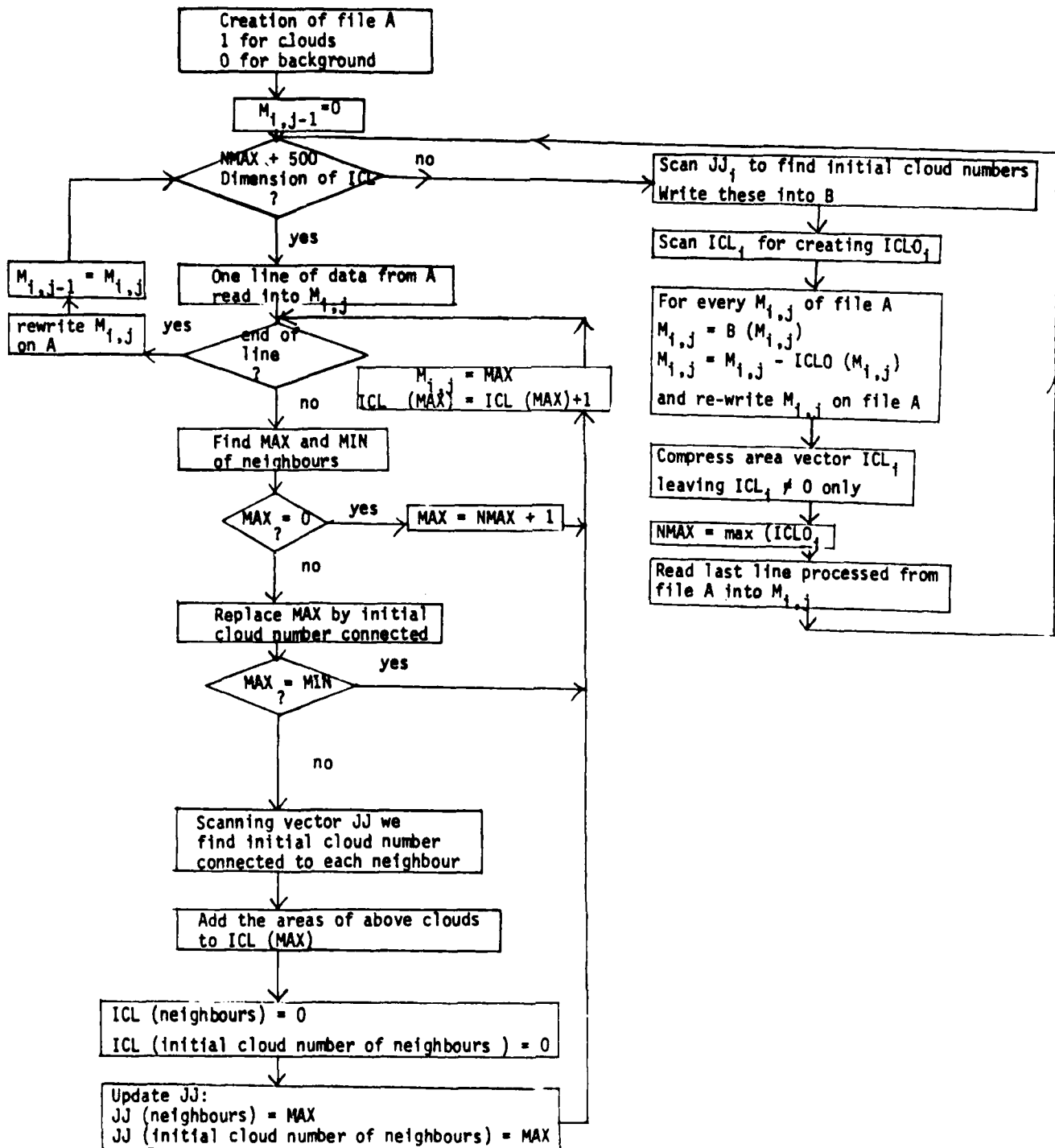


Figure 2.7: The size distribution of holes in clouds.

49 -

MSS =

4

7032

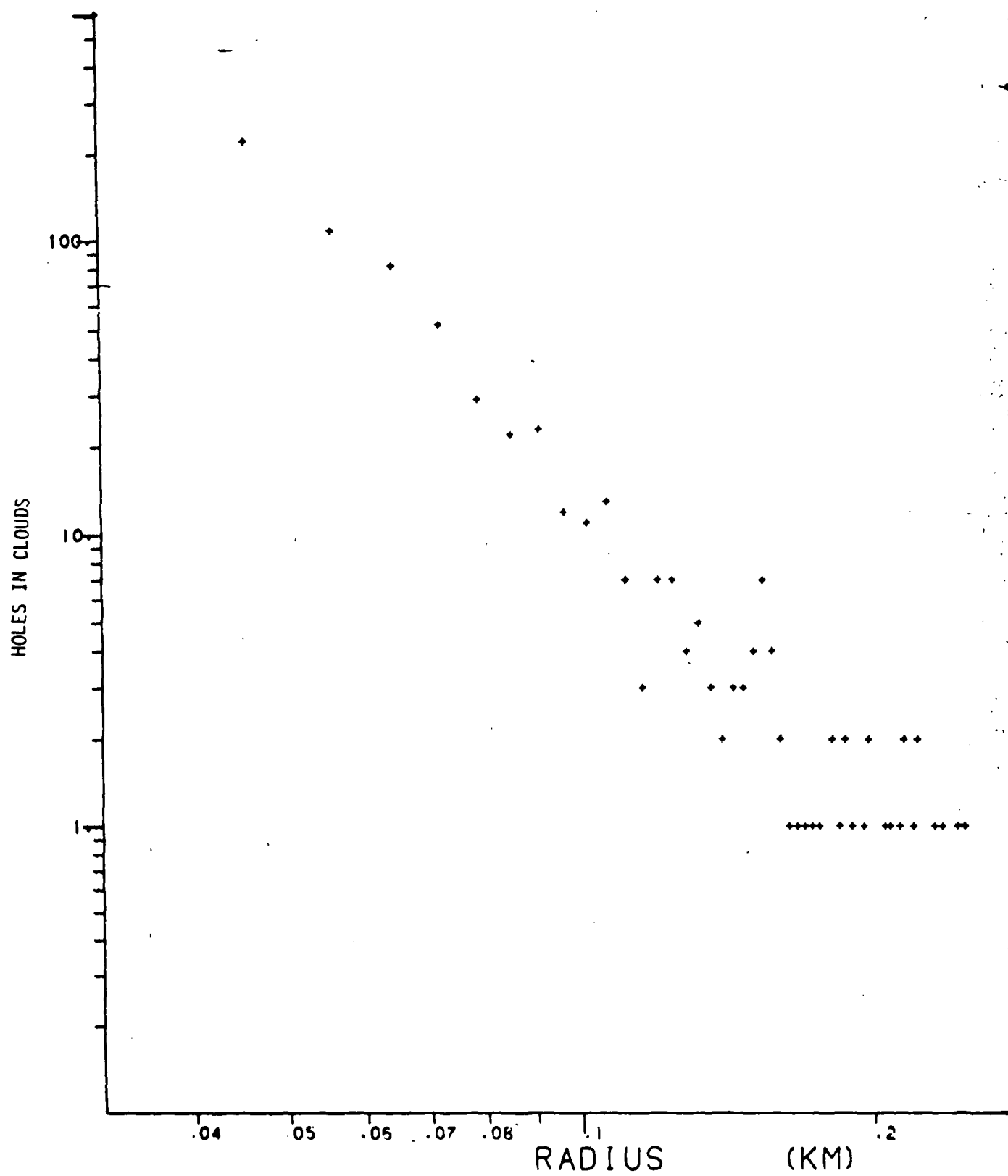


Table 2.1: Variation of cloud parameters with grey level threshold

Image no . 7025, lines 600 - 900, columns 1300 - 1800

<u>Threshold grey level</u>	<u>No. of clouds</u>	<u>No. of small clouds</u>	<u>No. of large clouds</u>	<u>Cloudiness in %</u>	<u>Cloudiness of large clouds in %</u>
MSS - 4: <u>Threshold Chosen - 69</u>					
80	511	146	365	13.2	13.0
78	512	143	369	13.7	13.5
76	513	144	369	14.2	14.0
74	514	134	380	14.7	14.5
72	522	126	396	15.3	15.1
70	511	122	389	15.9	15.8
68	514	124	390	16.6	16.4
66	511	122	389	17.3	17.2
64	513	124	389	18.2	18.0
62	528	129	399	19.1	19.0
60	559	165	394	20.3	20.1
MSS - 7: <u>Threshold Chosen - 2</u>					
10	405	130	275	5.8	5.8
9	411	121	290	6.4	6.2
8	419	112	307	7.1	7.0
7	443	118	325	7.9	7.7
6	449	115	334	8.8	8.7
5	479	135	344	10.0	9.9
4	500	148	352	11.4	11.2
3	514	135	379	13.2	13.0
2	544	149	395	15.8	15.6
1	2507	1961	546	23.5	21.6

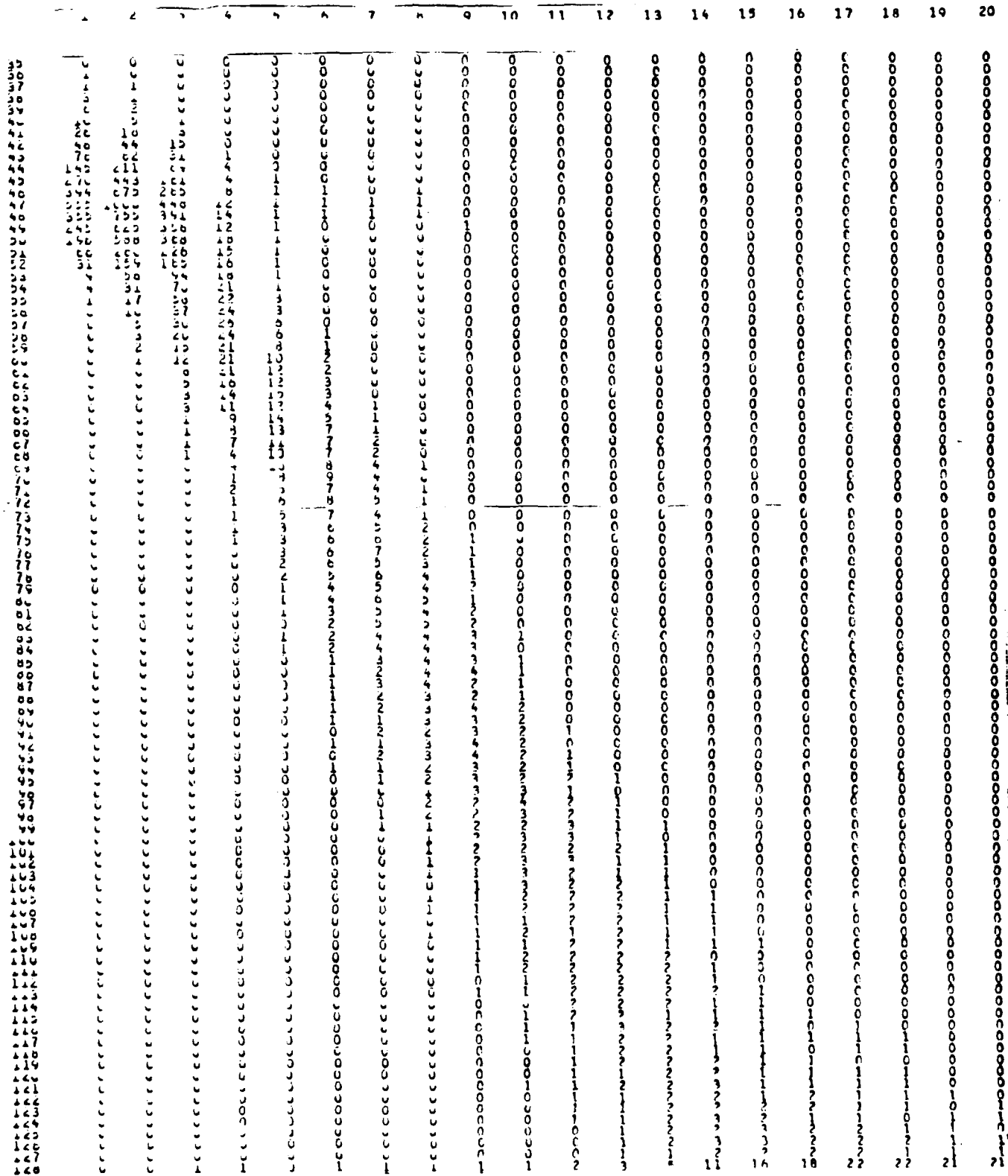
GREY LEVEL OF MSS 4 (1 - 128)

GREY LEVEL OF MSS 7 (1 - 64)

C. PART OF IMAGE 7025, CONTAINING CLOUD AND OCEAN

GREY LEVEL OF MSS 7 (1 - 64)

GREY LEVEL OF MSS 4 (1 - 128)



Chapter 3: The distribution of Cumulus cloud sizes and intercloud distances as derived from LANDSAT

3.1 Introduction

It is widely assumed that clouds act as important moderators of the Earth's radiation balance on both regional and global scales. Solar and thermal radiation fields in the atmosphere are significantly modified by the presence of cloud fields (e.g. Welch et al, 1980, Davies 1978, Joseph and Davies 1985, Harshvardhan and Thomas 1984).

The radiational effects of individual clouds depend on many factors - cloud thickness, cloud top height, cloud vertical and horizontal geometry, the illumination geometry as well as liquid water content, cloud droplet size distribution and atmospheric water vapor profiles. For cloud amounts larger than about 30 percent, several types of cloud-cloud interactions due to the "brokenness" of the cloudiness become important (Welch et al, 1980, Joseph and Davies 1985, Gube et al 1980, Harshvardhan and Weinman 1982, Harshvardhan and Thomas 1984).

Clouds may also be used as diagnostic features in studies of weather and climate. The cloud fields affect temperature, humidity and motion patterns of their ambient atmosphere (e.g. Paltridge 1974a,b, Cox et al, 1973, Reynolds and Cox 1975, Stephens 1976, Fravallo et al, 1981, Schubert et al, 1977, Yanai et al, 1977, Foltz and Gray 1979, Cho 1982, Gray and Jacobson 1977, Fingerhut 1977).

Therefore any study of atmospheric circulations and their accompanying phenomena must take into account the cloud-fields both as to their role in the dynamics of the development and their role as diagnostic features.

Major efforts on the definition and parameterization of cloudiness are underway (e.g. ICCPP). We are engaged in a detailed study of the morphology of broken cloud fields as viewed with high resolution from satellites. The morphology of a cloud field is the geometrical structure of the clouds and their spatial inter-relationships. As stated before, the morphology of cloud fields is strongly connected to atmospheric thermo-hydrodynamics, therefore cloud and cloud field properties can serve as both diagnostics and predictors of atmospheric phenomena. However, the morphology of clouds and cloud fields also has important effects on radiative transfer through a planetary atmosphere. These are:

- (a) Radiative transfer of energy fluxes - e.g. heating phenomena, availability of solar energy at the Earth's surface;
- (b) Radiative transfer of information - e.g. detection of surface features and properties through cloudy layers.

In this paper we summarize some of the initial results of our ongoing analysis of high resolution (70x80 m) of LANDSAT data taken over fair weather cumulus cloud fields in different parts of the world.

3.2 Analysis of LANDSAT Imagery

The sources of information on clouds are many. Each has its peculiar features - positive and negative. A summary of data sources is given in Table 1.

Satellite cloud data are one of the few data bases that are not sparse. They are usually available and on a global basis.

LANDSAT and similar high resolution data have a special place in the study of cloud field features. Detailed analysis of the high spatial frequency variations of the cloud field in parallel with consideration of low frequency (e.g. meteorological satellite data will make it possible to take into account the high frequency effects of cloud fields knowing only the meteorological satellite data. In addition studies of convection and planetary boundary layer dynamics will be much supported by high resolution satellite data.

The imagery available to us is in the form of CCT's with a data density of 6250 b.p.i. of all spectral bands as well as of black and white pictures. Imagery of suitable quality, highest in all bands, and cloudiness 0.1 to 0.6 is chosen from EROS catalogues, principally over the oceans at this stage of our study.

After reading, copying and checking the quality of the tapes, we identify from the black and white pictures of two bands (4 and 7 in the case of LANDSAT S2, 3), the location of the cloudy and clear areas to be analysed.

Histograms of the intensity from these areas are then constructed from which we determine first whether the intensities of the cloud images are saturated or not, viz whether there is a large peak at the highest gray levels. If, as is often the case, the cloud images are in fact saturated, we determine the lower limit of cloud pixel intensities in the following way. The lower limit of cloud pixel intensity is iteratively reduced from a value close to the maximum in both bands till the following conditions are met:

- (a) the total cloudiness approaches the same limit in the two bands,
- (b) the total number of clouds in both bands is approximately equal,
- (c) the ratio of the number of "small clouds" (less than four pixels in area) to total number of clouds increases suddenly, viz the noise level has been reached.

The lower limit varies from image to image and must be arrived at in the above manner.

If the clouds are not saturated, we use one- and two-dimensional histograms of cloudy and cloud-free areas to define the initial cut between clouds and background and then do the analysis described above. Additionally, if the intensities are not saturated we use data from bands 4 and 6 (in the case of Landsat 3) or equivalent bands in Landsats 4 and 5 to determine the cloud height in the following manner.

The height of cloud tops is determined by assuming that the cloud reflectivity does not vary spectrally. The cloud reflectivity can then be deduced from the red or solar I.R. band and used in the blue band to calculate the Rayleigh optical depth of the atmosphere above the cloud. From the optical depth, the pressure and the height are then deduced. A separate paper will be published comparing this method with others - e.g. use of thermal I.R. intensities in LANDSATS 4 and 5 (Joseph, Mekler, Kahn and Podolak, 1986).

The noise of the image was analysed and we made several tests on the efficacy of smoothing e.g. de-spiking, but the effect turned out not to be important for our purposes and consequently was deleted from our procedures.

The process is summarized in Figure 3.1.

The first type of clouds to be studied is Fair Weather Cumulus over sea in low and sub-tropical latitudes.

The reasons for this choice are several. First, it is easiest to develop an analysis technique for small, discrete and bright objects over a darker and usually fairly reasonably homogeneous background. This type of clouds is therefore of intrinsic interest as well as a separate species of clouds.

Our plan is to extend the analysis to clouds over land as well as to include pattern recognition of extended meso- and macro-scale cloud regimes.

In addition to the basic single cloud properties described in this study - size and inter-cloud distance distributions and total cloudiness - we derive also cloud perimeters and cloud top heights as described above, and the distribution of holes in clouds (see next chapter).

In addition, we derive multi-variate properties - the fractal dimension of the cloud field, the relations between the size and inter-cloud distance, the contribution of clouds of different sizes to total cloudiness for 16 intensity ranges, the ratio of cloud to cloud surrounding areas as a function of cloud areas, etc. (see next chapter).

Finally, we connect the various statistics to atmospheric dynamics in several ways.

All these will be presented in subsequent papers for a variety of locations covering the globe.

3.3 The Size Distribution of Clouds

Typical data on the experimental size distribution are given in Figure 3.3. Initially, we fitted the data to an exponential curve in order to compare our results to previous work (e.g. Plank 1969). The part that was fitted is from the minimum size - four pixels or $r_{\min} \sim 64 \text{ m}$ - to a maximum size prescribed by that effective maximum radius beyond which the data degenerate to an irregularly distributed tail of single clouds.

It is clear from the figure that a power law describes the data better than an exponential one. In addition it should be mentioned here that a power law is concomitant with the fractal nature of clouds (Mandelbrot, 1982) which will be dealt with in a subsequent paper. (Cahalan and Joseph 1986).

All our results on the cloud radius distributions are summarised in Table 3.1 and in the Appendices to this report. This table includes the data from previous studies of U-2 photographs (Plank 1969) as well as from that of Hozumi (1982) for cloudiness less than 20%. The other data from Hozumi are for larger amounts of cloudiness in which the type of clouds might be different from ours - Fair Weather Cumulus.

In order to get a visual impression of the data and the possible range of variability we present comparisons of the size-distribution and the accumulated size distribution (integrated backwards) for three cases spanning the range of cloudiness in our study - 0.5 to about 40 percent in figures 3.3(a) to 3.3(j). For each band two figures are shown - the size distribution and the accumulated size distribution (integrated backwards from the largest cloud). The actual data points are situated at the top of each L-shaped segment of the size-distribution histogram and at the right hand edge of the base of the "L" shape in the case of the accumulated distribution curve. The fit to the size distribution is indicated by a sloping line and the cut-off point by a vertical line intersecting the radius coordinate. The largest clouds may not always appear in the size distribution but do appear in the accumulated size distribution. For the sake of comparison all figures are with identical scale. In general

it is clear from the three figures as well as from the Appendices that the size distributions are quite similar for all amounts of cloudiness larger than about two percent . In addition, it is evident that for each image, the two bands give the same result. This constitutes one of the checks in the analysis.

The slopes, beta, of the three size distributions shown, with respect to the effective radius, are almost equal - the average value of the slope of all our data is 2.83 ± 0.20 taking into account ours as well as Plank's relevant data (Hozumi's data were not taken into account because they describe mixed clouds). This is obvious from looking at the Figures 3.3(a) to (j) and the Tables. Only the integration constants, K, differ. The value of the slope is larger than the value of $7/3$ which follows from the clouds being of fractal nature with a dimension of the perimeter of $4/3$ (Lovejoy 1982). Maximal cloud size varies between 0.3 and 2.0 km.

The constant K varies much more from location to location. The present data show no strong correlation of K with P - the percentage of cloudiness - or with any other parameter.

It must be especially emphasized that the slope w.r.t. the areas, A, in a log-log diagram is half the previous value - namely about 1.43. This is important and relevant when one tries to fit the present results to a cloud formation model by convection or by aggregation based on a fractal approach - e.g. D.L.A. of clusters (Family, Private Communications, 1986). It seems that the above results as well as the fractal dimensions of the perimeter - in our case about 1.3 and 1.55 as shown by us in the next chapter - make it reasonable to expect a good fit to one of the cluster aggregation models, (ibid, Private Communication).

Another interesting feature is that the maximal cloud radius in each case seems to be correlated to the cloud amount - the correlation coefficient is over 0.95. For the higher cloud amounts, it is possible that the largest clouds (larger than 10 km^2) may have a different frequency distribution of the cloud areas. This is apparent only in the accumulated size distributions given in the figures - viz. there may be a change in slope beyond 10 km^2 .

3.4 The Distribution of Minimal Distances Between Pairs of Cloud Centers

For each cloud in a given sample, we find the coordinates of its "center of gravity". Then, for any given cloud, we find the one other cloud that is closest to it in terms of the distance between the two "centers of gravity" in two circumstances - first all clouds are taken into account and secondly only those clouds that are at least one tenth larger than the area of the cloud in question. One example of the distribution of these distances is given in Fig. 3.4a and 3.4b in the two spectral bands analysed, MSS4 and MSS7, showing again that the same results are obtained in both.

The distribution is strongly peaked - in both spectral bands analysed - at a value of about 0.5 km. This peakedness is a feature common to all distributions. Some representative data are given in Table 3 in the form of fits to log-normal distributions. This seemed to be a natural choice due to both the shape of the curves as well as to the common occurrence of that distribution in many studies of cloud physics (e.g. Lopez 1977).

In addition, the log-normal distribution may be a result of the cloud formation process (e.g. Lopez 1977).

A fairly surprising result is that the values of P_1 and (especially) P_2 are very similar for all locations - not only those shown in the table. This may be due to similar conditions of convection at all locations - mid morning fair weather cumulus.

The fit to a log-normal may however not be the optimal approach. In a separate note, we show (Cahalan and Joseph 1986) that for a random distribution of cloud centers in the plane one should expect a distribution of a different type. We therefore decided to try and fit the experimental histogram of the distances between nearest neighbours using different assumptions. We assumed that the probability of finding a cloud center at distance r from any other one is given by

$$W(s) ds = [1 - \int_0^s W(s') ds'] 2\pi sn f(s) ds \quad (1)$$

where the expression in square brackets gives the probability of not finding a cloud at a distance

$$s' < s$$

and

$$2\pi s n ds$$

gives the random probability of finding a cloud center in an annulus of radius s of area $2\pi s ds$ and when the average density of cloud center is n . The function $f(s)$ describes the deviation from a random distribution in the plane.

Equation (1) is solved by us and its implications are more fully discussed in another paper (Cahalan and Joseph 1986). Here we present results assuming that

$$f(s) = s^{(N-1)} \quad (2)$$

and that therefore

$$W(s) = 2\pi n s^N \exp\{-2\pi n s^{(N+1)}/(N+1)\} \quad (3)$$

Therefore $N > 1$ implies deviation from a random distribution of clouds in the plane, such that the probability of finding a cloud distanced s from the center cloud increases with s . We therefore show the same data as before but fitted to such a function in Table 4.

Again the similarity of n and b at different locations are often striking, but in addition the fact that n is often close to one shows that the distribution of cloud centers in the plane is then close to random. The reason for the latter conclusion is that a purely random distribution would result in a value of one for the power N (Cahalan and Joseph 1986).

In order to give a further impression of the features of the distribution of minimal distances between cloud centers, we present Figures 3.5(a), (b) and (c) for amounts of cloudiness of 1.4, 13.5 and 32.9 percent respectively. The figures are for one band only (MSS4) as the results for the other one are similar. The histograms are not normalised but it is easy to check that normalisation to a constant number of "large clouds" (cloud with areas larger than four pixels), will make all three peaks coincide within the experimental error.

Superposed on the experimental data - the crosses - are the two fits that we used - the log - normal and the Weibull distributions. The two fits give similar results, except for the region of minimal distances larger than 2 km, where the Weibull function decreases too rapidly. One may conclude that the log-normal distribution is the one to adopt, similarly to the usage in most other studies on cloud properties (Lopez 1977). However, in our opinion, the experimental data are not good enough for such a conclusion - they indicate a distribution with a given peak and width only. It may however, be important to reach a definite conclusion because of the physical phenomena behind each distribution (e.g. *ibid* 1977).

We investigated statistically the possible correlations between the amount of cloudiness, the number of "large" and "small" clouds and their ratio and the coefficients of the two fits (See Appendices).

The only significant correlation is that between the amount of cloudiness and N , the exponent of the Weibull distribution. It is low when one takes into account all data - 0.31. When one successively increases the lowest amount of cloudiness taken into account, the correlation increases rapidly and reaches 0.87 for cloudiness larger than 15 percent and 0.92 for cloudiness larger than 20 percent. The values of cloudiness for which N is equal to one - an indication of randomness in the distribution of cloud centers - varies between 10 and 18 percent. This is reasonable in terms of experience. Fair Weather Cumulus clouds usually exhibit a random distribution for such low amounts of cloudiness.

3.5 Discussion and Summary

This study presents the initial results of an analysis of the statistical distribution functions of cloud size and minimal inter-cloud distances at seventeen locations spread over the world's oceans. These single cloud properties are a necessary first step in a study of the complex morphology of broken cloud fields and the application of the latter to relevant problems in atmospheric physics.

The type of clouds analysed - Fair Weather Cumulus - is an important widely and frequently occurring type and represents the prevalence of convection in the atmospheric boundary layer. Fair Weather Cumulus clouds usually have aspect ratios of about one (e.g. Plank 1969, Gagin 1983 private communication) so that our cloud radii distributions are also representative of the thicknesses of these non-raining clouds. The cloud thickness will be proportional to twice the effective radius found.

Some interesting commonalities have been observed in the distributions found at different locations. First, a power law fits the size distributions best. The power, β , is fairly similar from location to location, 2.83 ± 0.20 , and is slightly larger than $7/3$, the value resulting for clouds assumed to be self-similar fractals.

The constant K of the power law, $Kr^{-\beta}$ varies more from location to location and is weakly correlated to the cloud amount as shown in Section 3.

The number of clouds tends to decrease with the amount of cloudiness similarly to the previous results from different times of day at the same location (Plank 1969). This brings us to a basic deficiency in the LANDSAT data, namely the fact that they are available at one time of day only - mid-morning. This is of course partly off-set, but not corrected, by the possibility of analyzing many locations globally using the same instrumentation.

In the future, our data in order to be more fully useful, will need to be augmented by observations at other times of day (e.g. by use of airplanes).

In addition, it is important to extend the lower limit of resolution by analysis of imagery from other sources (Thematic Mapper, SPOT Satellite and airplanes). This point will be gone into more fully in subsequent papers dealing with the fractal property of the cloud field and its applications.

The fit of the minimal inter-cloud distances to a function given by:

$W(s) = 2\pi ns^N \exp, < - 2\pi ns^{(N+1)}/(N+1), >$ shows that in many cases studied the areal distribution of clouds is close to random - $N \sim 1$, especially for cloudiness lower than 20 percent. This same power, N , may thus serve as an indication of the deviation from randomness e.g. the cloud field west of Israel over the Mediterranean. Much additional information on the nature of the convection may be ~~derived~~ and will be reported on separately.

Further analysis of imagery at other locations is in progress as well as various applications to problems in atmospheric physics.

One other point which should be emphasized here is the extreme difficulty of developing a reliable semi-automatic data analysis scheme. Great effort went into the latter's development and a significant part of the project time was spent studying, checking and implementing the various possible methods.

Our U.S. counterpart took upon himself, inter alia, the analysis of different aspects of the problem, e.g. the perimeter - area relationships of the smallest clouds, close to the limit of resolution - and consequently was able to analyse in depth one image. His study was however, fundamental to the development of our approach in Israel, and will be reported separately.

3.6 Acknowledgements

The continuous and able scientific programming efforts of Mrs. S. Rechavi, Z. Rosen and S. Adler were a very important factor in the success of this study.

The advice and cooperation of Drs. Y. Mekler and R. Kahn are gratefully acknowledged.

This study was funded by Grant AFOSR-83-0239 of the USAF and partly by BSF Grant 3039/82 of the US-Israel Bi-National Science Foundation.

3.7 References -

- Cahalan, R.F. and J.H. Joseph, 1986: A statistical model for the horizontal distribution of Cumulus clouds (to be submitted).
- Cho, H.R. 1978: Some statistical properties of a homogeneous and stationary shallow cumulus cloud field: J. Atmos. Sci. 35, 125-138.
- Cox, S.K., 1969: Radiation models of mid-latitude synoptic features: Mon. Wea. Rev. 97, 637-651.
- Davies, R. 1978: The effect of finite geometry on the three-dimensional transfer of solar irradiance in clouds. J. Atmos. Sci. 35, 1712-1725.
- Fingerhut, W.H. 1977: A numerical model of a diurnally varying tropical cloud cluster disturbance. Paper prepared for U.S. Workshop on the GATE Central Program, NCAR, Boulder, 25 July, 39 pp.
- Foltz, G.S. and W.M. Gray, 1979: Diurnal variation in the troposphere's energy balance. J. Atmos. Sci. 36, 1450-1466.
- Fravalo, C., Y. Fouquart, R. Rosset, 1981: The sensitivity of a model of low stratiform clouds to radiation. J. Atmos. Sci. 38, 1049-1062.
- Gray, W.M. and R. W. Jacobson Jr., 1977: Diurnal variation of deep cumulus convection. Mon. Wea. Rev. 105, 1171-1188.
- Gube, M., J. Schmetz, E. Raschke., 1980: Solar radiative transfer in a cloud field. Contrib. Atmos. Phys. 53, 24-34.
- Harshvardhan and J.A. Weinman, 1982: Infrared radiative transfer through a regular array of cuboidal clouds. J. Atmos. Sci., 39, 431-439.
- Hozumi, K., T. Harimaya, C. Maono, 1982: The size distribution of Cumulus clouds as a function of cloud amount. J. Met. Soc. Japan, 60, 691-699.
- Harshvardhan and R.W.L. Thomas, 1984: Solar reflection from interacting and shadowing cloud elements J. Geophys. Res., 89, 7179-7185.
- Joseph, J.H., Y. Mekler, R. Kahn, M. Podolak, 1986: The determination of cloud top height from LANDSAT Imagery (to be submitted).
- Joseph, J.H. and R. Davies, 1986: The albedo of broken Cumulus cloud fields, (to be submitted).
- Lopez, R.E., 1977: The lognormal distribution and Cumulus cloud populations. Mon. Wea. Rev., 105, 865-872.
- Lovejoy, S. 1982: Area perimeter relation for rain and cloud areas. Science, 216, 185-187.

Paltridge, G.W., 1974a: Atmospheric radiation and the gross character of stratiform clouds: J. Atmos. Sci. 31, 244-250.

Paltridge, G.W., 1974b: Global cloud cover and earth surface temperature. J. Atmos. Sci., 31, 1571-1576.

Plank, V.G. 1969: The size distribution of Cumulus clouds in representative Florida populations. J. Appl. Met. 8, 46-67.

Reynolds, D.W., T.H. Vonder Haar and S.K. Cox, 1975: The effect of solar radiation absorption in the tropical atmosphere: J. Appl. Met. 14, 433-444.

Schubert, W.H., J.S. Wakefield, E.J. Stelmer and J.K. Cox, 1977: Marine strato Cumulus convection: Atmos. Sci. Paper 273, C.S.U. 140 pp (NTIS PB 272955/AS).

Stephens, G.L., 1976: The transfer of radiation through vertically non-uniform strato-cumulus clouds. Beitr. Phys. Atmos. 49, 237-253.

Welch, R.M., S.K. Cox, J.M. Davies, 1980: Solar radiation and clouds Meteorological Monographs, Vol. 17, AMS, 45 Beacon St., Boston, MA 02108 pp. 96.

Yanai, M., S. Esbensen, J. Chu, 1973: Determination of bulk properties of tropical cloud clusters from large-scale heat and moisture budgets. J. Atmos. Sci., 30, 611-627.

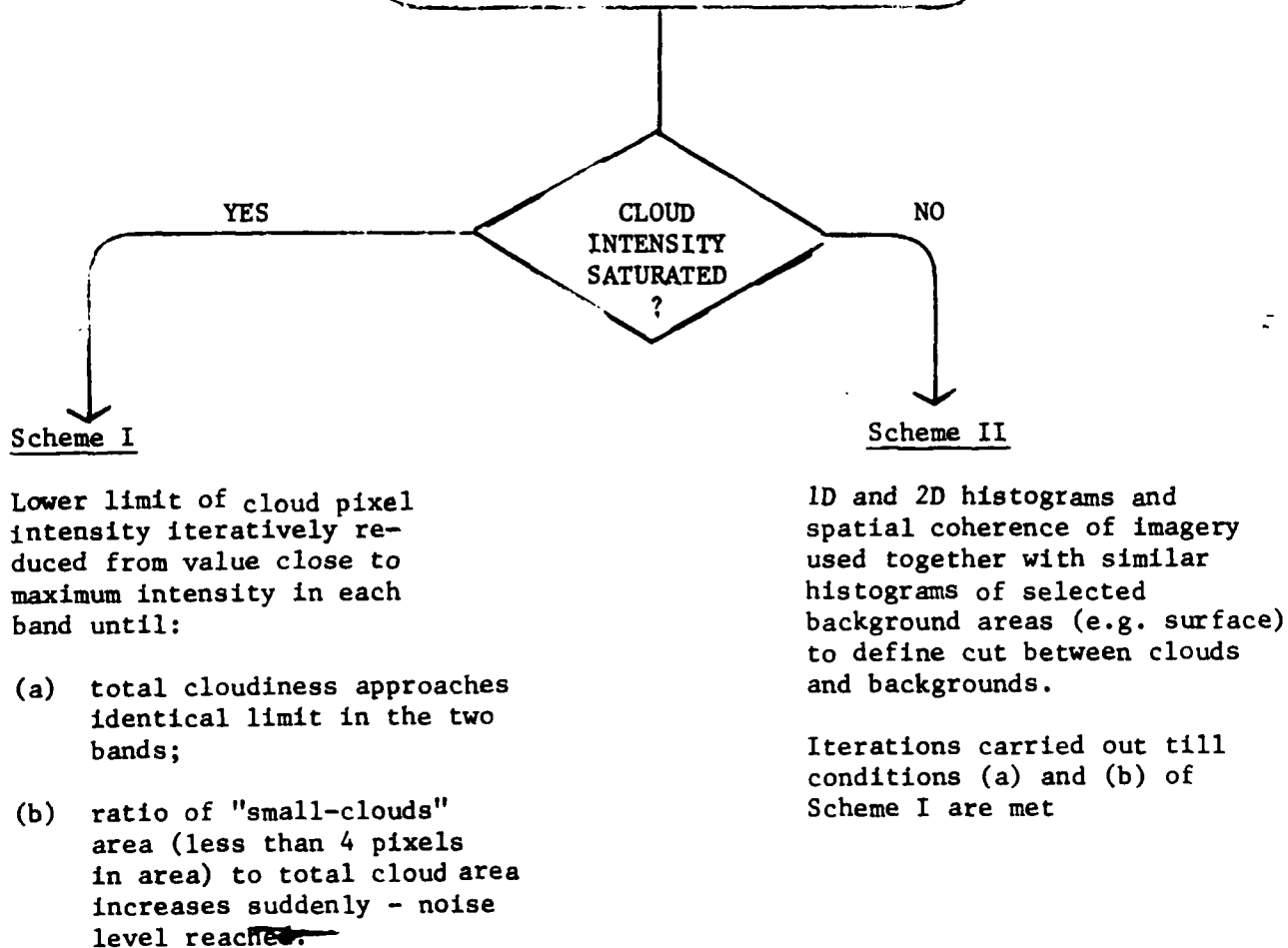
FIGURE 3.1: ANALYSIS OF LANDSAT IMAGERY

BASIC PROBLEM OF DATA ANALYSIS:

DISCRIMINATION BETWEEN CLOUDS AND BACKGROUNDS

BASIC TOOLS

Histograms of Spectral Intensity
Bands 4, 6 and 7 used
(generally 4 and 7 only)



Note: Height cannot be determined when bands saturated

Figure 3.2: Comparison of exponential and power-law fits to the experimental data on cloud radius

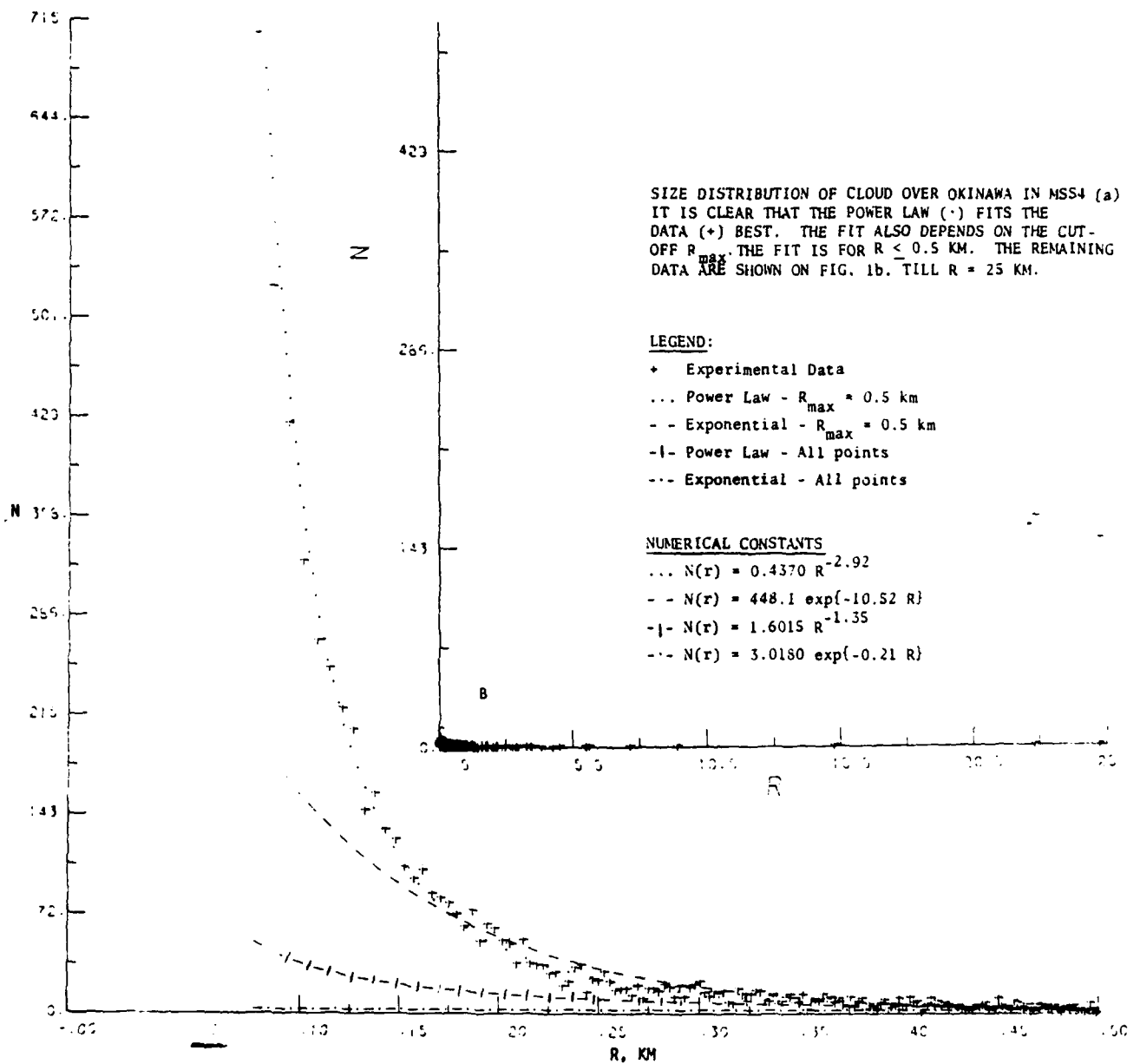
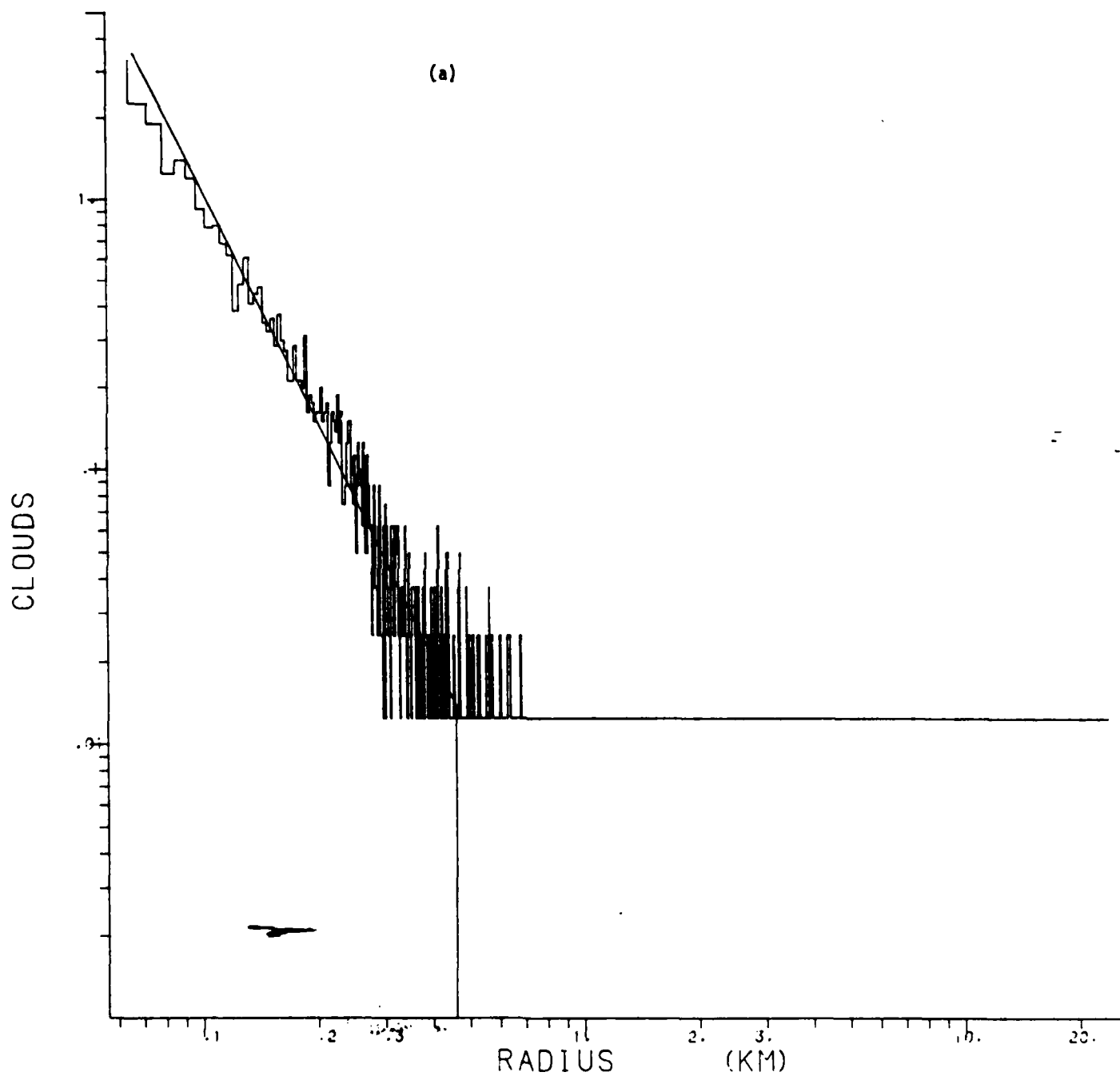


Figure 3.3: Size distribution and accumulated distributions for three cases.
Spanning the range of observed cloudiness

MSS=

4

7024



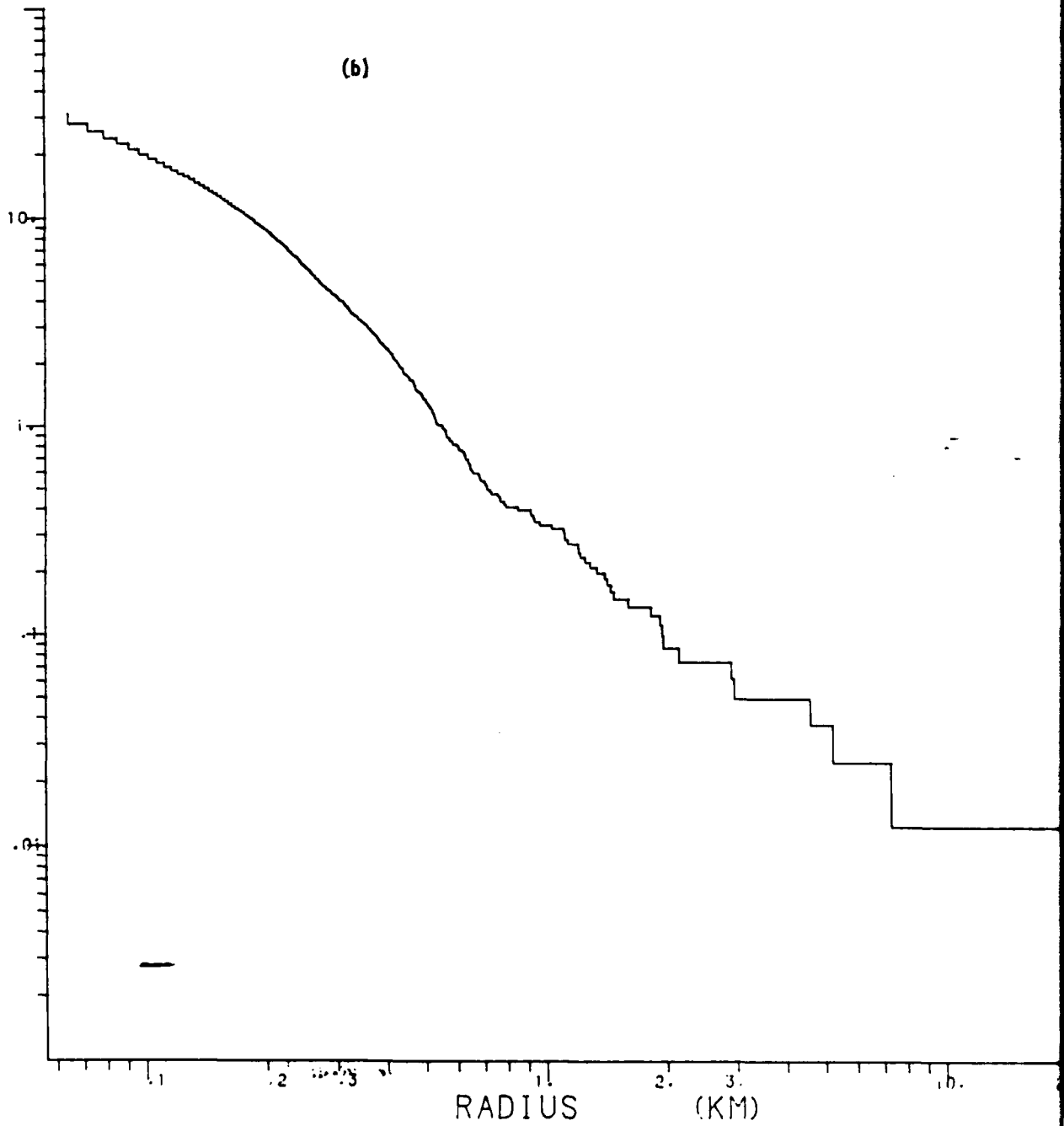
MSS=

4

7024

(b)

AC. CLOUDS BKWD



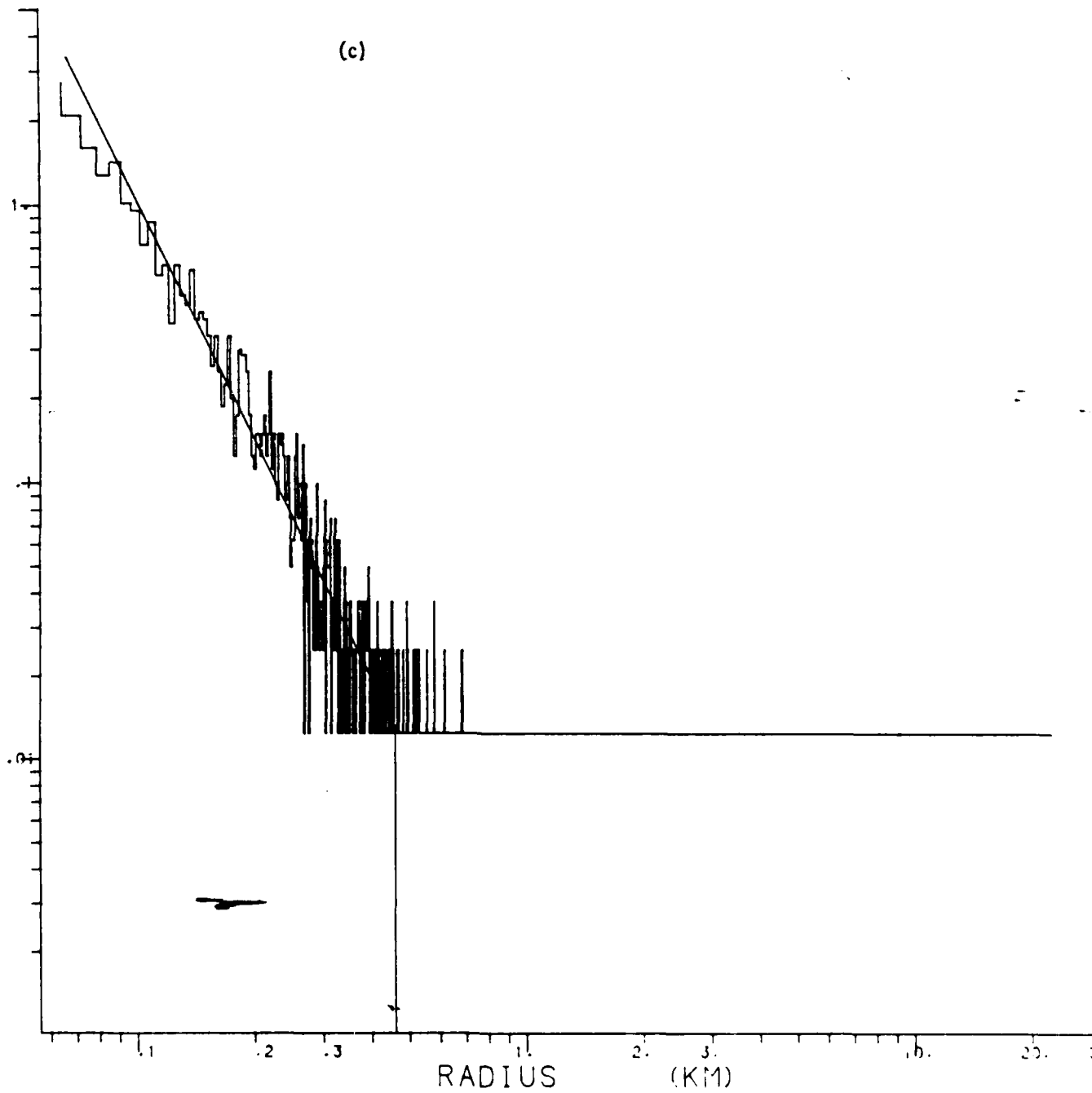
MSS=

7

7024

(c)

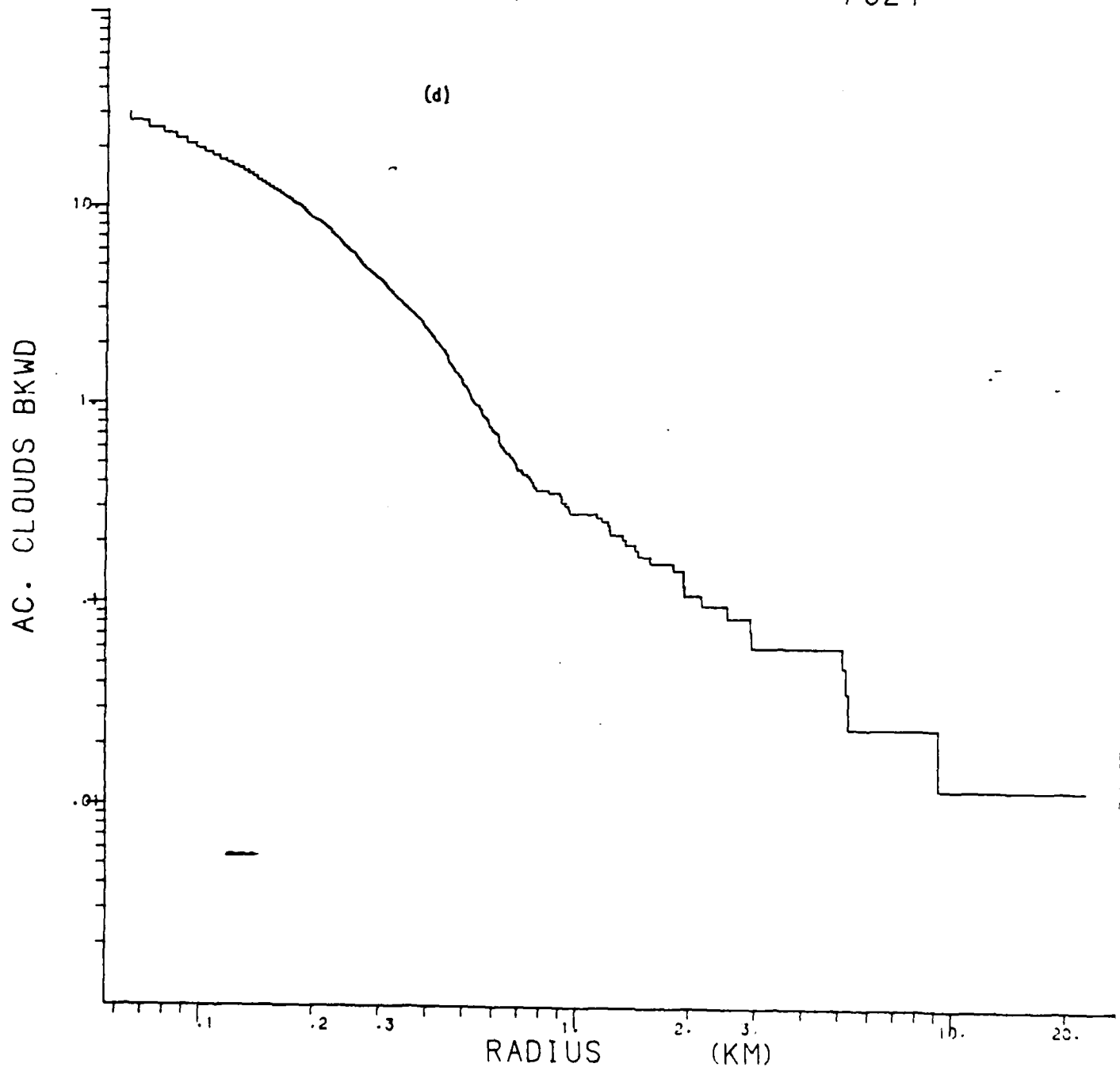
CLOUDS



MSS=

7

7024



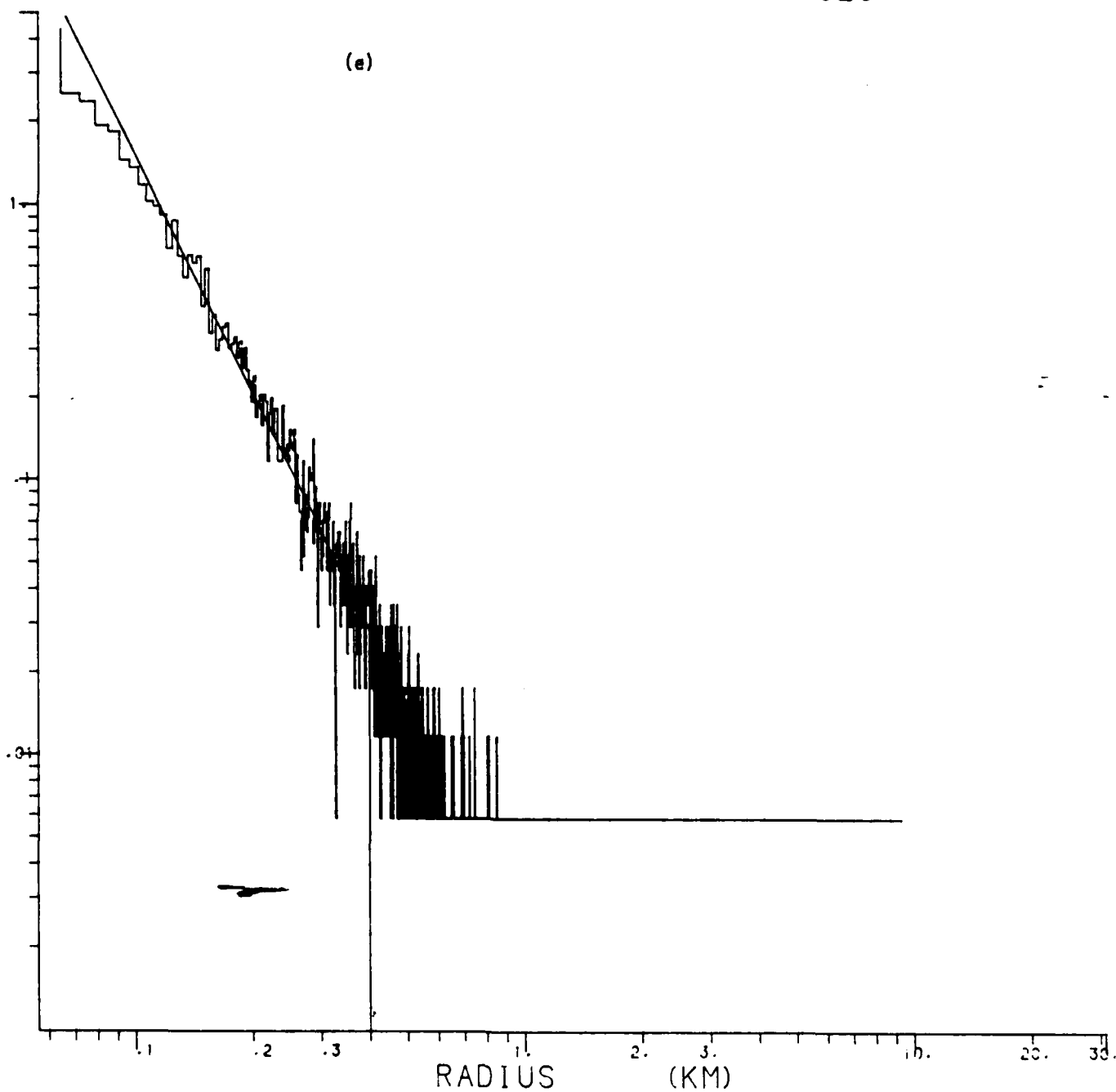
MSS=

4

7025

(a)

CLOUDS

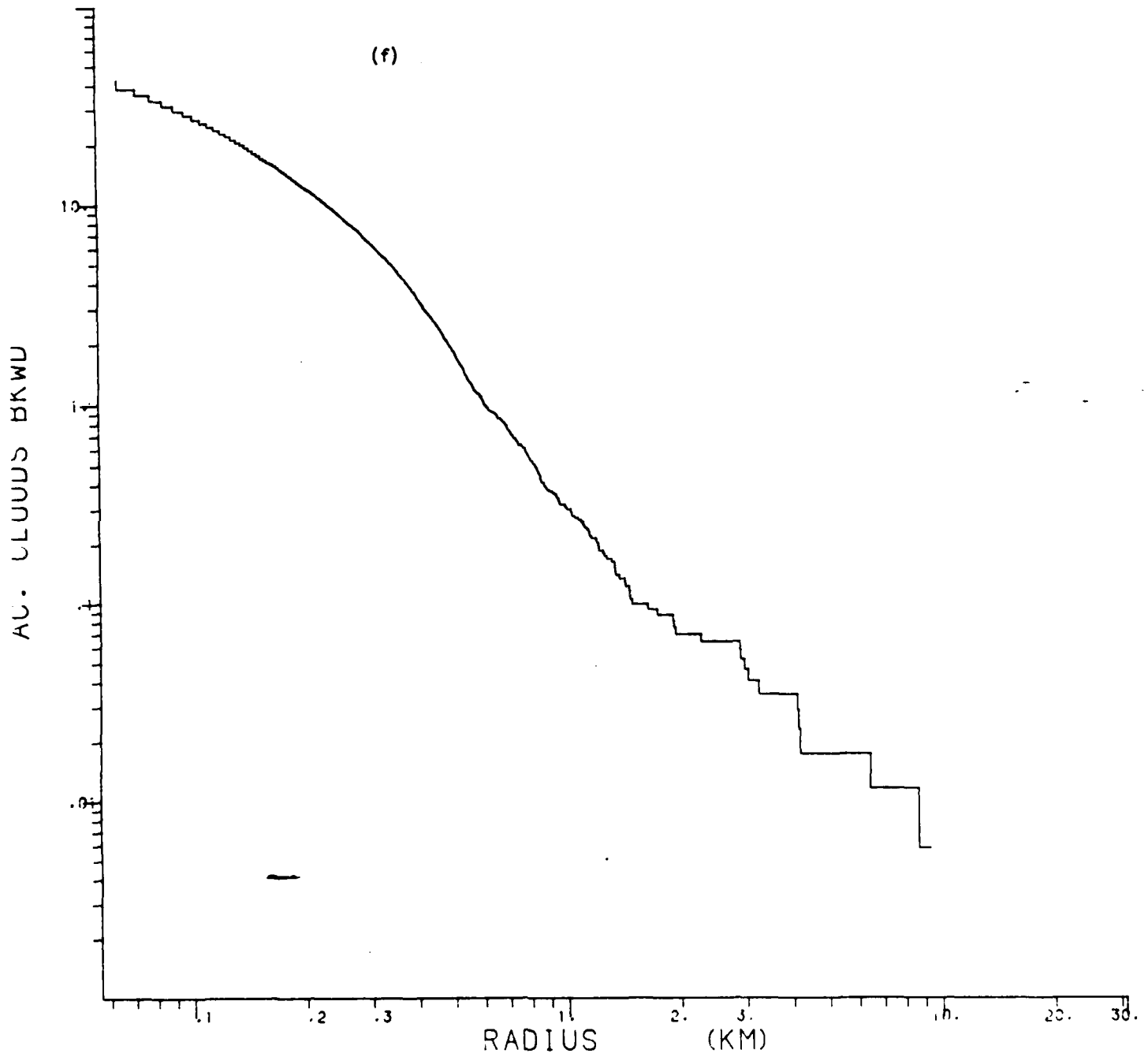


MSS=

4

7025

(f)



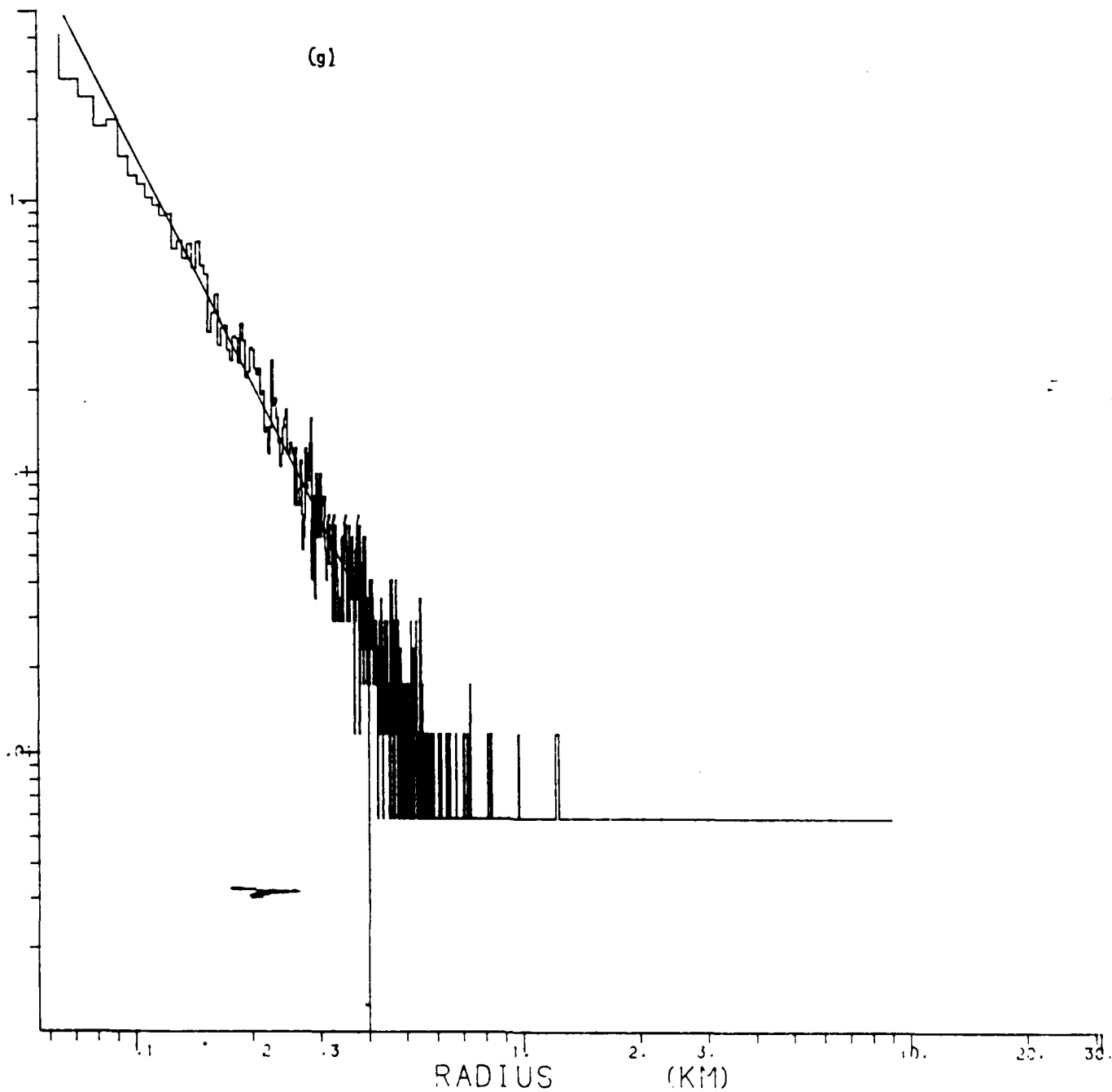
MSS=

7

7025

(g)

CLOUDS



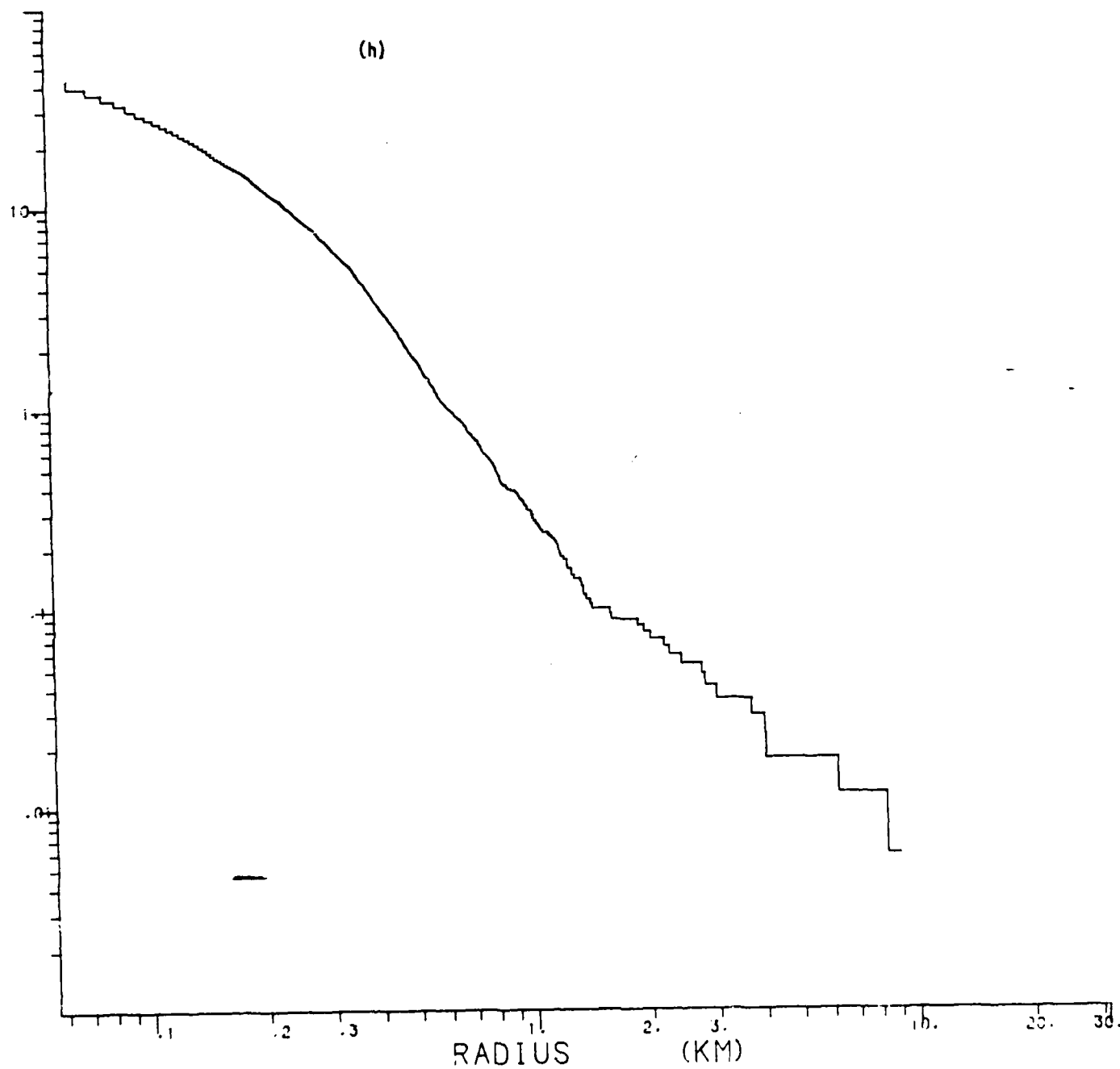
MSS=

7

7025

(h)

AC. CLOUDS BKWD

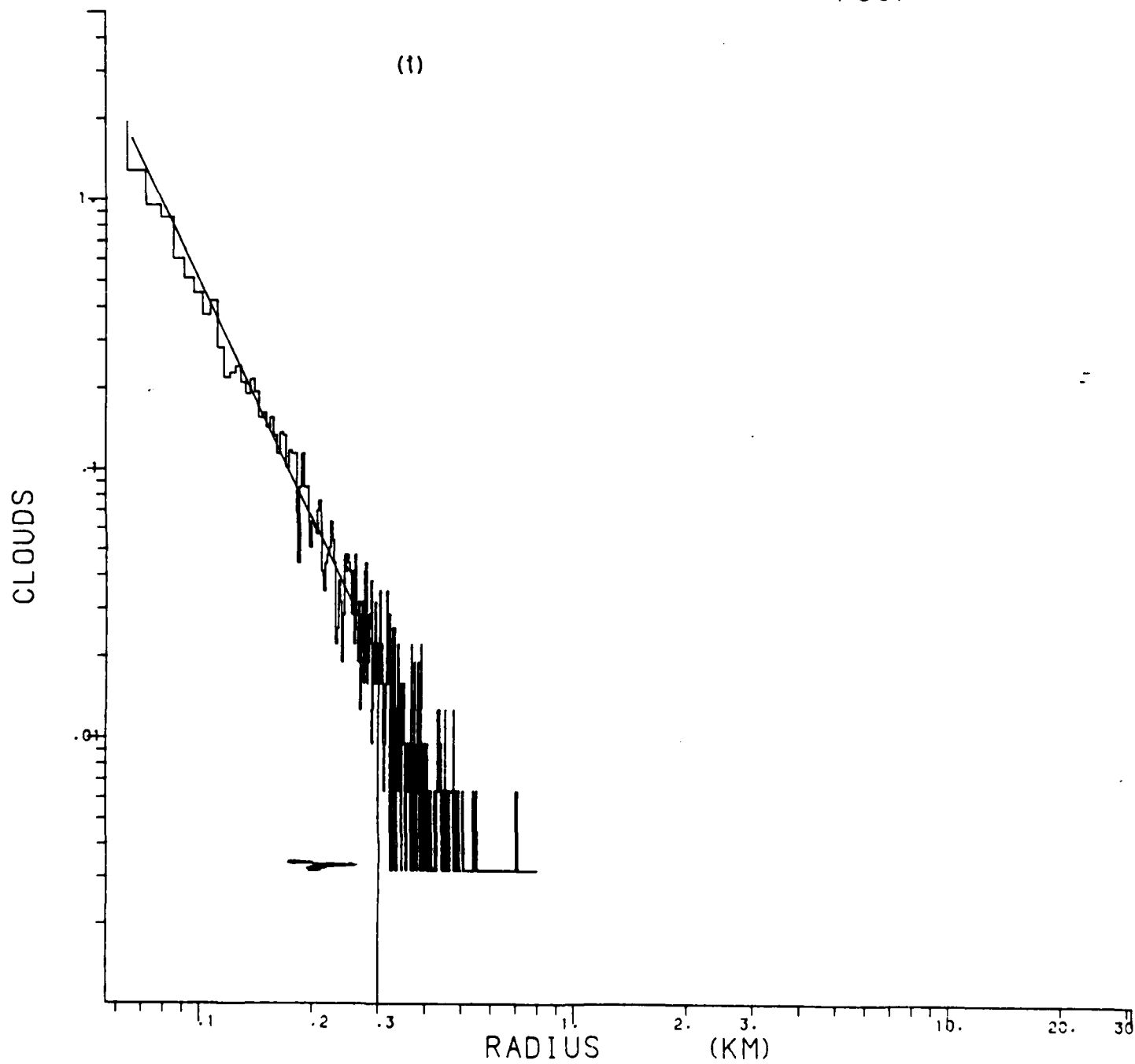


MSS=

4

7067

(1)



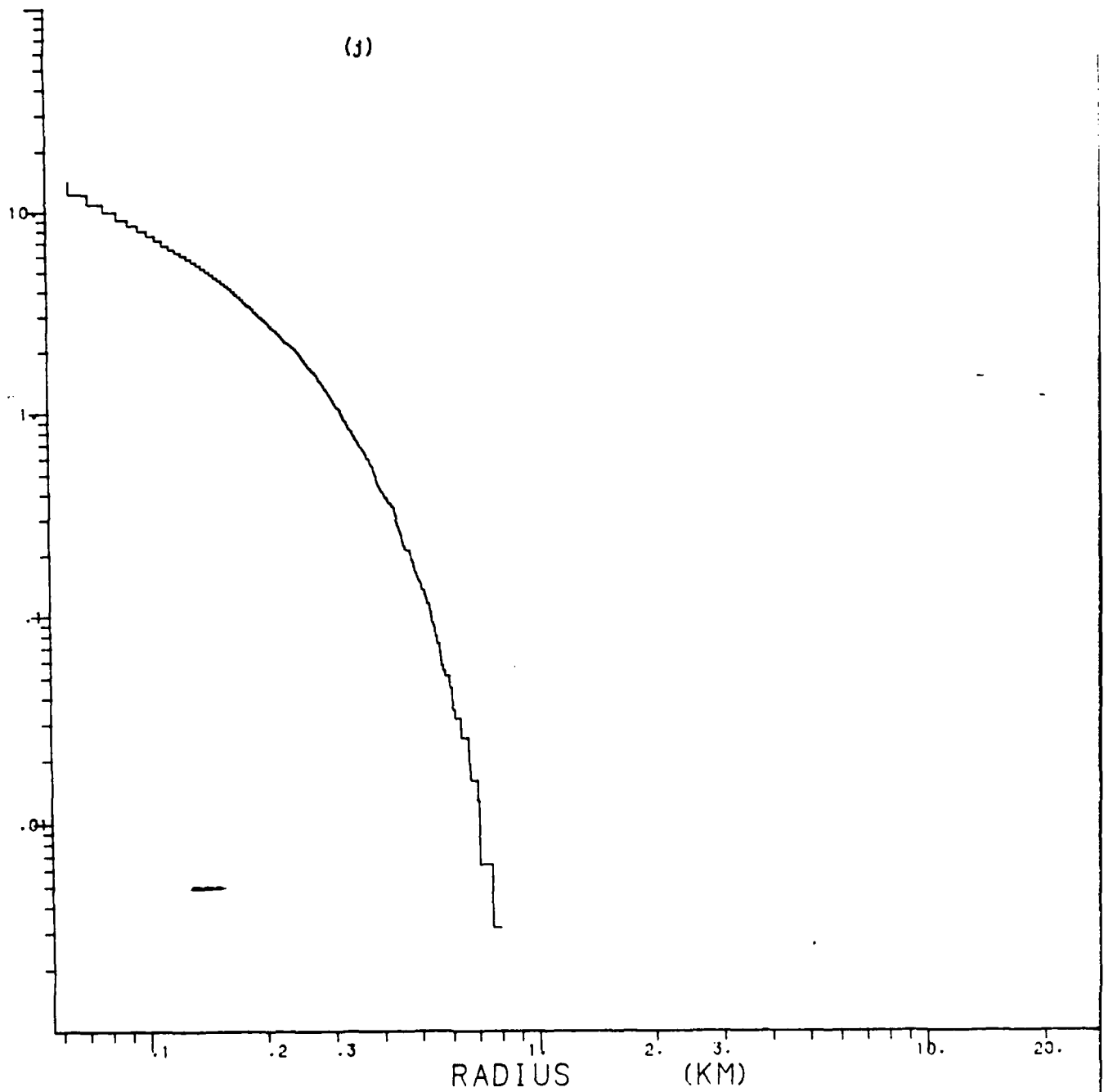
MSS=

4

7067

(j)

AC. CLOUDS BKWD

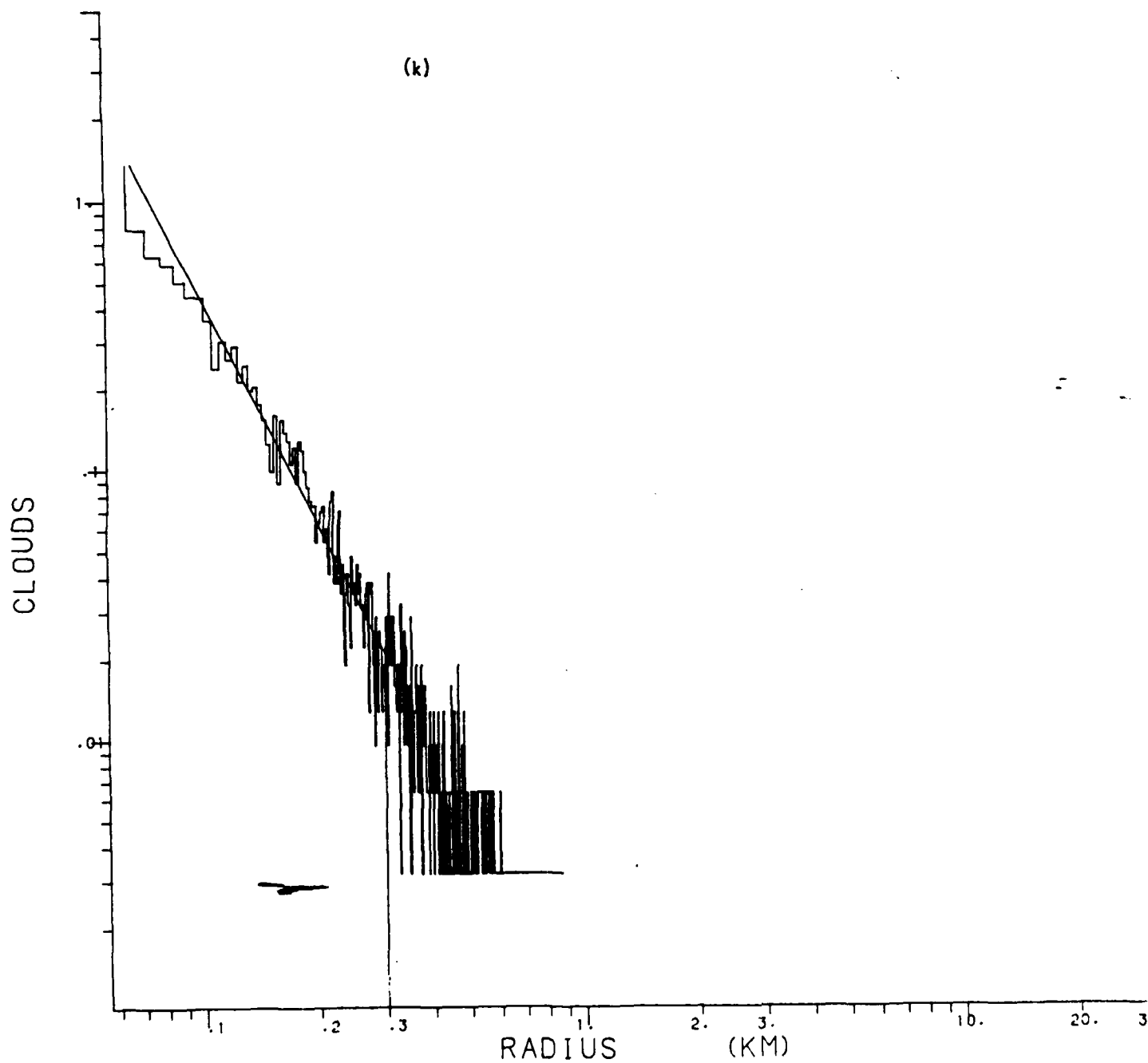


MSS=

7

7067

(k)



MSS=

7

7067

(1)

AC. CLOUDS BKWD

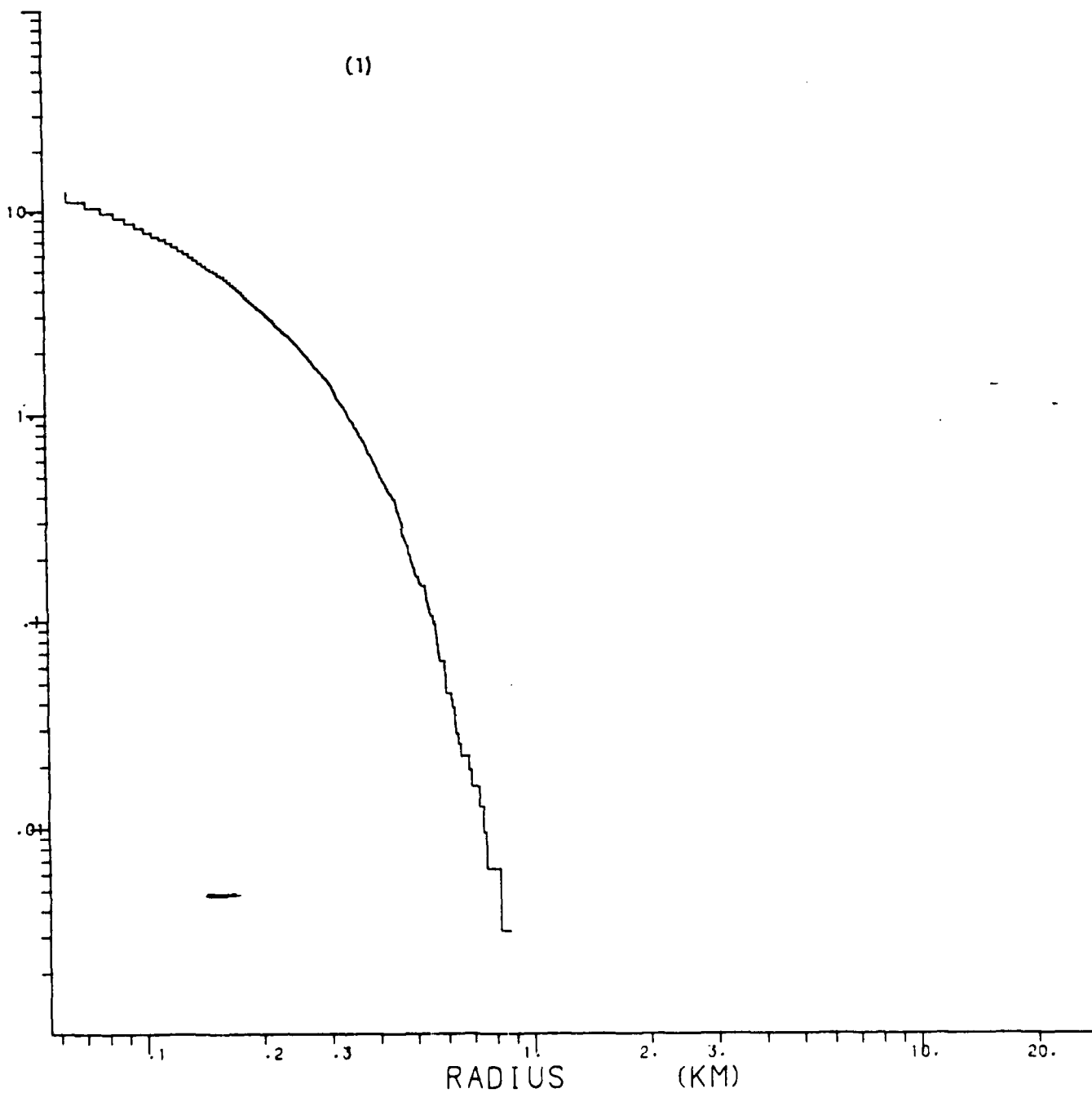


Figure 3.4: Histograms of minimal distances between cloud centers for bands MSS4 and 7 in case 7032 (See Appendix).

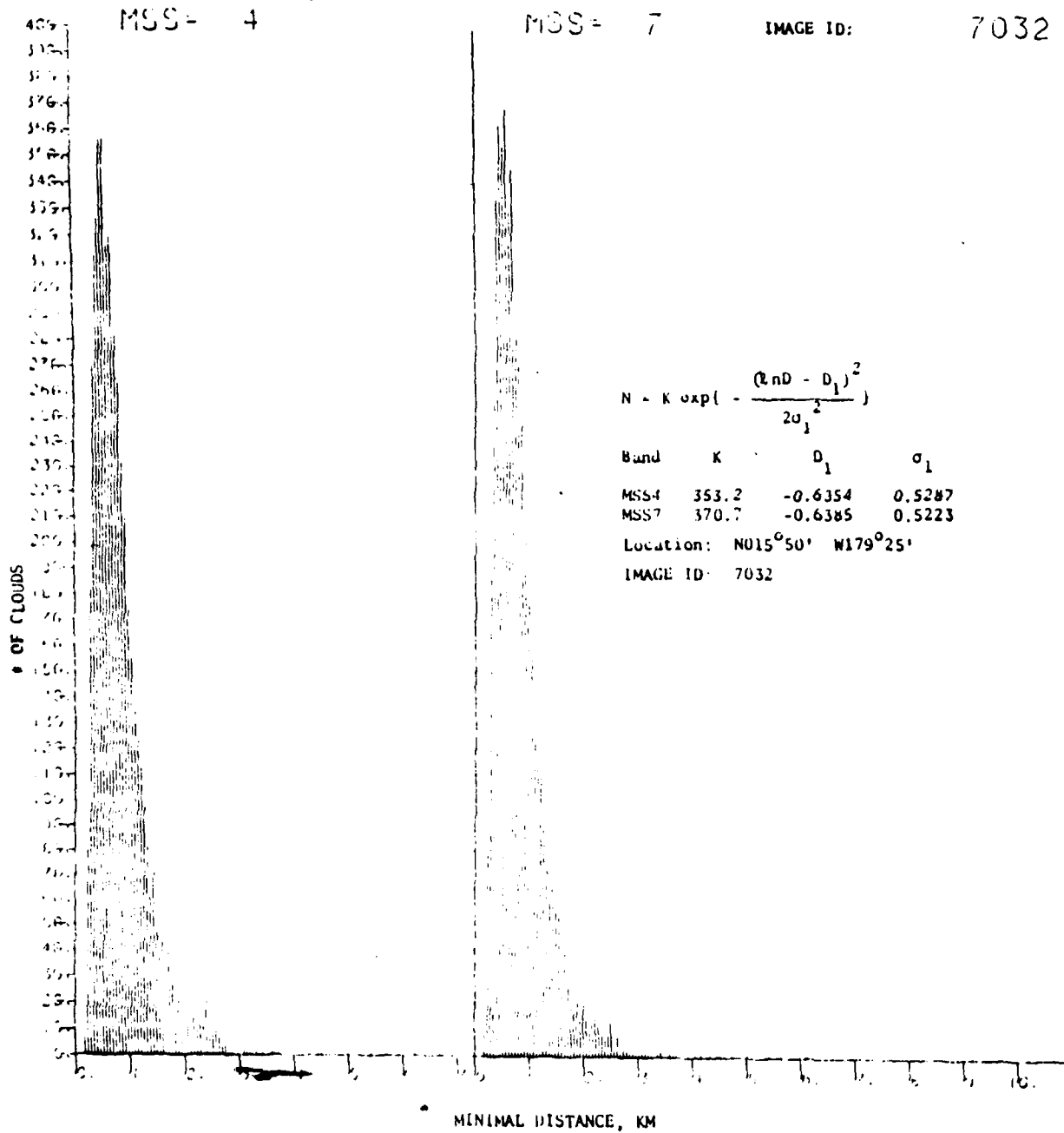
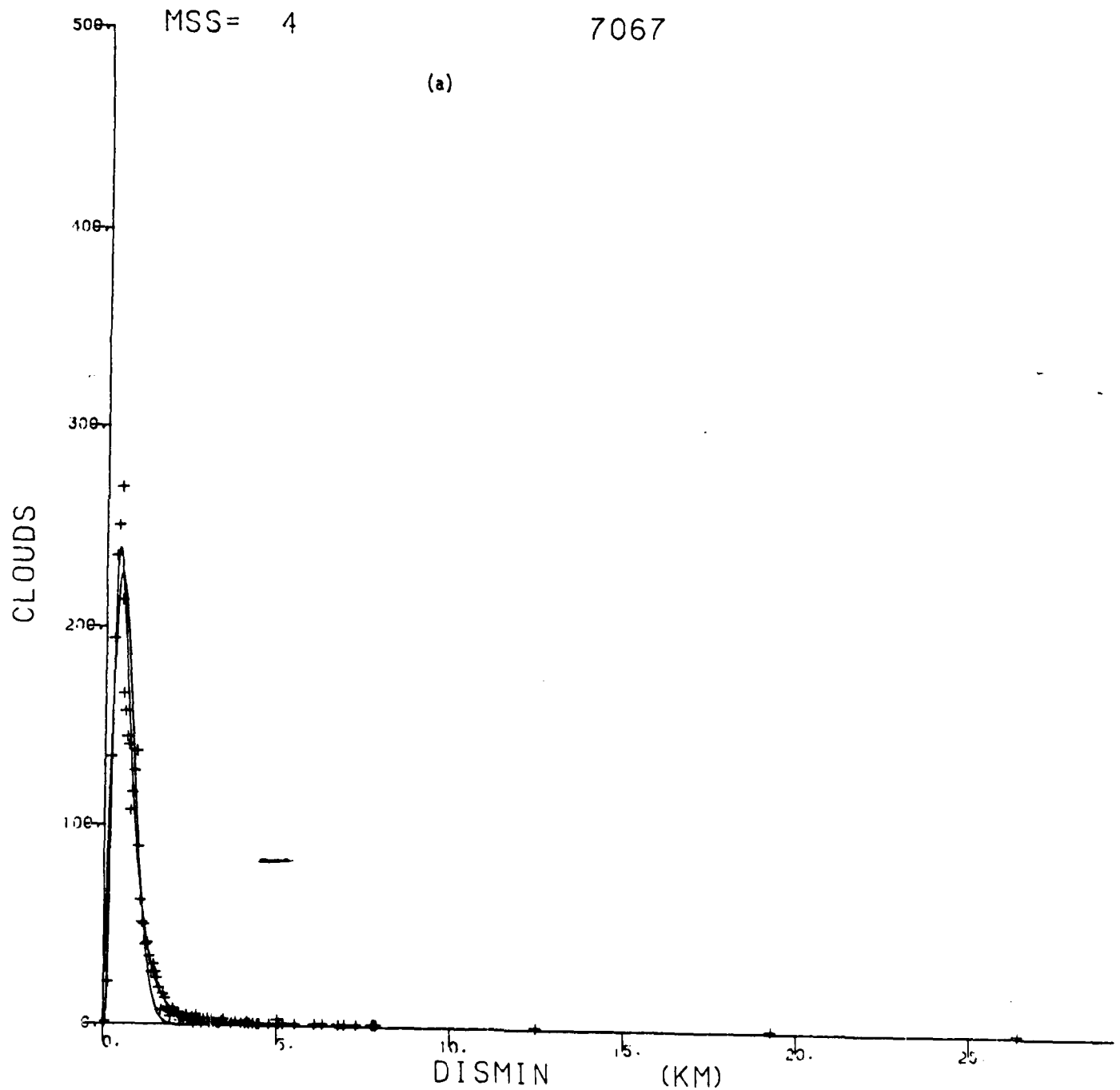
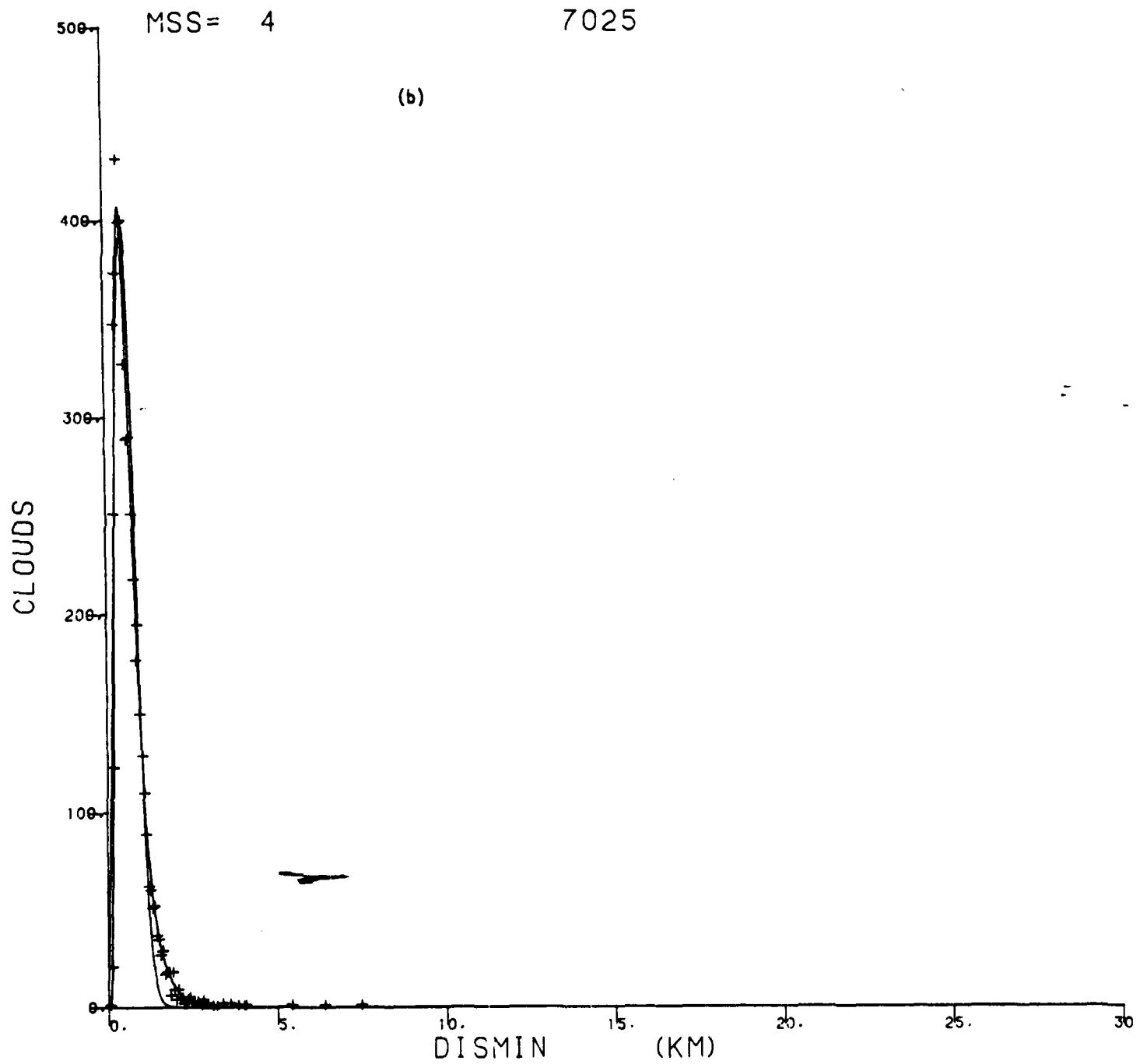


Figure 3.5: The distribution function of minimal distance between cloud centers for three cases spanning the range of cloudiness observed - (a) Case 7067, cloudiness 1.4%; (b) Case 7025, cloudiness 13.5%; (c) Case 7024, cloudiness 32.9%.





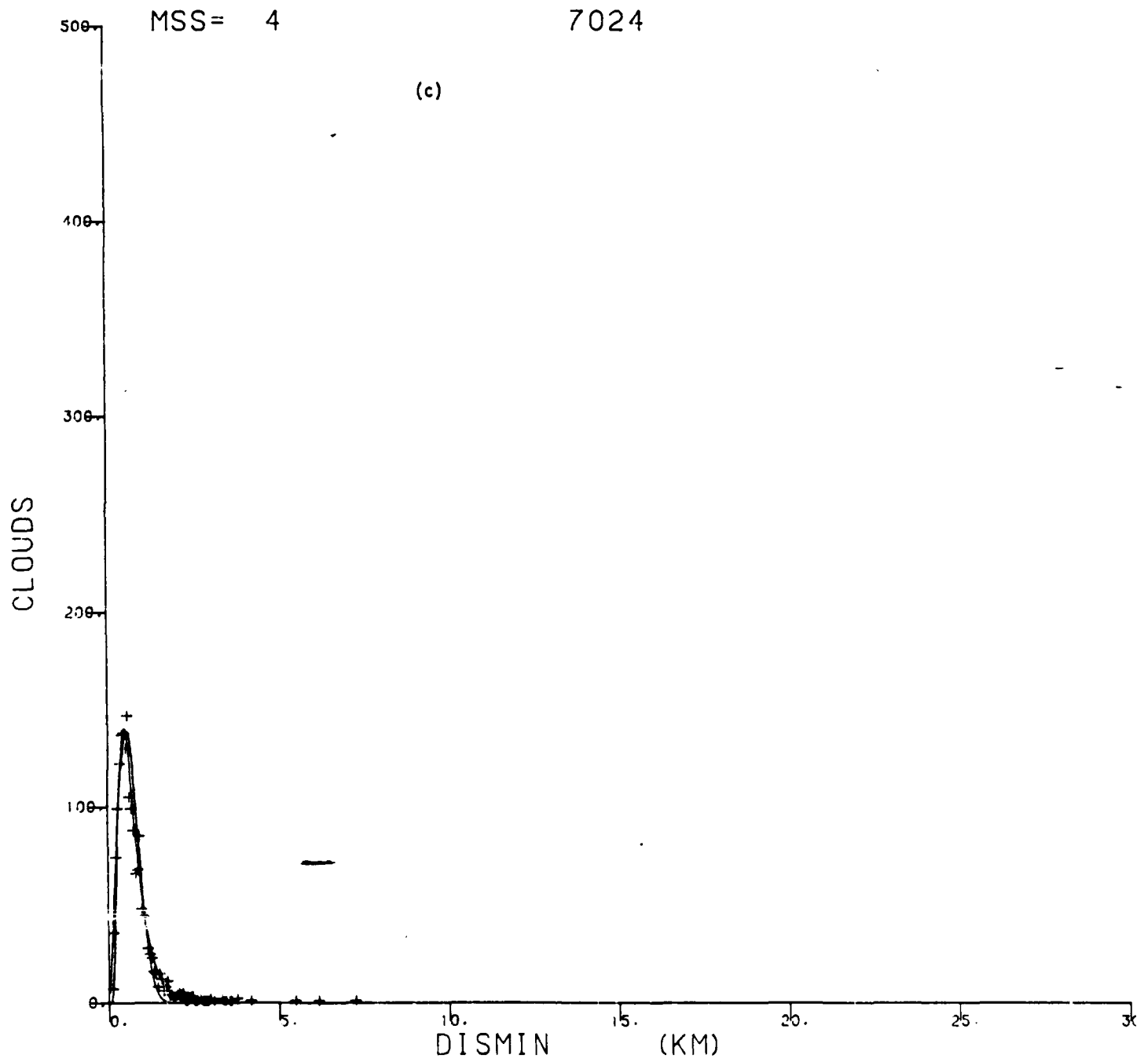


Table 3.1: Sources of Information on Clouds

Source	Spectral Ranges	Resolution	Temporal Coverage	Spatial Coverage
Ground-based Obs.	Solar and Terrestrial	5-100 m	All day year round	Local only
Balloon and Airplanes	Solar and Terrestrial	5-100 m	All day Sporadic	Regional Sporadic
MET SATS	Solar and Terrestrial	1-10 km	All day year round	Global
LANDSATS 2,3	Solar	70 m	Mid morning year round since 1972	Global
LANDSATS 4,5	Solar and Terrestrial	30 m 120 m	Mid morning year round since 1984	Global over land - special order - over ocean
SPOTSAT	Solar	10-20 m	Mid morning on demand only from 1985	Global on demand only

TABLE 3.2: The size distribution of Cumulus clouds over oceans

$$\frac{dN(r_e)}{dr_e} = K r_e^{-\beta} \quad \text{where } A \text{ is the area of cloud}$$

Location and Center Coordi.	Band	K	β	r_{max} (km)	No. of clouds	P(%) [*]	A(km ²) ^{**}
Ocean E. of Florida N23°04'W078°44'	MSS4	0.12	2.86	0.46	2521	32.9	8,036
	MSS7	0.11	2.87	0.46	2420	33.2	
Atlantic Ocean E. of Florida N24°30'W79°47'	MSS4	0.30	2.97	0.46	7329	13.5	17,172
	MSS7	0.31	2.96	0.46	7436	12.9	
Atlantic Ocean E. of Florida N24°30'W79°47'	MSS4	0.09	3.14	0.36	3349	17.5	17,235
	MSS7	0.10	3.13	0.36	3458	17.3	
Atlantic Ocean E. of Florida N24°30'W81°11'	MSS4	0.18	3.03	0.53	4738	19.0	15,200
	MSS7	0.18	3.02	0.43	4671	18.5	
Atlantic Ocean E. of Florida N24°28'W79°40'	MSS4	0.16	3.01	0.28	4235	8.8	16,243
	MSS7	0.19	2.92	0.28	4241	8.5	
Atlantic Ocean W. of Florida N28°46'W85°39'	MSS4	0.18	2.96	0.30	4450	1.4	31,491
	MSS7	0.24	2.77	0.30	3932	1.5	
Atlantic Ocean near Cape Verde Islands N17°16'W24°03'	MSS4	0.05	2.61	0.33	678	0.2	31,562
	MSS7	0.05	2.68	0.33	709	0.2	
Atlantic Ocean near Cape Verde Islands N15°50'W024°24'	MSS4	0.040	3.08	0.35	1274	0.9	13,681
	MSS7	0.045	2.99	0.35	1203	0.9	
Atlantic Ocean near Cape Verde Islands N14°24'W24°45'	MSS4	0.093	2.70	0.37	1477	0.6	31,568
	MSS7	0.083	2.75	0.36	1380	0.6	
Pacific Ocean NW of Marshall Islands N15°50'W173°20'	MSS4	0.45	2.64	1.0	7327	6.7	31,354
	MSS7	0.44	2.69	1.0	7548	6.7	
Pacific Ocean in Tuamotu Archipelago S15°51'W142°21'	MSS4	0.17	2.85	0.56	3616	14.5	31,721
	MSS7	0.17	2.82	0.56	3562	14.0	
Ocean near Okinawa N27°20'E129°07'	MSS4	0.83	2.33	1.2	6836	27.6	22,449
	MSS7	0.82	2.38	1.2	7013	26.5	
Ocean West of Israel N31°46'E34°11'	MSS4	0.16	2.58	0.5	1269	8.6	2,688
	MSS7	0.14	2.67	0.5	1242	7.4	
Plank 1969 (Fig. 7a)***	white light						
t=08-09		0.003	4.98	0.48	1645	6.0	256
t=09-10		0.15	2.57	0.64	1665	18.0	256
t=10-11		0.19	3.48	1.28	1056	26.0	256
t=11-12		0.22	4.19	1.20	1226	31.0	256
Hozumi 1982****	white light	2.68	2.15	0.8		0-10	
Pacific ocean		4.64	1.45	2.0		21-30	
Tokio to Taipei		3.16	0.91	2.0		41-50	

* P = Cloudiness in percent

** A = Total area analysed

*** Photographs from U2 aircraft

**** Photographs from commercial aircraft

TABLE 3.3: The distribution function of minimal distance between cloud pairs using a log-normal function

$$\frac{dN}{dD} = P_3 \exp \left\{ - (\ln D - P_1)^2 / 2P_2^2 \right\}$$

Location and center coordinates	MSS	P1	P2	P3
Okinawa	4	-0.478	0.566	272.748
N27°20'E129°07'	7	-0.452	0.556	280.887
Oc. of Israel	4	-0.560	0.491	64.771
N31°45'E34°11'	7	-0.559	0.510	61.156
Pacific ocean, NW of Marshall Islands	4	-0.635	0.529	353.155
N15°50'W179°20'	7	-0.639	0.522	370.676
Ocean East of Florida	4	-0.745	0.526	138.794
N23°04'W078°44'	7	-0.770	0.548	129.403
Atlantic Ocean near Cape Verde Islands	4	-0.829	0.604	57.498
N15°50'W24°24'	7	-0.843	0.590	54.712
Atlantic Ocean near Cape Verde Islands	4	-0.828	0.591	74.501
N14°24'W024°15'	7	-0.758	0.537	71.707

TABLE 3.4: Examples of fit to Weibull function

$$\frac{dN}{dD} = aD^n \exp \{-bD^{n+1}\}$$

of the distance D between nearest neighbours

Location and center coordinates		n	b	s
Ocean West of Israel N31°46'E34°11'	4	1.53	1.79	221.50
	7	1.40	1.60	187.69
Pacific Ocean near Okinawa N27°20'E129°07'	4	1.20	1.08	631.36
	7	1.22	1.07	652.90
Pacific Ocean near Marshall Islands N15°50'W179°20'	4	1.28	1.74	1078.34
	7	1.31	1.81	1167.22
Atlantic Ocean near Cape Verde Islands N15°50'W024°24'	4	0.83	1.72	142.116
	7	0.86	1.91	144.543
Atlantic ocean near Cape Verde Islands N14°24'W024°45'	4	1.01	1.95	217.382
	7	1.21	2.19	242.175

Chapter 4: On the fractal dimension of broken Cumulus cloud fields

4.1 INTRODUCTION

Clouds are important moderators of the Earth's radiation balance on both regional and global scale. They are also symptoms or diagnostic features in experimental and theoretical studies of both weather and climate thermohydrodynamics.

Many of the remote observations of the climate and weather system necessary for the implementation or validation of models or theories are strongly influenced by the presence of clouds.

Clouds are one of the facets of the problem of the parameterization of sub-resolution phenomena for weather prediction and climate modelling. Finally, the morphology of cloud fields is important for the planning and analysis of all remote sensing data of planetary atmospheres and surfaces (e.g. Lovejoy and Schertzer, 1986).

These are the main reasons for our undertaking an extensive and intensive analysis of clouds in high resolution LANDSAT satellite data. These will be in the future - augmented by SPOT, aircraft and other available high-resolution data on cloud field morphology.

Because of the fractal nature of cloud shapes, knowledge of the fractal dimension or dimensions of cloud fields is fundamental to the accurate description and parameterization of many cloud effects in applications varying from climate modelling to remote sensing.

AD-A174 944

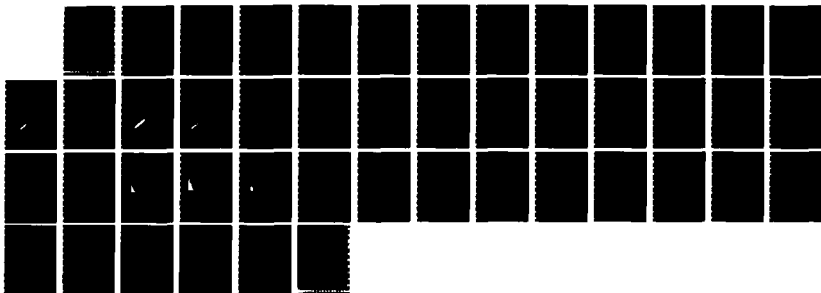
THE MORPHOLOGY OF BROKEN CLOUD FIELDS OVER OCEAN
SURFACES USING LANDSAT(U) TEL-AVIV UNIV (ISRAEL) DEPT
OF GEOPHYSICS AND PLANETARY SCIEN J H JOSEPH

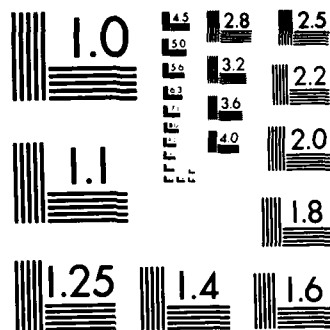
2/2

UNCLASSIFIED

05 MAY 86 AFOSR-TR-86-2126 AFOSR-84-0357 F/G 4/1

NL





MICROCOPY RESOLUTION TEST CHART
NATIONAL BUREAU OF STANDARDS-1963-A

4.2 DATA ANALYSIS

Determination of the fractal dimension involves the analysis of the area and perimeter of each discernible cloud.

The first problem is then the determination of a lower limit of brightness of a cloud pixel over a variable background. This difficult task is one of the reasons it was decided to analyse cloud data first over the ocean where cloud contrast is higher (Joseph and Cahalan, 1986, Joseph et al, 1986).

Many different techniques were tried based on one and two-dimensional histograms as well as other types of statistical analysis e.g. spatial coherence. The technique finally adopted is described elsewhere and based on comparison of size distributions, their moments and "noise" (clouds less than 4 pixels in area) on a man-computer interactive basis (Joseph and Cahalan, 1986, Joseph et al, 1986).

Secondly, there is the problem of determining the length of the perimeter of a cloud. This is especially important for clouds with "holes" and even more so for the smaller clouds.

We have carried out a study of three methods of calculating the cloud perimeter in the course of which one image has been analysed in great detail by our U.S. collaborator.

The main aim was a study of the effect of different choices of evaluations of the perimeter length on the value of the fractal dimension. Three main methods were used to calculate the perimeter - counting perimeter pixels, summing the length of all edges of pixels facing out from a cloud, and, thirdly, method two with an additional cutting of corners. All three methods give fairly

similar results for the slope of the $\log P$, $\log A$ curve for all but the smallest clouds (less than 12 pixels in area or $r_e < 0.1$ km. In the case of the latter, the first two again give similar results. The last method depends on correcting not only the perimeter but the area as well and also on proper filtration of the very smallest clouds - those less than 4 pixels in area.

We adopted the first method in our study but did not take into account clouds of area of three pixels and less as these are within the noise level of the data.

Thirdly, there is the question of taking into account the fact that some pixels may be only partially cloud-filled. This is particularly important for the small clouds. It is also connected to the first problem mentioned in this section, namely the identification of the cut between cloud and background intensities. After trying several approaches (e.g. Joseph et al, 1986) we feel that further reducing the number of cloud pixels already identified by the cut, by applying some assumption on the perimeter pixels - e.g. fifty percent cloud cover - is artificial and redundant. Moreover, as shown in the previous chapter, the derived properties are not sensitive to changes in the location of the cut of the order of one or two grey levels. Therefore any pixel identified as a cloud pixel by our iterative analysis was counted as part of the area or perimeter of a cloud.

4.3 THE FRACTAL DIMENSION OF CLOUD PERIMETERS

We have put particular emphasis in this paper on the relationship between areas, A , and parameters, P , of clouds. A previous study on such properties of clouds fields (Lovejoy, 1982) showed-through the existence of a constant slope of $(\log P - \log A)$ curves in a range of effective cloud radius ($r_e = (A/\pi)^{1/2}$) between 1 and 1000 km the validity of a power law, connecting the area and the perimeter in the above range of sizes. A second, very recent study showed the existence of two slope regimes (Rys and Waldvogel 1986).

One possible meaning of these results has been discussed in the literature (Mandelbrot, 1982) in terms of the fractal dimension of the 3-D cloud field and of that of a 2-D cut through the latter - e.g. a satellite image of a cloud field - the slopes of spectra of atmospheric turbulence and scales of motions may be indicated (ibid 1982).

The use of fractal dimensions to describe the geometry of continuous but non-differentiable curves and surfaces has been recently introduced (e.g. Mandelbrot, 1982). Clouds are such self-similar "scaling fractals" e.g. objects with no intrinsic scale, having a perimeter which depends only on the resolution and the "fractal dimension" of the object. Empirically, in our case this means that a satellite image of a cloud field, taken over a uniform dark ocean background with no evident geographical features, would be statistically indistinguishable from an image of any small portion of the scene if it had the same number of pixels as the original.

Physically, it may mean that there exist no preferred scales of motion in the size range where the relationship applies. This may have important consequences for several theoretical and applied fields of research in the atmospheric sciences.

Lovejoy's data are shown in Figure 4.1. This is a log-log plot of the area versus the perimeter of rain and cloud areas determined by a threshold technique from radar and satellite data. The lower solid line is a least-squares fit implying a power law of the form

$$\text{area} \sim (\text{perimeter})^{2/d}$$

where d is the "fractal dimension" given of the perimeter, $d = 1.35$. If cloud perimeters were smooth curves (i.e. one-dimensional) then they would enclose an area proportional to the square of the perimeter, so that the slope would have been 2. This case is shown here for comparison as the upper solid line labelled $d = 1$.

Note that a synoptic-scale system would lie at the upper extreme of this plot. A cloud covering one kilometer in diameter, the limit of resolution of present meteorological satellites, would be at the lower extreme. Over the extensive sub-tropical high pressure systems of the central oceans and also elsewhere one finds persistent fields of cumulus clouds most of which have a

diameter well below one kilometer. Such sub-resolution cloud fields (for meteorological satellites) contribute, inter alia, to errors in satellite-based estimates of cloud cover and sea-surface temperature. The idea that clouds are scaling fractals suggests that effects of the smaller scales on area-averaged quantities could be estimated from the large-scale data themselves. However, we shall see that the process of convection and the existence of a planetary boundary layer introduce a second fractal dimension which only becomes evident at the higher resolution available from Landsat.

Figures 4.2 (a), (b), (c) and (d) show a set of ($\log P$, $\log A$) diagrams in the blue spectral band (MSS4). The other band analysed exhibits identical results and is therefore not shown here. All results in both bands are available in the Appendices.

The cloudiness of the images analysed in the figures varies from 1.4 to 32 percent, which is about the range of our data. Most of the clouds are small, much below 1 km in effective radius. This is normal for the fair weather cumulus type of cloud field, as shown in a previous paper (Joseph and Cahalan 1986). The numbers and letters show the frequency of occurrence of clouds at each experimental point. The number of clouds involved is very large and given in Table 4.1 and in the Appendices for all images analysed.

The line with the smaller slope shows the linear least square fit to all data, which emphasizes the clouds below 1 km in size.

It is obvious that for clouds larger than a certain effective radius, this fit does not give the correct slope anymore. Using the deviation of the experimental points from the fit to all data, we determine statistically the most likely point for the change in slope. The line with the larger slope shows the best fit to the

experimental data above the latter point. It is obvious that a statistically significant increase in slope-fractal dimension occurs. This result has been corroborated recently in the literature (Rys and Waldvogel, 1986).

All the results described above are shown in Table 4.1 for thirteen locations, scattered over the globe. The fractal dimension of the cloud field is shown, as derived from experimental $(\log P - \log r_e)$ curves - like Figure 4.1 and from the slope of the size distributions, β (Joseph and Cahalan, 1986).

The fractal dimension for all clouds (fourth column) and for the large clouds ($r_e \geq r_{\text{break}}$) (sixth column) is shown for a variety of locations. The average value for all clouds taken together is 1.29 with a standard deviation of 0.3. The present results for the clouds with an effective radius larger than r_{break} , about 0.5 km, show a fractal dimension averaging 1.51 ± 0.12 . The value of 1.37, close to Lovejoy's value, was found in one case only. The break radius, determined by an analysis of the deviation of the residuals of the fit from a normal distribution, is shown in the fifth column in km and marked "Break".

The location of the break in slope - or fractal dimension - is on the average at 0.5 km and spreads from 0.178 to 1.0 km.

In column seven, we show the fractal dimension of the perimeter as calculated from the slope, β of the distribution of cloud radii (Mandelbrot 1984).

$$D = \beta - 1$$

The slope is determined from all clouds less than a maximal radius, r_{\max} , which is shown in column 8. The latter radius is defined as the last point that fits the slope determined from the majority of clouds. The tail of the distribution contains a relatively small number of large clouds, which, though not important for the statistics, may contribute significantly to the total cloudiness. This maximal radius is of the order of 0.5 km, or a single cloud area of about 0.8 km^2 . For more details on the analysis, see the other chapters. The ratio of the fractal dimension derived in the latter way, $D = \beta - 1$, to that from the $(\log P - \log r_e)$ curves is always larger than one. There is no apparent relationship between D and the quantity $\beta - 1$, which averages at $\beta - 1 = 1.79 \pm 0.22$.

4.4 DISCUSSION

Lovejoy (1982) reached several conclusions in his pioneering recent paper. The first is that clouds are self-scaling fractal entities with a fractal dimension of $4/3$ of the perimeter. Secondly, that clouds are fractals down to the lowest resolvable scale in the atmosphere and that therefore there are no dominant scales in the atmosphere, except for the radius of the Earth. Thirdly, that, because cloud outlines (or perimeters) and their movements may be assumed to be equivalent to those of turbulent isobars, there exists a fairly straightforward physical connection between homogeneous isotropic turbulence in three dimensions, described by the wellknown $5/3$ power law for the energy scale spectrum and the processes that produce clouds and rain.

The latter result was theoretically explained by an improvement in the theory of 3D turbulent diffusion in the atmosphere (Hentschel and Procaccia 1984).

The first and second of these conclusions may be somewhat doubtful because of our results. The fractal dimensions that we find are only rarely close to $4/3$ and are usually significantly smaller for the clouds less than about 0.5 km in effective radius. Secondly, we find that there occurs a distinct break in the slope of the $(\log P - \log A)$ relation at all the geographic locations we have investigated. This break is at an effective cloud radius of about 0.5 km and varies between 0.2 and 1.0 km and is corroborated in the literature (Rys and Waldvogel 1986).

Caution is indicated in reaching these conclusions because of the possible effect of holes on the perimeter-area relationships. This effect of the holes should be larger for the smaller clouds and might thus lead to the spurious occurrence of a break in the slope and to a smaller slope for the small clouds.

Therefore an analysis of the occurrence and size distribution of holes in clouds was carried out.

The holes typically have an effective radius distribution with a negative slope larger than 3 and range between a minimum effective radius of 44 meters to about 450 meters.

The negative slope of the size distribution of the holes is thus larger than that of the clouds encircling them, leading to rapid decrease in the possible influence of holes with increasing cloud size.

Furthermore, the location of the break is always much over our resolution. All the results presented in this paper take into account the presence of holes in the determination of the perimeter-area relationships (See Chapter 2). We are therefore fairly confident that the break (or possibly a functional dependence of the fractal dimension on r_e) is in fact real and should be taken into account.

Fair weather ⁻cumulus clouds usually have aspect ratios of the order of one (e.g. Plank 1969), therefore the thicknesses of the clouds average 1 km and vary between 0.4 and 2 km. This is about the depth of the typical atmospheric boundary layer that supports the cloud formation.

The effective cloud diameter at which the change in the value of D , the slope of the $(\log P - \log A)$ curve, occurs, is at about the same size with the same range.

It may thus be that this scale - that of the thickness of the boundary layer - is the most important scale of energy input into the atmosphere and that the change in slope is due to a change over from 3D turbulence in the planetary boundary layer to 2-D turbulence in the free atmosphere (e.g. Lovejoy, 1986).

The differences between the values of the fractal dimension D above and below the break in each case are statistically significant. The idea of clouds being simple self-similar scaling fractals down to the smallest size is thus not acceptable without modification. Therefore, for instance, it is not directly possible to use the fractal dimension of an observed large scale, low-resolution cloud field from a meteorological satellite in order to correct for the effect of sub-resolution cloudiness on the determination of sea surface temperature or of surface albedo. On the other hand, climatological data on the variation of fractal dimensions with ⁻cloud size or type may make the above practical applications possible.

4.5 SUMMARY

We have presented some of the results of an extensive ongoing analysis of LANDSAT imagery containing broken cumulus cloud fields over the ocean. The present results are based on a multispectral analysis of 17 locations.

It was shown that two regimes exist, each with its own fractal dimension. All Cumulus clouds less than about 500 meters in effective radius in a cloud field seem to display a fractal dimension of 1.29 ± 0.03 , those larger than 500 meters in radius - a fractal dimension of 1.51 ± 0.12 .

These results may have important implications for both modelling and remote sensing applications.

If cloud fields in fact are bi-fractal in nature, it may mean that between the global and micro scales of atmospheric turbulent thermohydrodynamics, there exists a scale of the order of the atmospheric planetary boundary layer at which energy is fed into the larger scales from the planetary surface. This may have important applications to the modelling of climate.

In addition, if this result turns out to be universally true, it may be possible to correct low-resolution remote sensing data for the effect of sub-resolution clouds, using climatologically determined relationships between the fractal dimensions of large and smaller scale clouds.

Future work will enlarge the set of locations studied over both ocean and land, as well as add the analysis of ultra-high resolution data at different times of day.

4.6 Acknowledgements

This study was funded in part by US AFOSR Grant 83-0239 and the US- Israel Bi-National Science Foundation Grant 30892/82. One of us (J.H.J) wishes to acknowledge short period subsistence support in the US by NASA and the University of Maryland, which contributed to the efficient planning and execution of this study.

Both authors wish to thank the very significant contributions in scientific programming and analysis of Mrs.S. Rechavi, Mrs. Z. Rosen, Mrs. S. Adler and of Dr. J. Robinson.

4.7 References

- Joseph, J.H. and R.F. Cahalan, 1986: On the size distribution of Fair Weather Cumulus Clouds. Journ. Atmos. Sci.
- Joseph, J.H., R.F. Cahalan, S. Rechavi, Z. Rosen and S. Adler, 1986: The analysis of cloud field morphology using LANDSAT images.
- Lovejoy, S., 1982: The area-perimeter relationship for rain and cloud areas. Science, 216, 185-187.
- Lovejoy, S. and D. Schertzer, 1986: Scale invariance, fractals and stochastic simulations of atmospheric phenomena. Bull. Am. Met. Soc., 67, 21-32.
- Mandelbrot, B., 1984: The fractal geometry of Nature. Freeman & Co., New York, 461.
- Plank, G.W., 1969: The size distribution of Cumulus clouds in representative Florida populations. J. Atm. Sci. 31, 1571-1576.
- Rys, F.S. and A. Waldvogel, 1986: Fractal shape of hail clouds. Phys. Rev. Lett. 56, 784-787.
- Hentschel, H.Q.E. -and I. Procaccia, 1984: Relative diffusion in Turbulent media, the fractal dimension of clouds. Phys. Rev. A29, 1461-1476.

Figure 4.1: The fractal dimension of very large cloud perimeters (Lovejoy 1982).

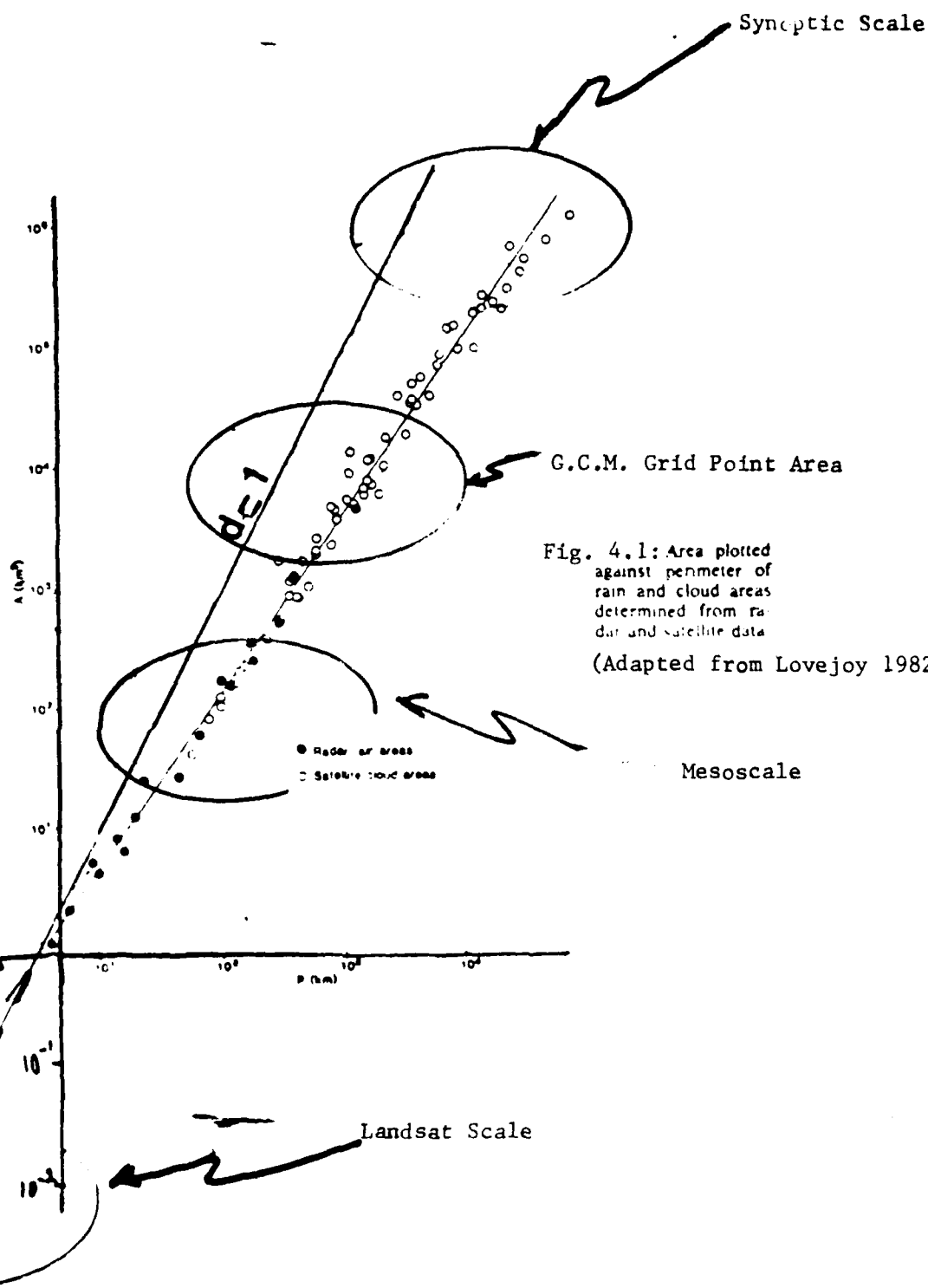
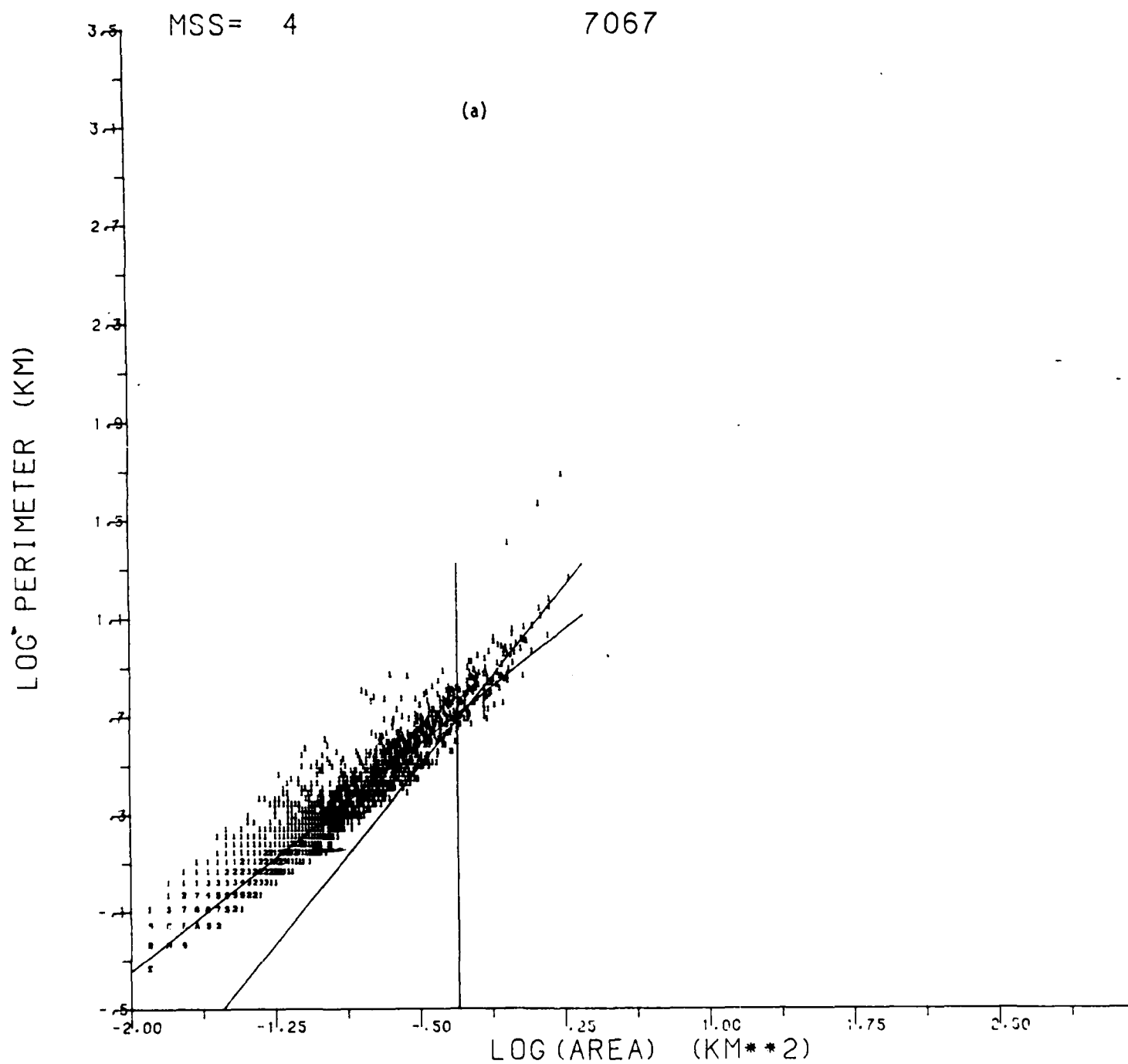


Fig. 4.1: Area plotted against perimeter of rain and cloud areas determined from radar and satellite data (Adapted from Lovejoy 1982)

Figure 4.2: A range of examples of the relationship between cloud perimeters and areas for four locations.



I 68

AJKM

I 68

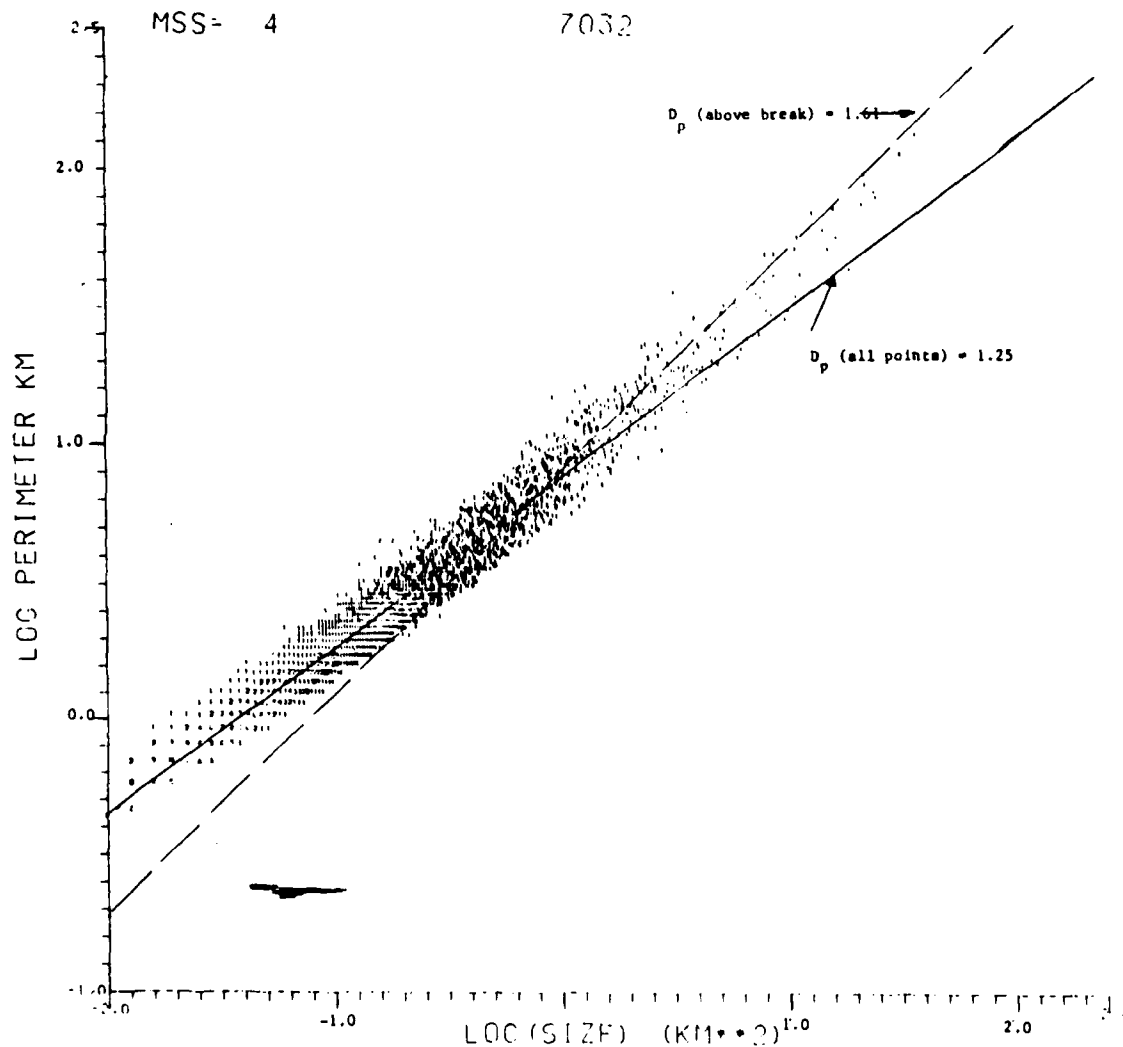
AJKM

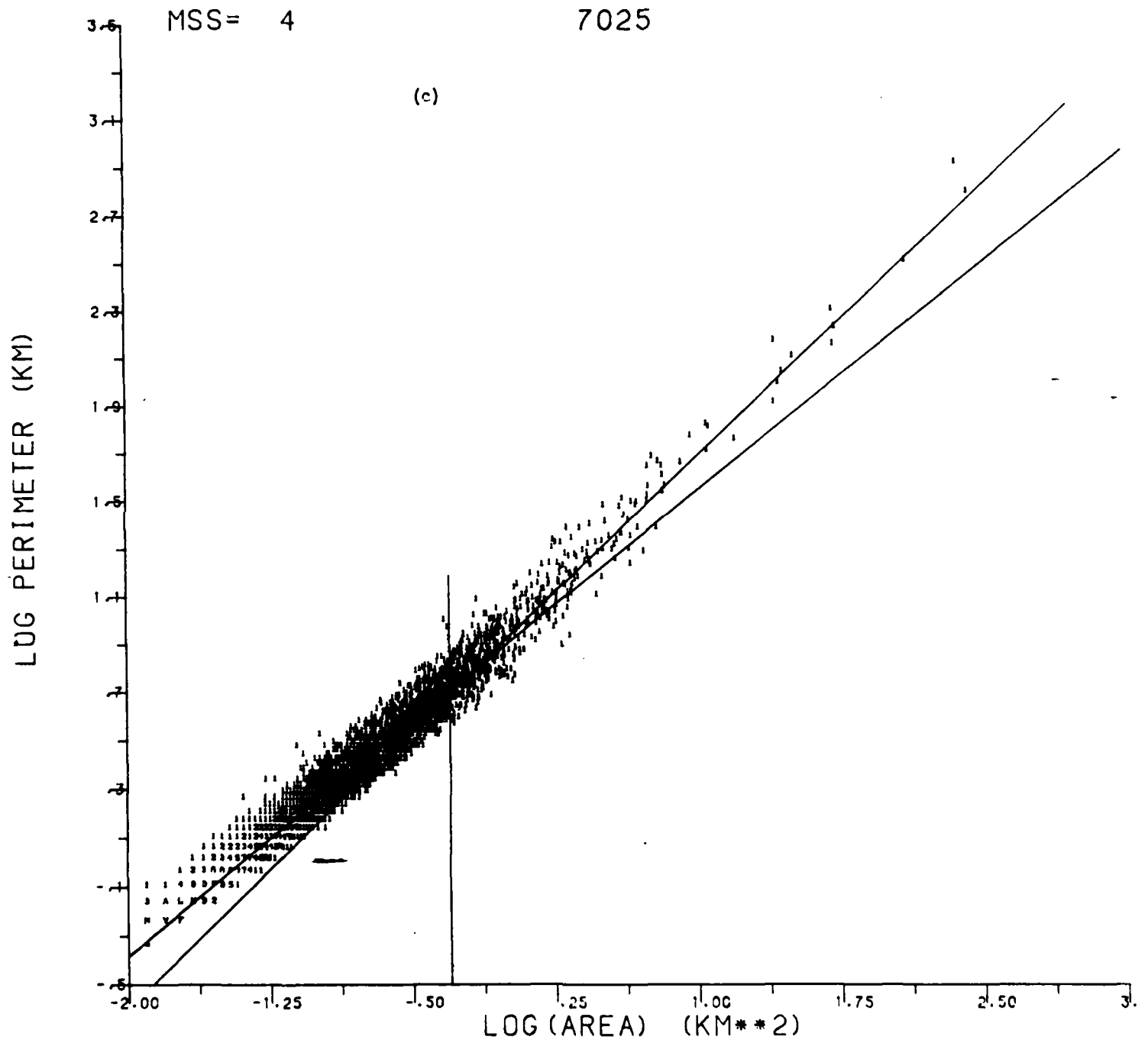
Figure 4.2b:

A TYPICAL EXAMPLE OF THE RELATIONSHIP BETWEEN CLOUD PERIMETERS AND AREAS FOR A LOCATION IN THE PACIFIC OCEAN NEAR THE MARSHALL ISLANDS - $N15^{\circ}50'W179^{\circ}25'$ (OUR ID # 7032). THE BREAK IN SLOPE OCCURS FOR A CLOUD EFFECTIVE RADIUS OF 0.564 KM, WHERE THE SLOPE CHANGES FROM $D_p = 1.25$ TO $D_p = 1.61$. CLOUDINESS IS 6.7%.

P (ALL POINTS) = $7.630 A^{0.627}$

P (ABOVE BREAK) = $7.716 A^{0.805}$





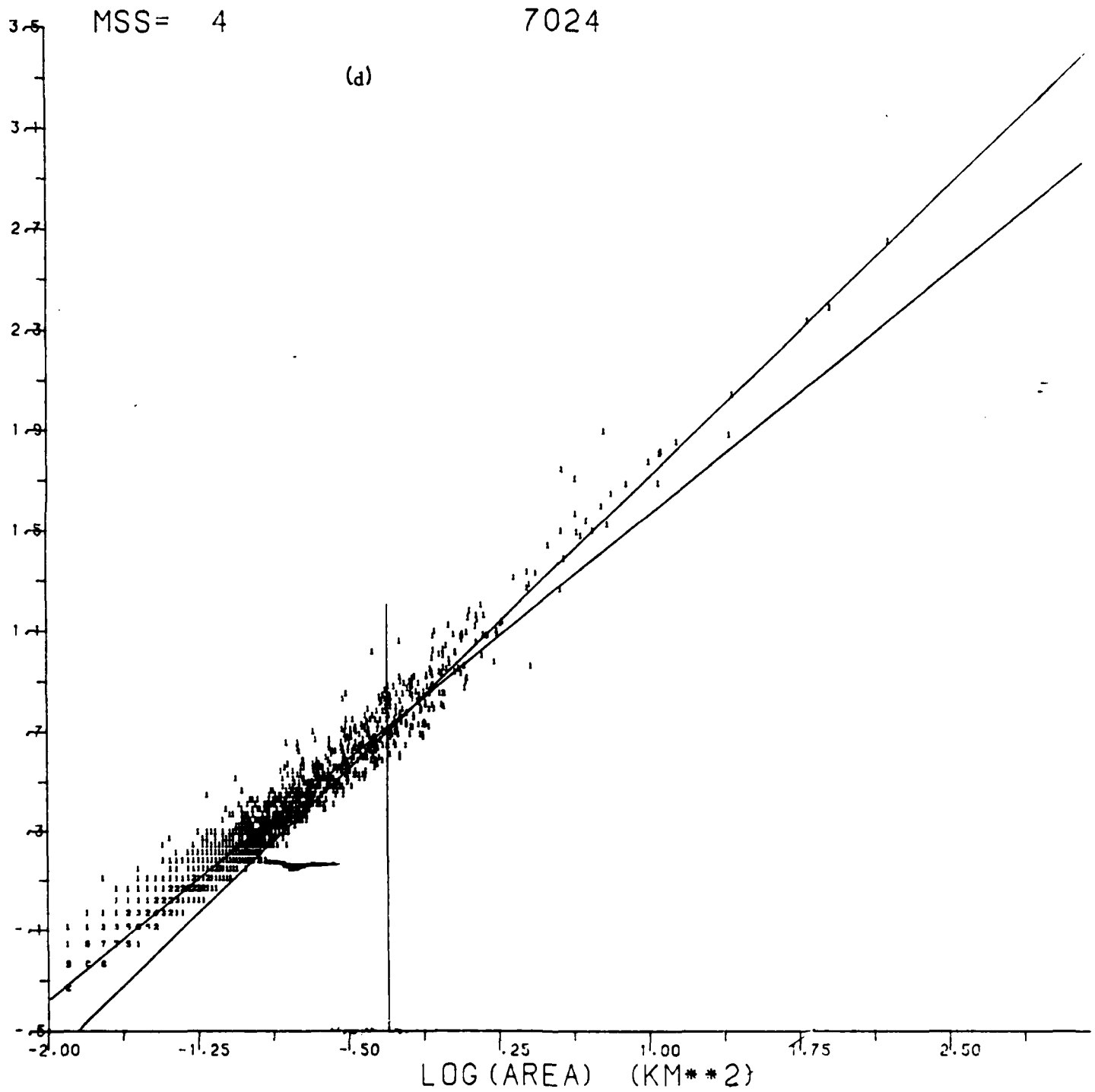


TABLE 4.1: Summary of Data on Fractal Dimension, D_p (Average of MSS-4 and MSS-7)
(See also Appendix III)

Image Number	Location	Center Coordinates	D_p calculated from (P_1A) curves		D_p calculated from $P_{DN}/dr = K \frac{-\beta}{r}$	
			all clouds	break (km)	large clouds only	$\beta-1$ r_{max} (km)
7024	Ocean W. of Florida	N23°04' W078°44'	1.35	0.5	1.54	1.51 0.46
7025	Straits Florida	N24°30' W079°47'	1.30	0.5	1.53	1.97 0.46
7028	Straits Florida	N24°30' W079°47'	1.30	0.5	1.51	2.13 0.36
7026	Straits Florida	N24°30' W081°11'	1.28	0.5	1.47	2.02 0.53
7029	Straits Florida	N24°28' W079°40'	1.32	0.5	1.62	1.97 0.28
7067	Gulf Mexico	N28°46' W085°39'	1.26	0.5	1.72	1.86 0.30
7036	Cape Verde Islands	N17°16' W024°03'	1.24	0.5	1.65	1.64 0.33
7035	Cape Verde Islands	N15°50' W024°24'	1.28	0.7	1.51	2.00 0.35
7034	Cape Verde Islands	N14°24' W024°45'	1.25	0.95	1.56	1.73 0.37
7032	Marshall Islands	N15°50' W0179°20'	1.26	1.0	1.27	1.66 0.5
7033	Tuamotu Archipelago	S15°51' W142°21'	1.27	0.5	1.41	1.83 0.56
7030	Okinawa	N27°20' E129°07'	1.32	0.448	1.49	1.36 1.2
7013	Ocean W. of Israel	N31°46' E034°11'	1.29	0.178	1.37	1.62 0.5

Chapter 5: Application to Cumulus Cloud Convection

5.1 The mean mass flux at cloud bottom altitude

An important application of our present data to atmospheric physics is an attempt to estimate the mean mass flux at cloud bottom altitude. We assume that the clouds in a fair weather broken cumulus field are non-interacting transient, growing and decaying, convective plumes with a power-law size distribution.

$$\frac{dN(r)}{dr} = Kr^{-\beta}$$

and cloud mass flux $m(r)$, both independent of altitude. Cloud sizes are bounded between a minimum effective radius, r_{\min} , and maximum radius, r_{\max} .

Under these circumstances, the mass flux per unit area of the cloud field at cloud bottom altitude is given by

$$m(r) = \int_r^{r_{\max}} dr' \frac{dN(r')}{dr} m(r') / F_0 \quad (1a)$$

where

$$m(r) = \frac{C_1}{3\alpha} r$$

$$C_1 = 1 \times 10^5 \text{ kg m}^{-1} \text{ s}^{-1} \text{ disturbed conditions}$$

$$3\alpha = 0.75$$

and F_0 is the magnitude of the area investigated. This analysis follows a model presented in the literature (Fraedrich, 1976, 1977.)

Integration results in:

$$M(r) = \frac{K}{\beta-2} \frac{C_1}{3\alpha} (r^{2-\beta} - r_{\max}^{2-\beta}) / F_o \quad (1b)$$

The area A, and accumulated number N of clouds can be similarly expressed

$$A(r) = \frac{\pi K}{3-\beta} (r_{\max}^{3-\beta} - r^{3-\beta}) \quad (2a)$$

$$N(r) = \frac{K}{1-\beta} (r_{\max}^{1-\beta} - r^{1-\beta}) \quad (2b)$$

All three accumulated quantities can be expressed by a constant and a profile function in the following manner.

$$M(r) = M_o m^*(r) \quad (3a)$$

$$N(r) = N_o n^*(r) \quad (3b)$$

$$A(r) = A_o a^*(r) \quad (3c)$$

where

$$M_o = \frac{K}{\beta-2} \frac{C_1}{3\alpha} (r_{\min}^{2-\beta} - r_{\max}^{2-\beta}) / F_o \quad (3d)$$

$$m^*(r) = (r^{2-\beta} - r_{\max}^{2-\beta}) / (r_{\min}^{2-\beta} - r_{\max}^{2-\beta}) \quad (3e)$$

$$N_o = \frac{K}{\beta-1} (r_{\min}^{1-\beta} - r_{\max}^{1-\beta}) \quad (3f)$$

$$n^*(r) = (r_{\min}^{1-\beta} - r^{1-\beta}) / (r_{\min}^{1-\beta} - r_{\max}^{1-\beta}) \quad (3g)$$

$$A_o = \frac{\pi K}{3-\beta} (r_{\max}^{3-\beta} - r_{\min}^{3-\beta}) \quad (3h)$$

$$a^*(r) = (r_{\max}^{3-\beta} - r^{3-\beta}) / (r_{\max}^{3-\beta} - r_{\min}^{3-\beta}) \quad (3i)$$

and M_o , N_o and A_o are the values of $M(r)$, $N(r)$ and $A(r)$ at $r = r_{\min}$.

The mean mass flux, M_o , can be expressed in terms of the observed quantities N_o , A_o , β , r_{\min} , r_{\max} and F_o , namely

$$M_o = \frac{C_1}{3\alpha} \frac{1}{F_o} \frac{(\beta-1)^{\frac{1}{2}} (3-\beta)^{\frac{1}{2}}}{\beta-2} \frac{r_{\min}^{2-\beta} - r_{\max}^{2-\beta}}{(r_{\min}^{1-\beta} - r_{\max}^{1-\beta})^{\frac{1}{2}} (r_{\max}^{3-\beta} - r_{\min}^{3-\beta})^{\frac{1}{2}}} \frac{A_o^{\frac{1}{2}} N_o^{\frac{1}{2}}}{\pi} \quad (4)$$

The units of K are $\text{km}^{(1-\beta)^{-1}}$, r_{\min} and r_{\max} are in km , F_o in km^2

and M_o in $\text{kg m}^{-2} \text{s}^{-1}$ is then divided by 10 to get the values shown in

Table 5.1, which are given in terms of increasing percentage of cloudiness and compared with three representative values taken from the literature.

The results are also shown in Fig.5.1 which shows the mean mass flux at cloud bottom as a function of cloudiness in percent. A least square linear fit was made between the computed mean mass flux and the percentage of cloudiness. The correlation and fits are fairly good considering the fact that our data are basically "snapshots" derived from seventeen different locations at different seasons at different mid-morning times and under different synoptic conditions.

The numerical regression equation is

$$M_o = 0.59 + 0.049 * P \quad (5)$$

where M_o is in $10^{-2} \text{ kg m}^{-2} \text{ s}^{-1}$, P is in percent and the correlation coefficient is 0.78.

The mean mass flux thus seems to be linearly proportional to cloudiness as follows from our equations (3d) and (3h) as well as from experimental data.

As already mentioned above, our computed fluxes represent an application of a particular transient plume theory of convection to our size distribution data, assuming conditions to be disturbed, $C_1 = 1 \times 10^5 \text{ kg m}^{-1} \text{ s}^{-1}$ (Fraedrich 1976, 1977). The size distribution data are collected from many different locations and seasons at mid-morning times. The slightly low correlation of the fit (0.78) is therefore to be expected. At all locations the presence of clouds probably represents fair to disturbed weather conditions.

The GATE A/B results (Houze and Cheng 1981) also represent convective conditions, but averaged over the whole GATE area for A/B conditions which include Fair Weather Cumulus as well as more highly convective situations.

The fact that the GATE A/B area fluxes are slightly higher than ours for the same average amount of cloudiness is therefore understandable.

Fraedrich's data for 50% cloudiness are slightly lower than our prediction for such cloudiness. Again this is understandable as they represent ATEX undisturbed conditions only.

Although the agreement of the fluxes computed from our data appear fairly well to the in-situ results, our results should be only taken as an indication that further studies are strongly indicated.

It should be mentioned in this context that one of the conclusions from the GATE experiment is the importance of the few large cloud areas for rainfall and cloudiness. This may indicate that one needs to deal with multimodal size distributions.

If one assumes that the mass fluxes of individual non-interacting clouds do not vary with height, one can calculate the change with height of the average mass flux of the bottom of the clouds directly from the profile function (3e). ~~The~~ type of clouds we have analyzed have aspect ratios - diameter to thickness ratios - of the order of one (Plank 1969). Therefore, we can transform the dependence on r to a dependence on height h above the common cloud bottom, by using that fact, e.g.

$$\frac{2r}{h} = 1 \quad (6)$$

The mass flux then decreases approximately as the ratio of the total cloud area at height $h = 2r$ to that at cloud bottom,

$$\frac{M(h)}{M(o)} = \frac{r_{\max}^{(3-\beta)} - (h/2)^{(3-\beta)}}{r_{\max}^{(3-\beta)} - r_{\min}^{(3-\beta)}} \quad (7)$$

The function peaks at the bottom of the cloud layer, and its decrease to zero above that height depends on β and r_{\max} .

The larger r_{\max} is, the slower will the profile function decrease with height. The dependence on β is weaker, as the latter varies in our data between 2.3 and 3.5. The importance of taking into account all clouds is thus clear. However, our size distribution combined with the sample parameterization model for the flux cannot reproduce the maximum in the profile at about 450 mb in the GATE A/B data, which is probably due to meso-scale phenomena, not taken into account in the model used by us (Houze and Cheng 1981). The rapid decay of $M_o(h)$ with height above cloud base shown by Fraedrich (Fraedrich 1977) is reproduced approximately.

5.2 The ratio of updraft to downdraft in convective Cu clouds

Another application of our data to the convection problem is an estimate of the ratio of average updraft speeds to average downdraft speeds. If one assumes that each active cumulus cloud is isolated from all others and that mass is conserved, then, from mass continuity, we must have a definite ratio between the area of the updraft and that of the downdraft for a given cloud. We

tried to approximate that ratio in the following way, assuming the total area of each visible cloud to represent an updraft.

We calculated for each cloud of given radius r , the nearest distance, D , from those neighbours whose areas are at least one tenth greater. The latter condition was decided upon in order not to calculate trivial distances between a cloud and a small puff close by that may be part of it. We then plot the ratio $r^2/((D/2)^2 - r^2)$ which we term γ . The latter ratio should be an approximation to the ratio of cloud area to clear area around it that is part of the same convection cell. Only one half of the nearest distance was taken for the same reason.

Typical results are shown in Figures 5.2(a), (b) and (c). These are two-dimensional plots of the ratio γ versus the effective radius r_e . Because of the very large number of clouds involved in each case - of the order of thousands - the points run together and form a pattern, similar for all cases analysed. This pattern has the following properties. First, the great majority of points cluster in the upper right (positive) quadrant of the (γ, r_e) plane in the vicinity of the origin. There are no negative values of γ , except the rare cases when two elongated clouds are very close together.

This result indicates that the mode or preferred value of γ is very small and positive. Secondly, on analysis of the figures, it becomes clear that this mode value is independent of the effective cloud radius.

In order to study these results in some more detail, we show in Tables 5.2(a) and 5.2(b) the same data for both bands (MSS4 and MSS7) of Case 7072.

Because of the large number of clouds involved, 11,300, spanning a range of areas, A , from 0.002 to 20 km², the effective radii

$$r_e = (A/\pi)^{1/2} \quad (8)$$

where divided into groups of equal size intervals when there are many clouds and the last 10 clouds in one final interval. In this way the few large clouds can still show their own behaviour w.r.t. those smaller.

The number of cases in each radius range is thus not equal. However, due to the large number of clouds involved in each range, except for the largest clouds, this is not a serious problem. We find that in the cases considered, the ratio

$$r^2 / ((D/2)^2 - r^2)$$

again shows the two above properties, which are typical of all cases analysed.

First, the peak value of the histogram of the ratio in each size range is between 0 and 0.025. The majority of ratios are in this range as shown in Tables 5.2.a and 5.2.b.

Secondly, the peak value is almost independent of cloud size up to and including the largest clouds.

It seems to us that the properties indicated by this result are that the clouds are formed in isolated cells in a region of fairly homogeneous horizontal distribution of water vapor content. Turbulent convergence of water vapor flux led to the formation of a cloud in each cell concentrating the water of the latter into the visible cloud volume. The area or volume of each turbulent cell determines the amount of available water vapor and thus the size of the cloud. The ratio of water vapor source region to cloud region for each cloud should be constant and lead to our result.

The range of values found by us may be compared to a theoretical estimate of the ratio of a cloud radius to its "radius of influence". The above ratio may be approximated by $r(D/2)$ and using our data gives a range of

$$0 < r/(D/2) < 0.16$$

as compared to the theoretical value of about 0.2 for amounts of cloudiness between 5 and 15 percent (Soong and Ogura 1973, Cho 1978).

5.3 References

- Cheng, C. -P. and R.A. Houze, Jr. 1980: Sensitivity of diagnosed convective fluxes to model assumptions. J. Atmos. Sci., 37, 774-783.
- Cho, H.R., 1978: Some statistical properties of a homogenous and stationary shallow Cumulus cloud field. J. Atmos. Sci., 35, 125-138.
- Fraedrich, K., 1976: A mass budget of an ensemble of transient Cumulus clouds determined from direct cloud observations. J. Atmos. Sci., 33, 262-268.
- Fraedrich, K., 1977: Further studies on a transient Cumulus cloud ensemble and its large scale interaction J. Atmos. Sci., 34, 335-343.
- Houze, R.A. and C. -P. Cheng, 1981: Inclusion of mesoscale updrafts and downdrafts in computations of vertical fluxes by ensembles of tropical clouds. J. Atmos. Sci., 38, 1751-1770.
- Plank, G.W., 1969: The size distribution of Cumulus clouds in representative Florida populations. J. Atmos. Sci., 31, 1571-1576.
- Soong, S.T. and Y. Ogura, 1973: A comparison between axisymmetric and slabsymmetric Cumulus cloud models. J. Atmos. Sci., 30, 879-893.

Figure 5.1: - The dependence of the mean mass flux at cloud bottom as a function of cloudiness in percent

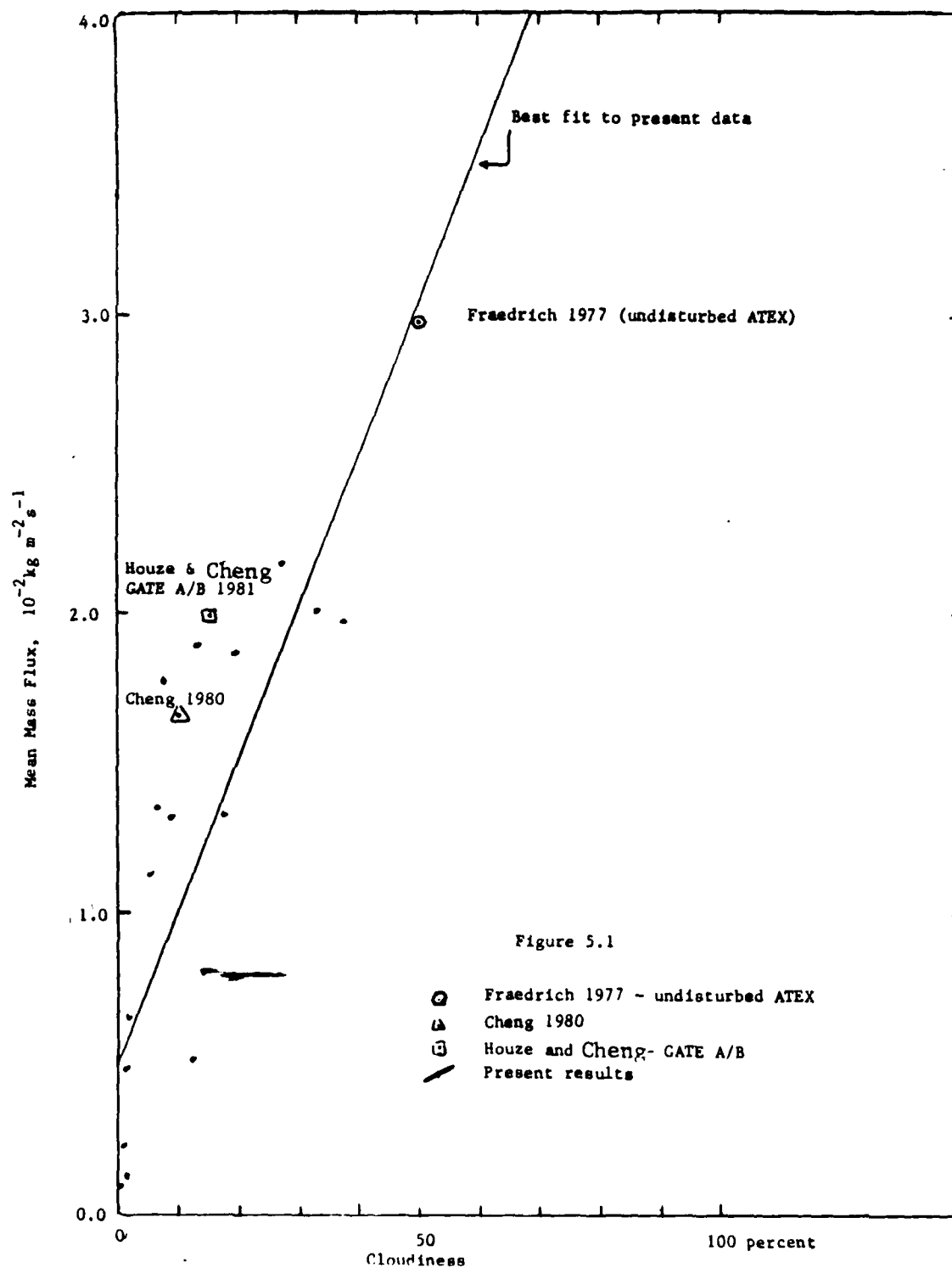
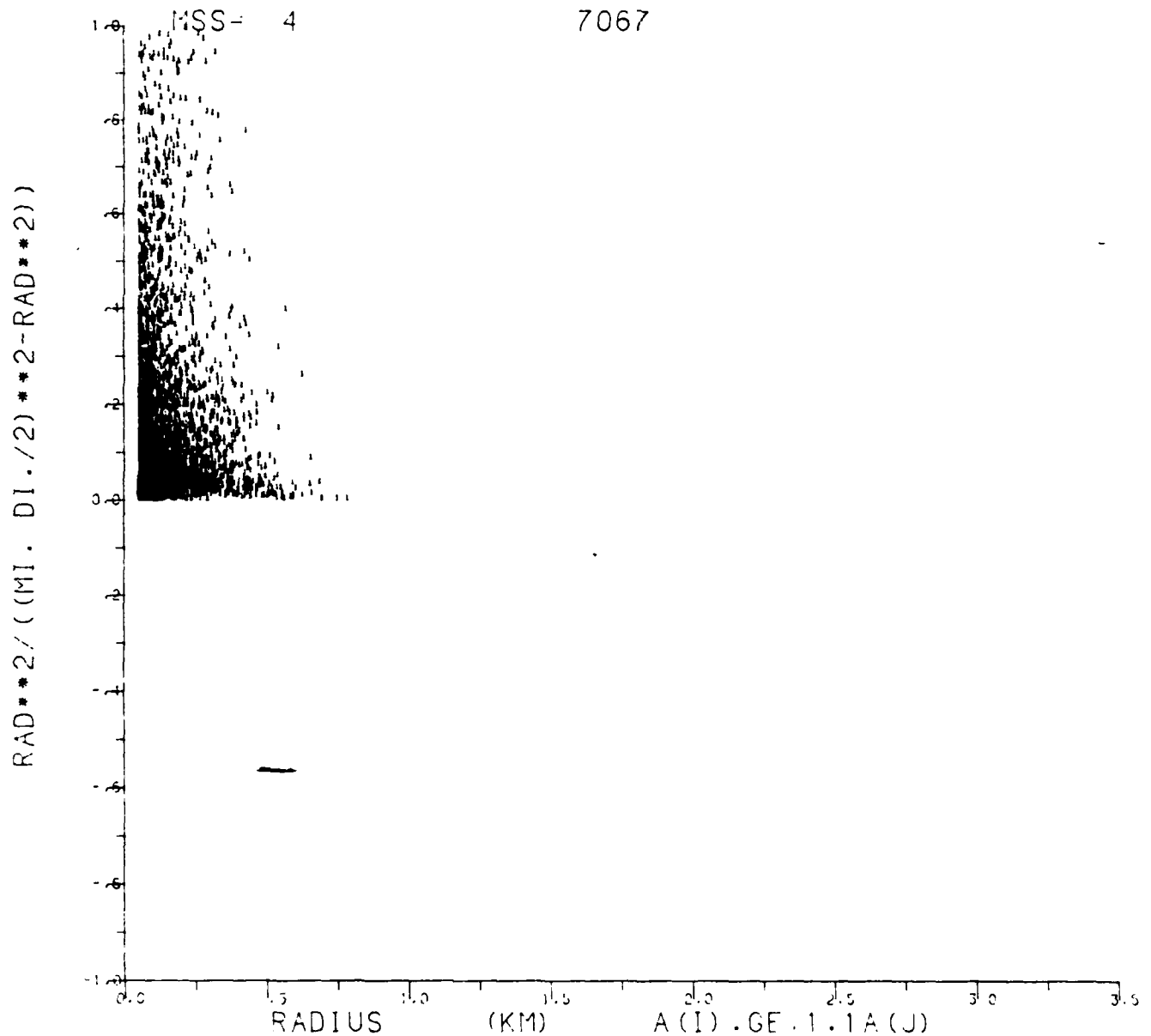
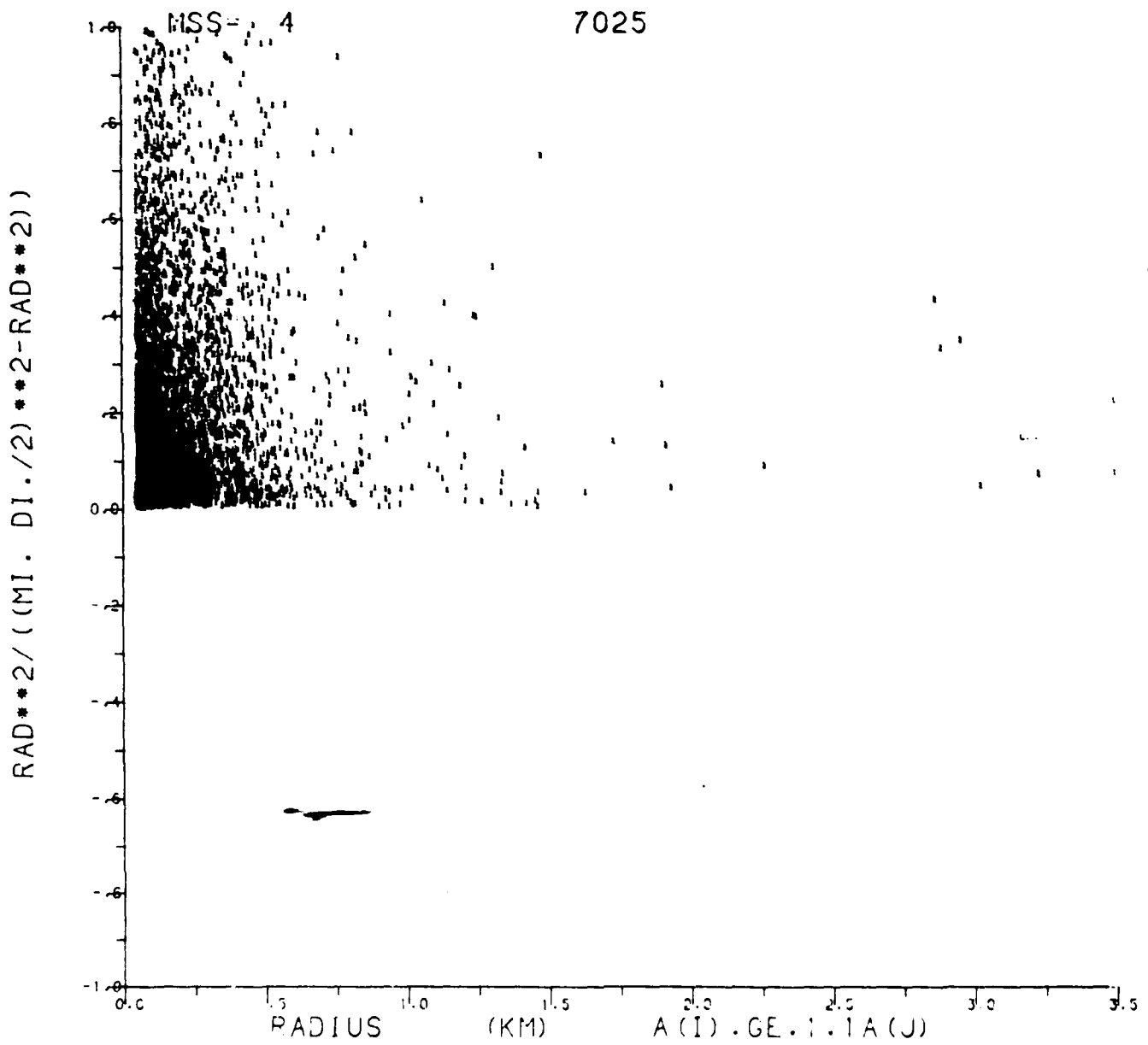


Figure 5.2: The parameter γ as a function of r for three cases:
 (a) Case 7067, cloudiness 1.4%; (b) Case 7025, cloudiness 13.5 %; (c) Case 7024, cloudiness 33%. All cases in Band MSS4.
 Results for MSS7 are identical.



I 68

AVXL



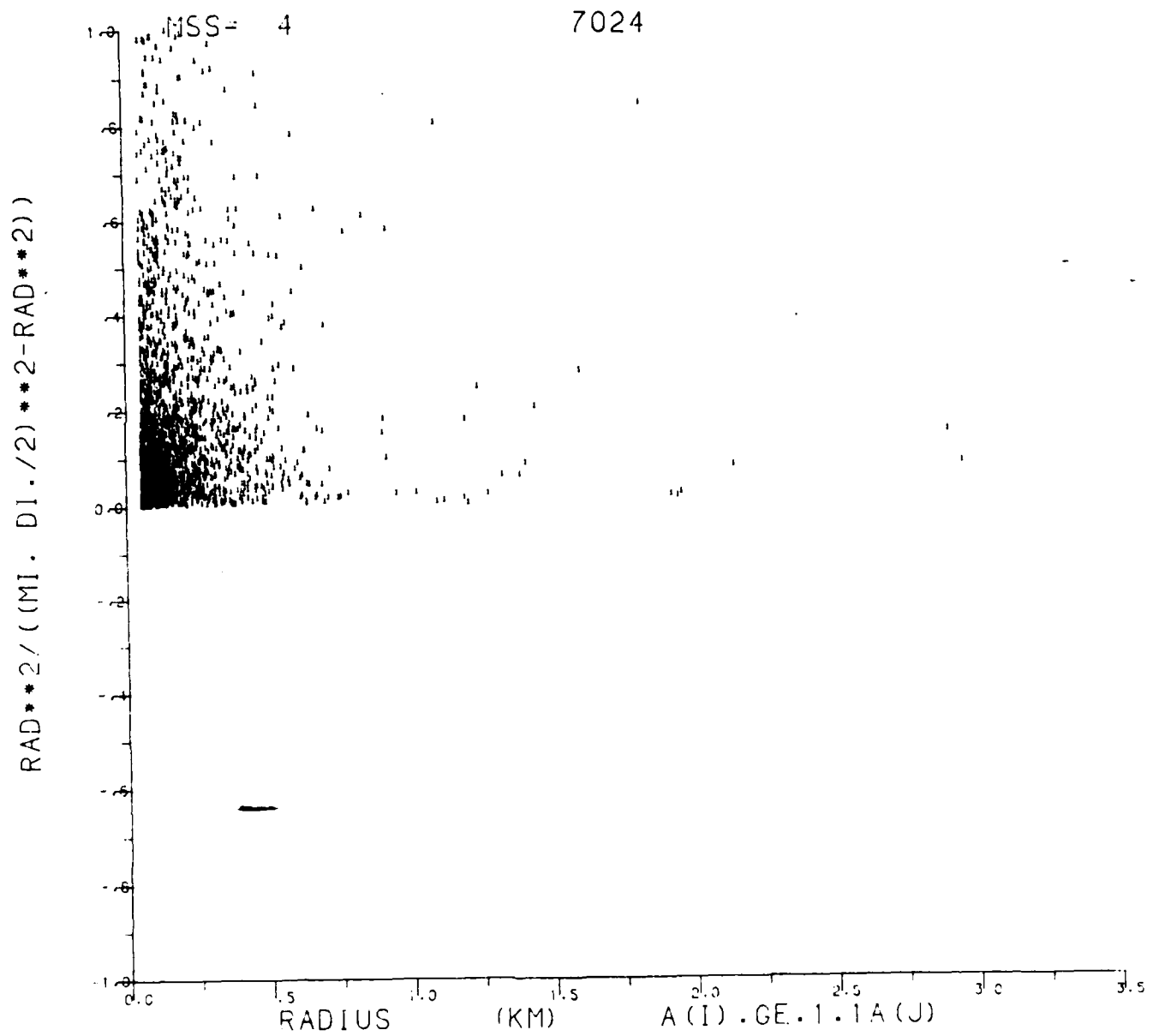


Table 5.1: Mean mass flux at cloud bottom altitude in $10^{-2} \text{ kgm}^{-2} \text{ s}^{-1}$

Image # *	Location	$M_o (10^{-2} \text{ kgm}^{-2} \text{ s}^{-1})$	Cloudiness %	$F_o \text{ km}^2$
7036	Ocean near Cape Verde Island	0.113	0.2	3.2 (4)
7034	Ocean near Cape Verde Islands	0.236	0.6	3.2 (4)
7072	Gulf of Mexico	0.130	0.8	1.8 (4)
7035	Ocean near Cape Verde Island	0.489	0.9	1.4 (4)
7067	Gulf of Mexico	0.656	1.5	3.2 (4)
7066	Gulf of Mexico	1.132	5.1	1.9 (4)
7032	Ocean near Marshall Island	1.362	6.7	3.1 (4)
7013	Med. W. of Israel	1.796	7.5	6.2 (3)
7029	Ocean E. of Florida	1.329	8.7	1.6 (4)
7064	Ocean E. of Florida	0.522	12.1	2.0 (4)
7025	Ocean E. of Florida	1.933	13.2	1.7 (4)
7033	Pacific Ocean in Tuamotu Archipelago	0.812	14.3	3.2 (4)
7028	Ocean E. of Florida	1.344	17.4	1.7 (4)
7026	Ocean E. of Florida	1.884	18.8	1.5 (4)
7030/31	Okinawa	2.181	27.0	2.2 (4)
7024	Ocean E. of Florida	2.083	33.1	8.0 (3)
7060	Bahamas	1.967	37.4	1.9 (4)
	Cheng (1980)	1.670	10.0	
	GATE A/B average	2.000	15.0	
	Houze and Betts (1981)			
	Ocean E. of Florida (Fraedrich 1977)	3.000	50.0	

*For exact coordinates, path and row - see Appendix I

TABLE 5.2a: 2-D Histogram of the ratio of cloud area to cloud area r_e^2
 - of influence as a function of cloud effective radius $\gamma = \frac{r_e^2}{(D/2)^2 - r_e^2}$
 Location: Gulf of Mexico, ID #7072, MSS4

γ \ r_e	0.00- 0.10	0.10- 0.20	0.20- 0.30	0.30- 0.40	0.40- 0.50	0.50- 0.60	0.60- 0.70	0.70- 0.80	0.80- 0.90	0.90 1.00
0.575-0.600	2	2	1	0	0	0	0	0	0	0
0.550-0.575	1	1	0	1	0	0	0	0	0	0
0.525-0.550	1	1	0	1	0	1	0	0	0	0
0.500-0.525	0	2	0	1	0	0	0	0	0	0
0.475-0.500	3	3	0	0	0	0	0	0	0	0
0.450-0.475	1	1	0	0	0	0	0	0	0	0
0.425-0.450	1	0	3	1	0	0	0	0	0	0
0.400-0.425	1	2	3	1	0	0	0	0	0	0
0.375-0.400	1	0	1	0	1	0	0	0	0	0
0.350-0.375	2	1	0	0	1	0	0	0	0	0
0.325-0.350	2	4	1	1	0	0	0	0	0	0
0.300-0.325	2	1	0	0	0	0	0	0	0	0
0.275-0.300	3	1	0	0	1	1	0	0	0	0
0.250-0.275	3	5	1	1	0	0	0	0	0	1
0.225-0.250	4	6	1	2	1	0	0	0	0	0
0.200-0.225	7	8	3	0	1	0	0	0	0	0
0.175-0.200	7	3	2	0	1	0	0	0	0	0
0.150-0.175	10	7	4	0	0	1	0	0	0	0
0.125-0.150	7	16	5	0	2	1	0	0	0	0
0.100-0.125	7	12	3	5	0	2	0	0	1	0
0.075-0.100	14	17	3	1	1	0	0	0	0	0
0.050-0.075	24	25	7	1	2	1	0	0	0	0
0.025-0.050	51	21	8	0	0	1	1	0	0	0
0.000-0.025	54	37	10	3	0	0	1	0	0	0

b) Same for MSS7 -

$\gamma \backslash r_e$	0.00- 0.10	0.10- 0.20	0.20- 0.30	0.30- 0.40	0.40- 0.50	0.50- 0.60	0.60- 0.70	0.70- 0.80	0.80- 0.90	0.90- 1.00
0.525 - 0.550	1	1	1	0	0	0	0	0	0	0
0.500 - 0.525	0	2	1	1	1	0	0	0	0	0
0.475 - 0.500	0	3	1	1	0	0	0	0	0	0
0.450 - 0.475	1	3	2	0	1	1	0	0	0	0
0.425 - 0.450	0	2	0	0	1	0	1	0	0	0
0.400 - 0.425	0	3	3	1	0	1	0	0	0	0
0.375 - 0.400	4	0	0	0	0	1	0	0	0	0
0.350 - 0.375	2	3	2	0	0	1	0	0	0	0
0.325 - 0.350	2	2	0	1	0	0	0	0	0	0
0.300 - 0.325	1	3	3	1	0	0	0	0	0	0
0.275 - 0.300	4	3	1	1	0	0	0	0	1	0
0.250 - 0.275	6	8	1	0	1	0	0	0	0	0
0.225 - 0.250	3	6	3	0	1	1	0	0	0	0
0.200 - 0.225	4	6	3	1	1	0	0	0	1	0
0.175 - 0.200	3	10	1	2	2	1	0	0	0	0
0.150 - 0.175	3	8	4	2	2	1	0	0	0	0
0.125 - 0.150	3	9	3	0	1	0	0	0	0	0
0.100 - 0.125	10	14	11	3	0	0	0	0	1	0
0.075 - 0.100	22	18	5	1	2	0	0	0	0	0
0.050 - 0.075	22	14	8	0	2	0	0	1	0	0
0.025 - 0.050	31	31	10	3	0	0	1	0	0	0
0.000 - 0.25	122	38	7	3	2	1	1	0	0	0

Introduction to the Appendices I - IV

Appendices I, II, III and IV summarize in concise form a great part of the basic information acquired during the course of this study.

Appendix I identifies the analysed images in several ways. In addition, information is provided on the parts of each image that were not analysed and the reasons for this, which are of interest in themselves. There are mainly three .

The first, A, is the presence in the image of land surfaces or shallow ocean. It is impossible to distinguish reliably between clouds and such variable backgrounds even with intensive man-computer interaction. Consequently, we have not analysed those parts of the images mentioned in the appendix. In addition, we will refrain from analysing any images over land, until appropriate techniques can be developed, which will probably have to include utilisation of information on the surface reflectivity and its spatial distribution.

The second reason, B, is the presence of fog or haze over the image with an intensity close to that of the smaller clouds. This makes it wellnigh impossible ~~to~~ discriminate a great number of the smaller clouds, part of the studied population, against the background.

The last reason, C, is the partial absence of an image or errors in the grey levels in the data base. It may also happen that there are over-estimates of cloudiness, especially in cases of reported cloudiness of ten percent or more in the acquired satellite data.

The second Appendix, II, summarises for the two bands analysed, 4 and 7, the area analysed in pixels, the criterion used for the grey levels, in each case, to distinguish between cloud and background, the exact percentage of cloudiness of the area analysed. Moreover, we specify the fractional area of clouds with areas of less than 4 pixels as "noise", as well as the number of such small clouds versus the number of clouds of larger size.

Appendix III summarises all available empirical fits to cloud size distributions in the form of power laws. Both the fit up to a maximal effective radius as well as that using all clouds, are given, showing the probable need for bi-modal distributions.

Secondly, all ($\log P$, $\log A$) fits given again for each histogram up to a maximal size as well as using all clouds. The radius of the break is identified in each case.

In the last column, the two average fractal dimensions of the perimeters in each case are given.

Appendix IV summarises fits to the distribution functions of the minimal distance between cloud pairs. Both log-normal and Weibull distributions are used. All distributions are normalised to 100 km^2 , to make comparisons possible between the various cases.

Some additional general information is required for using the appendices. The area of one pixel is 0.003249 km^2 . "Large clouds" are those clouds that have an area of more than three pixels. Only these are considered clouds. "Small clouds" are those of less than 4 pixels in area. This is the limit of our resolution and consequently the "small clouds" are considered to be noise:

There are 2983 lines and 3548 columns in a full image.

APPENDIX 1

Image No.	Image ID	Place	Path Row	Date YY DDD	Areas of Image Not Processed					
					R = Reason for Not Processing: A = Land or Shallow Ocean B = Fog Over Ocean C = Data Absent or in Error					
					Lines	Columns	R	Lines	Columns	R
7013	2555-07291	Israel	188-038	76-212						
7024	22072-15003	Bahamas	014-044	80-268	1- 700 1201-1500 2101-2983	900-3548 1600-3548 1-3548	A A A	701-1200 1501-2100	1200-3548 1900-3548	A A
7025	22073-15055	Straits Florida	015-043	80-269	1-1200 2100-2983	1-950 750-2200	A A	1-2983	2650-3548	A
7026	22056-15113	Straits Florida	016-043	80-252	1-1800	1-1200		1-1400	1201-3548	
7028	22109-15054	Straits Florida	015-043	80-305	1-1200 2100-2983	1- 950 750-2200	A A	1-2983	2650-3548	A
7029	22127-15052	Straits Florida	015-043	80-323	1-1200 1501-2983	1- 700 2600-3548	A A	1-1500 2100-2983	2400-3548 500-2100	A A
7030 7031	30277-01144	Okinawa		78-341	1- 219 1075-1277	1245-1700 544- 950	A A	407- 749 1970-2340	934-1330 1- 650	A A
7032	30346-21395	Pacific Ocean near Marshall Islands	083-049	79-045	No holes					
7033	30369-18510	Pacific Ocean Toamotu Islands	052-071	79-068	1100-2250 880- 930	1520-2200 1-3548	A C	2400-2679 2680-2800	200- 700 1-3548	A C
7034	30364-11203	Cape Verde W.Africa	226-050	79-063	450- 700	1500-1900	A	100- 700	1900-2500	A
7035	30364-11201	Cape Verde W.Africa	226-049	79-063	1-1299	1-3548	B	1300-2983	2601-3548	B
7036	30364-11194	Cape Verde W.Africa	226-048	79-063	2200-2983 1980-2200	1-1320 1- 200	A A	2640-2983	1320-2200	A
7060	22036-14590	Bahamas	014-041	80-232	1900-2983	1-2200	A	2420-2983	2201-3548	A
7064	22038-15094	Ocean E of Florida	016-039	80-234	660-1500	2200-3548	B	1760-2983	1400-3548	B
7066	22312-15310	Gulf Mexico	020-040	81-142	1-1800	1-3548	B			
7067	30661-15303	Gulf Mexico	020-040	79-360	No holes					
7072	31565-15595	Gulf Mexico	024-040	80-168	1-2983 1- 880	1-1030 1686-3548	C A	1- 220	1320-1685	B

- 132 -
APPENDIX 2

Image No.	MSS	Area Analysed in Pixels	Grey Level Threshold for Clouds	Percentage of Cloudiness	Percentage of Noise	No. of Large Clouds	No. of Small Clouds
7013	4 7	1909440 1909440	20 3	8.5922 7.3577	0.4038 0.3482	1269 1242	-
7024	4 7	2473345 2473345	21 3	32.9202 33.1866	0.1037 0.1156	2521 2420	2566 1728
7025	4 7	5285332 5285332	69 2	13.4944 12.8875	0.1039 0.1315	7329 7436	3173 4538
7026	4 7	4678420 4678420	21 3	18.9997 18.4689	0.0826 0.0793	4738 4671	2235 2152
7028	4 7	5304581 5304581	69 2	17.4672 17.3171	0.0647 0.0742	3349 3458	2017 2345
7029	4 7	4999329 4999329	65 2	8.7629 8.5214	0.0759 0.0930	4235 4241	2176 2836
7030 7031	4 7	6909474 6909474	43 3	27.5781 26.4643	0.1431 0.2021	6836 7013	-
7032	4 7	9650303 9650303	82 7	6.6937 6.7086	0.0540 0.0952	7327 7548	2976 6255
7033	4 7	8276192 8276192	77 6	14.5296 13.9987	0.0320 0.0742	3616 3562	1794 4750
7034	4 7	9716240 9716240	77 6	0.5882 0.6015	0.0147 0.0282	1477 1380	809 1634
7035	4 7	4210868 4210868	81 7	0.9156 0.9053	0.0311 0.0403	1274 1203	728 1104
7036	4 7	9714234 9714234	77 6	0.1843 0.1981	0.0086 0.0749	678 709	447 5019
7060	4 7	6685609 6685609	22 3	37.6347 37.1414	0.1082 0.1402	6676 6631	4146 5827
7064	4 7	6216943 6216943	27 5	12.0736 12.1883	0.0493 0.0485	2440 2252	1829 1849
7066	4 7	5789598 5789598	24 5	5.2203 4.8984	0.3688 0.4109	5172 5355	13842 15711
7067	4 7	9692370 9692370	17 4	1.3787 1.5027	0.0873 0.0496	4450 3932	5452 2645
7072	4 7	5428235 5428235	43 10	0.7906 0.7676	0.0183 0.0113	513 602	707 350

- 133 -
APPENDIX 3

Image No.	MSS	Fit to Cloud Radius Distribution $N(r_e) = ar_e^b$			Fit to (logP, logA) Curve $\log_{10} P = a + b \log_{10} A$			$D = \frac{2b_4 + 2b_7}{2}$
		Radii Used	$\log_{10} a$	b	Areas Used	a	b	
7013	4	all	-0.44198	-1.98529	all	0.92055	0.64519	1.28080
	4	up to $r_e = 0.5$ km	-0.79495	-2.58287	-	-	-	
	7	all	-0.55024	-2.16589	all	0.90748	0.63561	
	7	up to $r_e = 0.5$ km	-0.86184	-2.67101	-	-	-	
7024	4	all	-0.06557	-1.31674	all	0.91017	0.64455	1.29350
	4	up to $r_e = 0.46$ km	-0.92221	-2.86250	from $A = 0.50$ km ²	0.93190	0.77170	
	7	all	-0.7304	-1.25780	all	0.91857	0.64895	
	7	up to $r_e = 0.46$ km	-0.94806	-2.86977	from $A = 0.50$ km ²	0.93643	0.77233	
7025	4	all	-0.01599	-1.80115	all	0.90190	0.64352	1.29755
	4	up to $r_e = 0.40$ km	-0.44520	-2.85626	from $A = 0.50$ km ²	0.92387	0.76133	
	7	all	-0.05133	-1.87171	all	0.92129	0.65403	
	7	up to $r_e = 0.40$ km	-0.40766	-2.82256	from $A = 0.50$ km ²	0.94649	0.76927	
7026	4	all	0.00582	-1.50017	all	0.89502	0.63742	1.27712
	4	up to $r_e = 0.53$ km	-0.75173	-3.02705	from $A = 0.50$ km ²	0.91603	0.73303	
	7	all	-0.01765	-1.50492	all	0.89756	0.63970	
	7	up to $r_e = 0.43$ km	-0.74855	-3.02206	from $A = 0.50$ km ²	0.91599	0.73351	
7028	4	all	0.02724	-1.14899	all	0.91051	0.64451	1.29673
	4	up to $r_e = 0.36$ km	-1.03915	-3.13759	from $A = 0.50$ km ²	0.90106	0.74978	
	7	all	0.04027	-1.17093	all	0.92515	0.65222	
	7	up to $r_e = 0.36$ km	-1.01134	-3.12829	from $A = 0.50$ km ²	0.91744	0.76207	
7029	4	all	-0.02673	-1.39878	all	0.92524	0.65614	1.32037
	4	up to $r_e = 0.28$ km	-0.80577	-3.01304	from $A = 0.50$ km ²	0.95467	0.80137	
	7	all	-0.04716	-1.44257	all	0.94330	0.66423	
	7	up to $r_e = 0.28$ km	-0.72510	-2.92320	from $A = 0.50$ km ²	0.97089	0.81907	
7030 and 7031	4	all	0.20452	-1.35001	all	0.91718	0.65297	1.31010
	4	up to $r_e = 1.20$ km	-0.08146	-2.32960	-	-	-	
	7	all	0.20716	-1.36263	all	0.92806	0.65713	
	7	up to $r_e = 1.20$ km	-0.08812	-2.37884	-	-	-	
7032	4	all	-0.01273	-1.85315	all	0.87562	0.62467	1.25436
	4	up to $r_e = 1.00$ km	-0.34390	-2.63715	-	-	-	
	7	all	-0.02089	-1.88638	all	0.88939	0.62969	
	7	up to $r_e = 1.00$ km	-0.35931	-2.68639	-	-	-	
7033	4	all	-0.65950	-1.14230	all	0.88669	0.63058	1.26830
	4	up to $r_e = 0.56$ km	-0.77968	-2.85170	from $A = 0.50$ km ²	0.89297	0.69764	
	7	all	-0.55310	-1.15870	all	0.90364	0.63772	
	7	up to $r_e = 0.56$ km	-0.76617	-2.82177	from $A = 0.50$ km ²	0.90917	0.70766	
7034	4	all	-0.56379	-1.98367	all	0.89844	0.63293	1.27281
	4	up to $r_e = 0.37$ km	-1.03314	-2.69731	from $A = 0.50$ km ²	0.95080	0.78624	
	7	all	-0.54762	-1.94276	all	0.91381	0.63988	
	7	up to $r_e = 0.36$ km	-1.08271	-2.75142	from $A = 0.50$ km ²	0.95920	0.77243	
7035	4	all	-0.65404	-2.02471	all	0.88445	0.62389	1.25362
	4	up to $r_e = 0.35$ km	-1.40224	-3.07728	from $A = 0.50$ km ²	0.94747	0.73822	
	7	all	-0.63874	-1.99064	all	0.89696	0.62973	
	7	up to $r_e = 0.35$ km	-1.34412	-2.98635	from $A = 0.50$ km ²	0.94904	0.67445	
7036	4	all	-0.76595	-1.96454	all	0.87441	0.61800	1.23910
	4	up to $r_e = 0.333$ km	-1.26233	-2.61392	from $A = 0.50$ km ²	0.91386	0.86660	
	7	all	-0.79351	-2.00409	all	0.88145	0.62110	
	7	up to $r_e = 0.333$ km	-1.30742	-2.67713	from $A = 0.50$ km ²	0.92113	0.84160	

APPENDIX 3

7060	4	all	0.06275	-1.39980	all	0.91190	0.64525	1.29246
	4	up to $r_e=0.35$ km	-0.77280	-3.18511	from $A=0.50$ km ²	0.93380	0.74929	1.50674
	7	all	0.06596	-1.39957	all	0.92098	0.64721	
	7	up to $r_e=0.34$ km	-0.64386	-3.04911	from $A=0.50$ km ²	0.94605	0.75745	
7064	4	all	-0.13472	-1.33572	all	0.95273	0.66050	1.32496
	4	up to $r_e=0.27$ km	-1.35905	-3.30411	from $A=0.50$ km ²	0.98586	0.79068	1.59143
	7	all	-0.13547	-1.36278	all	0.95553	0.66446	
	7	up to $r_e=0.27$ km	-1.12321	-3.02937	from $A=0.50$ km ²	0.99001	0.80075	
7066	4	all	-0.22053	-1.70314	all	1.06074	0.70332	1.38849
	4	up to $r_e=0.30$ km	-1.25336	-3.47954	from $A=0.50$ km ²	1.00909	0.98368	1.94642
	7	all	-0.26772	-1.79310	all	1.03707	0.68517	
	7	up to $r_e=0.30$ km	-1.27233	-3.50998	from $A=0.50$ km ²	1.00447	0.96274	
7067	4	all	-0.79319	-2.93864	all	0.89578	0.62070	1.25666
	4	up to $r_e=0.3$ km	-0.75674	-2.95584	from $A=0.50$ km ²	0.98009	0.97102	1.71874
	7	all	-0.70365	-2.82239	all	0.90620	0.63596	
	7	up to $r_e=0.3$ km	-0.62811	-2.76809	from $A=0.50$ km ²	0.94905	0.74772	
7072	4	all	-0.27861	-1.06982	all	0.91369	0.63568	1.28183
	4	up to $r_e=0.25$ km	-1.68625	-2.91277	from $A=0.50$ km ²	0.92356	0.87856	1.68530
	7	all	-0.31335	-1.15139	all	0.91045	0.64615	
	7	up to $r_e=0.25$ km	-1.65080	-2.91708	from $A=0.50$ km ²	0.93795	0.80674	

APPENDIX 4

FIT TO MINIMAL DISTANCE BETWEEN CLOUD PAIRS, D

Image No.	MSS	$N(D) = P3 * \exp -((\ln D - P1)^2 / (2P2)^2)$ $+ = P3 \text{ Computed for Normalized Areas}$			$N(D) = P3 * D^{P1} * \exp(-P2 * D^{(P1+1)})$ $+ = P3 \text{ Computed for Normalized Areas}$		
		P1	P2	P3	P1	P2	P3
7013	4	-0.55994	0.49111	64.7705	1.52873	1.79018	221.49639
	7	-0.55922	0.51032	61.1564	1.40091	1.60098	187.68728
7024	4	-0.74456	0.52621	138.7939	1.28525	2.24294	489.87466
	7	-0.76980	0.54838	129.4032	1.23844	2.23453	453.06119
7025	4	-0.80450	0.54548	409.4483	1.23796	2.36535	1458.41991
	7	-0.83677	0.56044	415.9373	1.18027	2.36847	1448.37904
7026	4	-0.73929	0.59695	227.5773	1.05220	1.66901	635.62997
	7	-0.74346	0.60588	163.8646	1.03172	1.64914	455.15136
7028	4	-0.73055	0.57695	160.9150	1.16185	1.82621	491.20837
	7	-0.74694	0.58009	168.3463	1.09676	1.84269	503.37175
7029	4	-0.80760	0.53882	242.7626 ⁺	1.25644	2.48817	906.76298 ⁺
	7	-0.76815	0.52067	245.2799 ⁺	1.39112	2.54228	975.95436 ⁺
7030	4	-0.47792	0.56580	272.7483	1.19935	1.07889	631.35858
	7	-0.45241	0.55616	280.8868	1.21929	1.06552	652.89730
7032	4	-0.63542	0.52871	353.1548	-	-	-
	7	-0.63854	0.52226	370.6761	-	-	-
7033	4	-0.73724	0.65187	149.7132	0.87340	1.38239	355.6843
	7	-0.73916	0.64319	148.8162	0.86456	1.39155	349.29688
7034	4	-0.82847	0.59149	74.5011	1.00986	1.94548	217.38228
	7	-0.75763	0.53689	71.7074	1.21063	2.19246	242.17473
7035	4	-0.82990	0.60341	57.4976	0.82554	1.72054	142.11590
	7	-0.84268	0.58965	54.7118	0.85806	1.90916	144.54251
7036	4	-0.81506	0.66436	25.6057	0.95432	1.74619	72.32391
	7	-0.97421	0.73145	26.7265	0.77940	1.96263	74.56375
7060	4	-0.72741	0.54371	336.6152 ⁺	1.30295	2.08892	1231.31990 ⁺
	7	-0.77908	0.55998	355.6379 ⁺	1.20922	2.18450	1323.11584 ⁺
7064	4	-0.89713	0.57941	138.6066 ⁺	1.01659	2.28049	463.04405
	7	-0.91769	0.55387	140.3201 ⁺	1.14643	2.84010	574.79191
7066	4	-1.22084	0.50574	452.5571	1.50547	9.10124	4021.24733
	7	-1.27320	0.50134	501.4725	1.48414	9.89945	4581.70214
7067	4	-0.94194	0.61714	239.0711 ⁺	0.96318	4.36410	774.09093 ⁺
	7	-0.81692	0.58321	202.6496 ⁺	1.05446	4.14845	663.90040 ⁺
7072	4	-0.79638	0.60631	25.4142 ⁺	1.05881	1.90624	84.51854 ⁺
	7	-0.69105	0.59546	27.7992 ⁺	1.18349	1.72497	95.48503 ⁺

DESCRIPTION OF COOPERATION AND ASSESSMENT OF THE CONTRIBUTION OF BOTH PARTNERS

1. Introduction

The work of the two partners is very tightly interconnected and complementary. In addition, however, each of the two partners also has separate aims and plans w.r.t. the results.

2. Contribution of U.S. partner

The U.S. partner has provided

- . catalogues of LANDSAT MSS data at EROS Data Center and at NASA-GSFC
- . 60° swath of LANDSAT 4 data in the Pacific Ocean is being analysed by him
- . two 7-band scenes of LANDSAT 4 TM data including tape dump in the Carolinas area
- . software for reading LANDSAT 4 TM tapes
- . documentation on facilities and software available at the Goddard Space Flight Center
- . advice on Weibull functions and their use in statistics
- . comparison of different techniques for calculating the length of perimeters for small clouds

3. Contribution of Israeli partner

The Israeli partner has provided

- . size, nearest neighbour spacing and other distribution functions and other data
- . non-linear fits of the above to various probability distribution functions indicated by physical intuition
- . application to problems of convection in the atmosphere
- . development of radiative transfer technique for cloud top height determination
- . software for the analysis, identification and labelling of clouds and cloud fields
- . choice of LANDSAT 3, 4 and 5 imagery for analysis and their organization into catalogues
- . computer memory disk rental and data purchase through independent funding

In addition to the above contributions, each partner has pursued his own specific plans with the results.

The US partner emphasizes analysis of the relationship of sub-grid scale convective processes on horizontally averaged quantities in the atmosphere and the large-scale conditions in which cumulus convection occurs.

The Israeli partner's aims are to use the data in the parameterisation of vertical radiative transfer of energy in fields of broken cloudiness and diagnosis of conditions of atmospheric convection dynamics from the cloud field structure, cloud height, etc.

APPENDIX 6

Inventory and Status of Data - May 1986

PRODUCTION STAGE OF MAGNETIC TAPES

- * - TAPE ON ORDER, NOT YET RECEIVED
- * - TAPE RECEIVED, NO WORK DONE YET
- * - TAPE COPIED ONTO OUR BACK-UP TAPE
- * - READ AND COPIED DATA FROM ONE OR MORE BANDS
- * - PARTIAL ANALYSIS OF DATA
- * - ANALYSIS COMPLETED

FILM POSITIVES

- * - ON ORDER
- * - RECEIVED
- X - FILM RETURNED FOR EXCHANGE

OPEN ANALYSIS NOT COMPLETED

- A - PAGELEMS
- B - NO CONTINUATION, NO OCEAN BACKGROUND
- C - NO CONTINUATION, INSUFFICIENT CLOUDS
- D - NO CONTINUATION, TAPE PROBLEMS
- E - OLD TAPES, NEED SPECIAL TREATMENT, MAY BE ANALYSED LATER
- F - NO CONTINUATION, TOO MANY SMALL ISLANDS
- G - NO CONTINUATION, INSUFFICIENT CORRELATION BETWEEN PSS-4 AND MSS-7
- X - TAPE ON ORDER RETURNED TO EOS OR EUSAT FOR EXCHANGE

PATH NO	SCENE ID	PLACE	PART OF IMAGE	YY RDD	FILM POSITIVES	PRODUCTION STAGE OF TAPES	IMAGE NO
	2055-05214	PAKISTAN	1,2/4		+	30	7010
	2055-05214	PAKISTAN	3,4/4		+	30	7011
18E 39	2555-07291	ISRAEL	4/4		+	18	7012
18E 39	2555-07291	ISRAEL	3/4		+	4	7013
19 40	30930-15143	GULF MEXICO	1/1		+	*	7014
16 41	31555-15255	GULF MEXICO	1/1		+	*	7015
16 41	22058-15221	GULF MEXICO	1/1		+	*	7016
	32735-23314	AUSTRALIA	1/2		+	OF	
	32735-23314	AUSTRALIA	2/2		+	OF	
	30335-10401	SENEGAL	1/1		+	OF	
45 43	22145-15051	STRAITS FLORIDA	1/1		+	10	7021
	22145-15051	STRAITS FLORIDA	1/1		+	10	7022
14 43	22072-15000	BAHAMAS	1/1	RD 268	+	20	7023
14 44	22072-15003	BAHAMAS	1/1	RD 268	+	4	7024
15 43	22072-15055	STRAITS FLORIDA	1/1	RD 268	+	4	7025
16 43	22058-15113	STRAITS FLORIDA	1/1	RD 252	+	4	7026
	22147-15102	STRAITS FLORIDA	1/1		+	30	7027
15 43	22145-15054	STRAITS FLORIDA	1/1	RD 305	+	4	7028
15 43	22127-15052	STRAITS FLORIDA	1/1	RD 373	+	4	7029
	32777-01144	OKINAWA	1,2/4		+	4	7030
	32777-01144	OKINAWA	3,4/4		+	4	7031
83 49	30346-21350	PAC OCN MARSHALL IS	1/1	79 045	+	4	7032
15 51	30346-21350	PAC OCN MARSHALL IS	1/1	79 069	+	4	7033
220 46	30346-11203	CAPE VERDE W AFRICA	1/1	79 063	+	4	7034
220 46	30346-11201	CAPE VERDE W AFRICA	1/1	79 063	+	4	7035
220 46	30346-11154	CAPE VERDE W AFRICA	1/1	79 063	+	4	7036
	40045-15151	S CAROLINA	1/2		+	2A	7037
	40045-15151	S CAROLINA	2/3		+	2A	7038
	40045-15151	S CAROLINA	3/3		+	2A	7039
	40045-15171	FLORIDA KEYS	3/3		+	1	7042
	40045-15171	FLORIDA KEYS	2/3		+	1	7043
	40045-15171	FLORIDA KEYS	1/3		+	1	7044
	2055-05212	PAKISTAN	1,2/4		+	2A	7045
	10545-14453	MAINE	1,2/4		+	OF	7048
	10545-14453	MAINE	3,4/4		+	OF	7049
	10545-14453	FLORIDA	1,2/4		+	1A	7050
	10545-14453	E OF MAINE	1,2/4		+	1A	7051
	20704-15105	FLORIDA	1/2		+	1C	7053
300 42	30100-17302	UTAH	1/4			1A	7054
300 42	30100-17302	UTAH	2/4			1A	7055
300 42	30100-17302	UTAH	3/4			1A	7056
300 42	30100-17302	UTAH	4/4			1A	7057
	30605-17413	UTAH	2/4			1	7058
	30140-17370	UTAH	3/4			10	7059
14 41	30605-14500	BAHAMAS	1/1	RD 237	+	4	7060
14 41	30605-14500	BAHAMAS	1/1	RD 242	+	2E	7061
14 42	30605-14500	BAHAMAS	1/1	RD 242	+	2E	7062
14 42	30605-14500	BAHAMAS	1/1	RD 206	+	2E	7063
14 43	30605-14500	UCN E OF FLORIDA	1/1	RD 214	+	4	7064
14 43	30605-14500	UCN E OF FLORIDA	1/1	79 221	+	3	7065

20	21	22	23	24	25	26	27	28	29	30	31	32	33	34	35	36	37	38	39	40	41	42	43	44	45	46	47	48	49	50	51	52	53	54	55	56	57	58	59	60	61	62	63	64	65	66	67	68	69	70	71	72	73	74	75	76	77	78	79	80	81	82	83	84	85	86	87	88	89	90	91	92	93	94	95	96	97	98	99	00	01	02	03	04	05	06	07	08	09	10	11	12	13	14	15	16	17	18	19	20	21	22	23	24	25	26	27	28	29	30	31	32	33	34	35	36	37	38	39	40	41	42	43	44	45	46	47	48	49	50	51	52	53	54	55	56	57	58	59	60	61	62	63	64	65	66	67	68	69	70	71	72	73	74	75	76	77	78	79	80	81	82	83	84	85	86	87	88	89	90	91	92	93	94	95	96	97	98	99	00	01	02	03	04	05	06	07	08	09	10	11	12	13	14	15	16	17	18	19	20	21	22	23	24	25	26	27	28	29	30	31	32	33	34	35	36	37	38	39	40	41	42	43	44	45	46	47	48	49	50	51	52	53	54	55	56	57	58	59	60	61	62	63	64	65	66	67	68	69	70	71	72	73	74	75	76	77	78	79	80	81	82	83	84	85	86	87	88	89	90	91	92	93	94	95	96	97	98	99	00	01	02	03	04	05	06	07	08	09	10	11	12	13	14	15	16	17	18	19	20	21	22	23	24	25	26	27	28	29	30	31	32	33	34	35	36	37	38	39	40	41	42	43	44	45	46	47	48	49	50	51	52	53	54	55	56	57	58	59	60	61	62	63	64	65	66	67	68	69	70	71	72	73	74	75	76	77	78	79	80	81	82	83	84	85	86	87	88	89	90	91	92	93	94	95	96	97	98	99	00	01	02	03	04	05	06	07	08	09	10	11	12	13	14	15	16	17	18	19	20	21	22	23	24	25	26	27	28	29	30	31	32	33	34	35	36	37	38	39	40	41	42	43	44	45	46	47	48	49	50	51	52	53	54	55	56	57	58	59	60	61	62	63	64	65	66	67	68	69	70	71	72	73	74	75	76	77	78	79	80	81	82	83	84	85	86	87	88	89	90	91	92	93	94	95	96	97	98	99	00	01	02	03	04	05	06	07	08	09	10	11	12	13	14	15	16	17	18	19	20	21	22	23	24	25	26	27	28	29	30	31	32	33	34	35	36	37	38	39	40	41	42	43	44	45	46	47	48	49	50	51	52	53	54	55	56	57	58	59	60	61	62	63	64	65	66	67	68	69	70	71	72	73	74	75	76	77	78	79	80	81	82	83	84	85	86	87	88	89	90	91	92	93	94	95	96	97	98	99	00	01	02	0
----	----	----	----	----	----	----	----	----	----	----	----	----	----	----	----	----	----	----	----	----	----	----	----	----	----	----	----	----	----	----	----	----	----	----	----	----	----	----	----	----	----	----	----	----	----	----	----	----	----	----	----	----	----	----	----	----	----	----	----	----	----	----	----	----	----	----	----	----	----	----	----	----	----	----	----	----	----	----	----	----	----	----	----	----	----	----	----	----	----	----	----	----	----	----	----	----	----	----	----	----	----	----	----	----	----	----	----	----	----	----	----	----	----	----	----	----	----	----	----	----	----	----	----	----	----	----	----	----	----	----	----	----	----	----	----	----	----	----	----	----	----	----	----	----	----	----	----	----	----	----	----	----	----	----	----	----	----	----	----	----	----	----	----	----	----	----	----	----	----	----	----	----	----	----	----	----	----	----	----	----	----	----	----	----	----	----	----	----	----	----	----	----	----	----	----	----	----	----	----	----	----	----	----	----	----	----	----	----	----	----	----	----	----	----	----	----	----	----	----	----	----	----	----	----	----	----	----	----	----	----	----	----	----	----	----	----	----	----	----	----	----	----	----	----	----	----	----	----	----	----	----	----	----	----	----	----	----	----	----	----	----	----	----	----	----	----	----	----	----	----	----	----	----	----	----	----	----	----	----	----	----	----	----	----	----	----	----	----	----	----	----	----	----	----	----	----	----	----	----	----	----	----	----	----	----	----	----	----	----	----	----	----	----	----	----	----	----	----	----	----	----	----	----	----	----	----	----	----	----	----	----	----	----	----	----	----	----	----	----	----	----	----	----	----	----	----	----	----	----	----	----	----	----	----	----	----	----	----	----	----	----	----	----	----	----	----	----	----	----	----	----	----	----	----	----	----	----	----	----	----	----	----	----	----	----	----	----	----	----	----	----	----	----	----	----	----	----	----	----	----	----	----	----	----	----	----	----	----	----	----	----	----	----	----	----	----	----	----	----	----	----	----	----	----	----	----	----	----	----	----	----	----	----	----	----	----	----	----	----	----	----	----	----	----	----	----	----	----	----	----	----	----	----	----	----	----	----	----	----	----	----	----	----	----	----	----	----	----	----	----	----	----	----	----	----	----	----	----	----	----	----	----	----	----	----	----	----	----	----	----	----	----	----	----	----	----	----	----	----	----	----	----	----	----	----	----	----	----	----	----	----	----	----	----	----	----	----	----	----	----	----	----	----	----	----	----	----	----	----	----	----	----	----	----	----	----	----	----	----	----	----	----	----	----	----	----	----	----	----	----	----	----	----	----	----	----	----	----	----	----	----	----	----	----	----	----	----	----	----	----	----	----	----	----	----	----	----	----	----	----	----	----	---

END

1-87

DTIC